Architecture and Dynamics of the Ventral Actin Stress Fiber Network

By

Shwetha Narasimhan

Dissertation
Submitted to the Faculty of the
Graduate School of Vanderbilt University
in partial fulfillment of the requirements
for the degree of

DOCTOR OF PHILOSOPHY
in

Cell and Developmental Biology

May 31, 2022
Nashville, Tennessee

Approved:
David Miller, Ph.D.
Katherine Friedman, Ph.D.
Matthew Tyska, Ph.D.
Dylan Burnette, Ph.D.
Irina Kaverina, Ph.D.

To my dear family, whose love, support, and steadfast faith

has nourished and inspired me every day

ACKNOWLEDGEMENTS

My graduate training at Vanderbilt has been a time of intense learning, discovery and personal growth. As the first in my family to attend graduate school, I'm so thankful for the opportunity to attend this amazing institution and study from learned scientists and peers to grow my research and analysis skills, scientific knowledge and choose my career path.

I'm deeply grateful to my advisor, Dr. Irina Kaverina for her long-standing support and guidance in my scientific training, experiments and analyses; as well as my professional development in growing as a researcher. Irina's dedication to enriching her trainees beyond the lab through memorable get-togethers; and her commitment to DEI in the lab and beyond is deeply commendable. My thanks to all my current and former lab-mates for their help and advice with my research, congeniality and support that inspired each other to excel in our work.

I am deeply thankful to my committee- Dr. David Miller, Dr. Katherine Friedman, Dr. Matthew Tyska and Dr. Dylan Burnette for their guidance and support in my research and progression of my graduate training. I am deeply grateful to Dr. Miller for his capable guidance and support in completing my research and training at Vanderbilt successfully. I am deeply grateful to Dr. Friedman for her long-standing support and advice in both my research and in navigating complex situations. I am deeply grateful to Dr. Tyska and Dr. Burnette for their brilliant advice and insight into my research and training. My heartfelt gratitude to the late Dr. Donna Webb for her cheerful support and mentorship. Though my time under her training was tragically short, her work ethos and advice have keenly guided my development as a scientist. I am deeply thankful to my funding sources, especially the National Institutes of Health and the American Heart Association for their support of my work and scholarship.

My special thanks to the professional growth programs by the staff of the BRET office, the CDB department and other Vanderbilt resources for honing my soft skills and enabling my well-rounded career development.

In addition to my scientific training, a key part of my PhD experience was the learning of resilience and developing grit. Through my years of experimentation and analysis, I am thankful to have strengthened my reasoning and quantitative skills to be robust even in the face of ambiguity and failure. Though my time at Vanderbilt has presented me with the lion's share of circumstantial challenges through my injuries and the arc of my training, I also gratefully acknowledge how this has led to the growth of my unbowed and adept spirit which I will cherish for all my life.

Coming to the US as a naïve international student seven years ago, I had no inkling of the challenging and instructive years that lay before me. However, even back then, as I do now, I knew I could move forward as I had the unwavering, cherished love, prayers and support of my dear family. Though we have been separated by two continents and an ocean, visa challenges, health challenges and a vicious pandemic, our abiding love and care for each other has sustained and guided us to surmount all our obstacles, be it in health, careers, relations and more, so that we may live and grow together through our lives. I can't wait to meet you in person soon and hug you, mom, dad and Shreyaa!

TABLE OF CONTENTS

LIST OF FIGURES

CHAPTER 1: INTRODUCTION

1.1 THE CYTOSKELETON

The cytoskeleton is a dynamic network of protein filaments that provides spatial organization in the cell, connects the cell to the microenvironment through physical and biochemical links; and generates forces that coordinate cell shape and movement (Fletcher & Mullins, 2010).

Eukaryotic cells possess three main types of cytoskeletal filaments: actin microfilaments, intermediate filaments and microtubules.

Actin microfilaments are the smallest in width, measuring 7 nm in diameter, comprised of polymers of G-actin monomer arranged in a double helical structure. Intermediate filaments are 10 nm in diameter, forming two anti-parallel helices from a variety of proteins such as keratins, vimentins, desmins, lamins and more. Microtubules are the largest in width at around 25 nm in diameter. They are hollow cylinders made from thirteen protofilaments of alpha and beta tubulin polymers.

The architecture and dynamics of the cytoskeleton are regulated by several kinds of proteins (Fletcher & Mullins, 2010) such as

1) nucleation promoting factors, which regulate initial filament formation

2) capping proteins, which regulate filament termination

3) polymerases, which promote the growth of the filament

4) depolymerases and severing factors, which promote filament disassembly and reduce filament length

5) crosslinking and stabilizing proteins, which organize higher-order filament networks

1.1.1 FUNCTIONS OF THE CYTOSKELETON IN CELLS

Cytoskeletal filaments are functionally significant based on the characteristics and interacting network of the component protein. The polarity of cytoskeletal polymers by the asymmetrical arrangement of monomers produces tracks for cytoskeletal motors to move directionally in the cell. The motors contribute to the organization and function of the cytoskeletal filaments and serve to transport cargo between intracellular compartments. The main cytoskeletal motor proteins are myosin in actin microfilaments and kinesin and dynein in microtubules.

Actin microfilaments form a variety of structural arrangements such as branched networks near the leading edge of the cell that promote cell protrusion and migration, small projections made from bundled actin that sense the environment and promote directionality of migration; and complex, long bundled fibers that produce contractile forces and allow for cell polarization.

Intermediate filaments provide structural support to the cell and promote maintenance of cell shape and rigidity. They anchor organelles such as the nucleus and desmosomes in place. As an example, Lamins are fibrous, type V intermediate filament proteins that interact with the inner nuclear membrane and form the dense fibrillar network called the nuclear lamina. The lamina provides mechanical support to the nucleus and performs a host of other functions such as chromatin organization, regulation of DNA transcription and regulation of the DNA damage response. Defects in the Lamin genes lead to laminopathies such as Hutchinson-Gilford Progeria syndrome, Emery–Dreyfuss muscular dystrophy and dermopathies (Gruenbaum et al, 2005; Burke & Stewart, 2013).

Microtubules perform a variety of cellular functions in interphase and during mitosis. Interphase microtubule arrays facilitate cell polarization, vesicular transport, regulation of structures like focal adhesions involved in mechano-transduction and cell movement. During mitosis, microtubules arrange into the mitotic spindle apparatus to find and position chromosomes using the characteristic dynamic instability of the tubulin

polymers. Microtubules also form structural core of cilia and flagella and have links to gene regulation (Nogales, 2000; Brouhard & Rice, 2018; Gudimchuk & McIntosh, 2021).

1.2 THE ACTIN CYTOSKELETON

Actin is a globular protein abundantly found in eukaryotic cells. Actin has a monomeric form called G-actin, which, when organized into filaments is known as F-actin. G-actin has 374 amino acid residues, and its crystal structure shows that the monomer has two main lobes with a deep cleft in the middle. This cleft has a fold which binds a Magnesium ion and Adenosine Tri-Phosphate (ATP) (Merino et al, 2020). Binding of the nucleotide is essential to the stability of G-actin, and without this binding the monomer unfolds (Asakura, 1961). The two lobes are further divided into four sub domains (SD1-4). Subdomains 1 and 3 comprise the barbed end (plus end) while Subdomains 2 and 4 comprise the pointed end (minus end). These two ends differ by the rate of actin monomer addition and dissociation, thus defining the polarity of the actin polymer.

There are six actin genes that give rise to the following isoforms in birds and mammals- the alpha (skeletal) actin, the alpha (cardiac) actin, the alpha (smooth) actin and gamma (smooth) actin that are expressed in skeletal, cardiac and smooth muscle; and the beta (cyto) actin and gamma (cyto) actin that are present ubiquitously (Perrin, 2010).

G actin monomers polymerize into filamentous F actin, forming a double stranded helix 7-9 nm wide (Holmes et al, 1990). The monomer to filament conformational transition involves rotation of the two major domains by 20 degrees, thus G-actin is flattened while being incorporated into F-actin (Oda et al, 2009). Actin does not effectively hydrolyze ATP in its monomeric form, but upon polymerization the ATPase activity increases 42,000 times (Merino et al, 2020; Blanchoin & Pollard, 2002), leading to ATP hydrolysis into ADP and release of the phosphate ion.

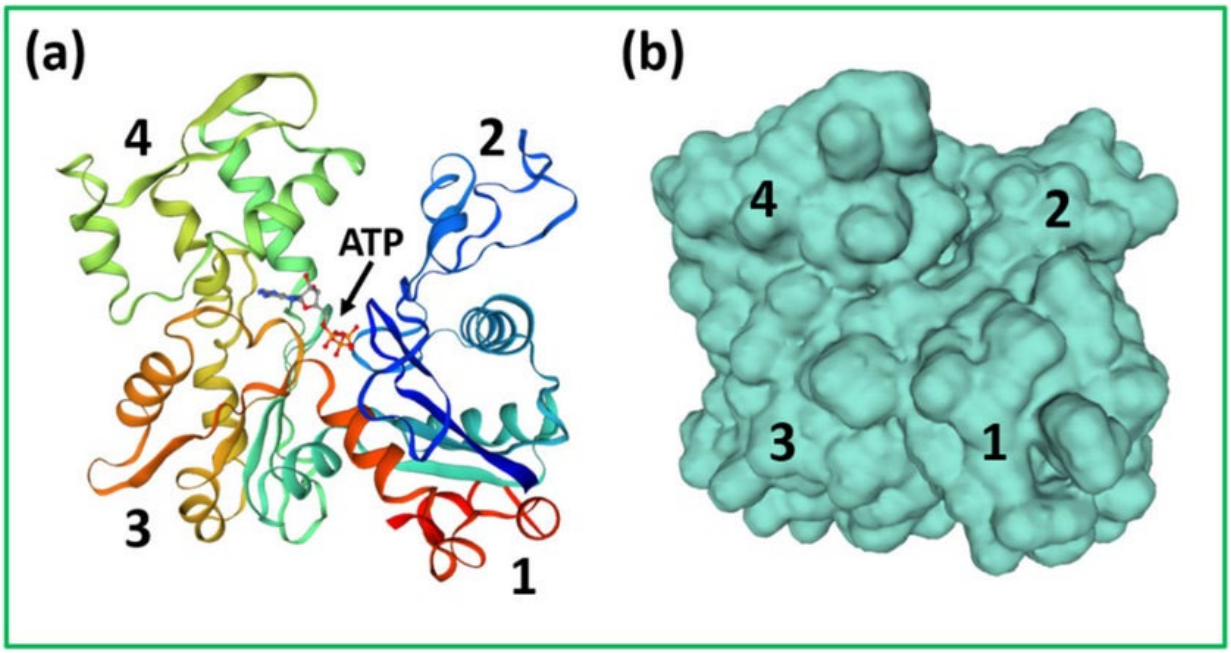

Fig 1.1: Structure of the actin monomer from human cardiac muscle*. The 4 subdomains and central nucleotide binding cleft are shown in a) ribbon diagram and b) surface representation. From Squire, J. (2019). The actin-myosin interaction in muscle: Background and overview. International Journal of Molecular Sciences, 20(22), 5715. (CC BY) license.*

The assembly of the actin filament involves nucleation of actin monomers and elongation. In the nucleation step, actin assembles into dimers and trimers. The trimers elongate based on the reversible addition of monomer to either end, with the barbed end of actin elongating five to ten times faster than the pointed end, at a rate of 11.6 $\mu M^{-1} \cdot s^{-1}$. Formation of actin filaments from G-actin is dependent on monomer concentration; at the critical concentration, the rate of polymerization of monomers into F-actin is equal to the rate of their dissociation (Cooper, 2000; Pollard, 1986; Blanchoin et al, 2014).

F-actin subunits hydrolyze ATP to ADP, leading to an arrangement of ATP-actin monomers in the barbed end of the filament followed by ADP-actin monomers. Since the dissociation of ADP-actin occurs more readily than ATP-actin, the actin filament has a

net loss of ADP-actin monomers from the pointed end that is balanced by addition of ATP-actin subunits to the barbed end. This phenomenon is called actin treadmilling, and results in a constant polymerizable actin concentration (Carlier et al, 2017; Cooper, 2000).

1.2.1 ACTIN ASSOCIATED PROTEINS

Several actin binding proteins (ABPs) interact with actin to regulate filament assembly and disassembly. The WH2 (Wiscott–Aldridge syndrome protein homology domain 2) repeat is found in many ABPs and these ABPs can be classified into several groups based on their interactions with G- and F-actin (Dos Remedios et al, 2003):

1) Proteins that bind G-actin and promote polymerization of the filament. The Profilin family are small proteins of approximately 19 kDa, that are present in all eukaryotes. Profilin binds and sequesters ATP-actin, transporting it to the barbed end through association with formins and promoting filament elongation (Krishnan & Moens, 2009; Zweifel & Courtemanche, 2020). Profilin-actin association is regulated by competitive binding with phosphatidylinositol (4,5)-bisphosphate (PIP2) and proteins with PLP (poly-L-proline) stretches (Goldschmidt-Clermont et al, 1990; Metzler et al, 1994).

2) Proteins that promote actin filament depolymerization by converting F-actin to G-actin. The ADF/Cofilin family of proteins are highly conserved in eukaryotes and most vertebrates have three genes coding for Cofilin 1 (found in non-muscle cells), Cofilin 2 (found in muscle cells) and Destrin (MacIver & Hussey, 2002). ADF/Cofilin protein binding induces conformational change in the actin filament, weaking its structural integrity (McGough et al, 1997). ADF/Cofilin proteins cause F-actin depolymerization in two major ways- 1) by severing the filament, thus creating more ends that undergo disassembly and 2) increasing the off-rate for monomers on the pointed end of the filament by 30-fold and contributing to the treadmilling of actin in concert with profilin (Du & Frieden, 1998; Ressad et al, 1999). Phosphorylation of ADF/cofilin causes loss of affinity for G-actin. This process is further regulated through LIM-kinase proteins that phosphorylate cofilin and Slingshot proteins that dephosphorylate cofilin, thus regulating the rate of F-actin turnover (Sumi et al, 1999; Niwa et al, 2002).

3) Actin monomer binding proteins that prevent polymerization by sequestering G-actin, thus removing them from the pool of available monomers for filament assembly. Examples include Thymosin Beta-4 (Safer et al, 1997), Cyclase associated proteins (Hliscs et al, 2010), Twinfilin (Goode et al, 1998) and DNase I (Weber et al, 1994).

4) Proteins that bind the ends of the actin filament and prevent monomer exchange. Tropomodulin caps the pointed end of the filament, doubling the critical concentration and preventing both elongation and depolymerization (Weber, 1994). Capping protein caps the barbed end of the filament, preventing monomer exchange. Capping protein is highly conserved and along with Tropomodulin, stabilizes the actin filament, thus allowing stable thin filaments found in striated muscle cells. The enrichment of the capping protein in the Z disk leads to its alternate name, CapZ (Cooper & Sept, 2008; Schafer et al, 1995). The capping protein also promotes branched actin nucleation by Arp 2/3 by regulating nucleation promoting factors (Akin & Mullins, 2008; Funk et al, 2021).

5) Proteins that bind the side of F-actin and stabilize the filament. Tropomyosins are coiled coil proteins forming polymers that bind along the α-helical groove of the actin filament. Tropomyosin binding stabilizes the actin filament and regulates the binding of other proteins such as ADF/cofilin. Muscle-specific tropomyosin isoforms regulate contraction in skeletal and smooth muscle. Cytoskeletal isoforms of tropomyosin perform several functions, especially myosin motor recruitment and regulation. (Gunning et al, 2008; Cooper et al, 2002; Clayton et al, 2014; Barua et al, 2014)

6) Proteins that bind the side of F-actin and sever the filament, shortening the average length. The Gelsolin superfamily of proteins is present in all eukaryotes and activated by calcium binding that triggers conformational changes exposing actin interaction domains. Gelsolin regulates actin filaments by capping the barbed end of actin and inhibiting polymerization, as well as severing actin filaments (Laine et al, 1998; Nag et al, 2013). Though Gelsolin can sever filaments when Tropomyosin is bound to F-actin,

Tropomyosin can regulate Gelsolin's severing activity by binding it in solution and preventing association with actin filaments (Khaitlina et al, 2013).

7) Actin crosslinking proteins that possess at least two binding sites for F-actin, forming branched actin networks and filament bundles. Examples include the Arp 2/3 complex, which mediates branched actin nucleation (Pollard, 2007), the actinin family of proteins which forms anti-parallel dimers with calponin homology domains that bind actin on either end (Murphy & Young, 2015), the Fimbrin protein which forms tightly bundled actin filaments (such as in stereocilia and microvilli) (Bretscher, 1981), the Filamin proteins which crosslink actin filaments at orthogonal angles (Nakamura et al, 2011) and the Palladin protein which uses immunoglobulin-like domains in order to bind F-actin (Dixon et al, 2008).

1.3 FOCAL ADHESIONS

Focal adhesions are transmembrane structures composed of integrins and several other associated proteins that connect the cytoskeleton and the extracellular matrix (Burridge, 2017). Identified in 1975 by Abercrombie through Electron Microscopy in fibroblasts, they were identified as 'plaques' on the ventral plasma membrane (Abercrombie et al, 1971). Subsequent studies using Interference Reflection Microscopy and Immunofluorescence Microscopy established important characteristics of adhesions, such as the dynamics of focal adhesion maturation from focal contacts and the prevalence of adhesion associated proteins such as vinculin and talin (Heath & Dunn, 1978; Nobes & Hall, 1995; Geiger,1979; Burridge & Connell, 1983).

Integrins are a superfamily of adhesion receptors that form the major structural unit of focal adhesions. They are heterodimeric, transmembrane proteins consisting of α and β subunits. At least 18 α and 8 β subunits have been identified in humans, generating 24 heterodimers. An arginine-glycine-aspartic acid tripeptide sequence (RGD peptide) serves as a general integrin-binding motif, present in

extracellular matrix ligands such as fibronectin, vitronectin and fibrinogen. Integrin ligand specificity varies by the subunit composition; for example, RGD recognizing integrins (such as $\alpha_5\beta_1$ (primary receptor for fibronectin), $\alpha_V\beta_1$ and $\alpha_V\beta_5$) and laminin/collagen binding integrins (such as α1β1, α2β1, α3β1) (Takada et al, 2007; Barczyk et al, 2010).

Focal adhesions form as small focal complexes consisting of clustered integrins which are activated from a bent conformation to an extended structure with an open headpiece conformation optimized for ligand binding (Takagi et al, 2002). This is followed by recruitment of adaptor proteins such as talin and paxillin, which further promote integrin activation and provide a scaffold for recruitment of many other proteins involved in signaling, mechanotransduction and actin dynamics. Thus, a mature focal adhesion is formed in complex with the actin cytoskeleton, serving as a signaling hub and mechanical link to the extracellular matrix (Legerstee & Houtsmuller 2021).

1.3.1 FOCAL ADHESION ASSOCIATED PROTEINS

Further studies in adhesion proteins over the decades has led to a comprehensive visualization of the nanoscale architecture of adhesions in 2010 (Kanchanawong et al, 2010) using iPalm (interferometric photoactivated localization microscopy) showing three distinct layers-

1) An integrin signaling layer located above the intracellular integrin domains, containing FAK (focal adhesion kinase) and paxillin.

2) A force transduction layer containing talin and vinculin.

3) An actin-regulatory layer containing zyxin, ENA/VASP actin polymerization proteins and actin crosslinking protein alpha-actinin which connects to stress fibers rising from the adhesion.

Paxillin is a key adaptor protein that is essential to focal adhesion formation. It is recruited to early focal adhesions and binds to integrins via its C-terminal LIM domains. It serves as a multidomain scaffolding protein and mediates recruitment of

adhesion components through its N-terminal region which has binding domains that facilitate protein-protein interactions (Schaller, 2001; Deakin & Turner, 2008).

Focal adhesion kinase is a non-receptor tyrosine kinase that is activated by autophosphorylation. The N-terminal FERM domains (F for 4.1 protein, E for ezrin, R for radixin and M for moesin) direct interaction with integrins and growth factor receptors while the C-terminal domain mediates protein-protein interactions such as with paxillin, the Src family of kinases and cas protein. FAK is instrumental in focal adhesion turnover and migration (Parsons, 2003; Mitra, Hanson, & Schlaepfer, 2005).

Talin is a large adaptor protein consisting of an N-terminal FERM domain and C-terminal rod domains that contain alpha-helices. The globular head domain of talin binds beta-integrins and promotes integrin activation (Calderwood et al, 1999). The tail domain of talin mediates mechanosensitive binding to vinculin, resulting in its activation. The tail domain can also bind actin directly, thus talin acts as a structural link between integrin and actin across the adhesion's protein layers, acting as the tension-bearing core of the focal adhesions (Critchley & Gingras, 2008; Critchley, 2009; Liu et al, 2015).

Vinculin is a mechanosensitive protein in focal adhesions consisting of a globular N-terminal domain mediating interactions with talin and alpha-actinin and a C-terminal tail domain mediating interactions with actin and paxillin. Vinculin promotes adhesion growth by facilitating integrin activation and clustering (Humphries et al, 2007). Vinculin transmits forces generated by myosin contractility through the adhesion, regulating cell area and traction force coupling (Ziegler et al, 2006; Dumbauld et al, 2013; Atherton et al, 2016).

Zyxin is a mechanosensitive protein that localizes to focal adhesion and sites on actin stress fibers under mechanical stress. The N-terminal region of zyxin has proline-rich motifs that mediate its interactions with proteins such as ENA/VASP and alpha-actinin, while the C-terminal region of zyxin consists of three tandem LIM domains that mediate its localization to focal adhesions (Drees et al, 2000; Li et al, 2001; Yoshigi et al, 2003; Uemura et al, 2011). Localization of zyxin is highly force-dependent; loss of contractile

forces by chemical inhibition or severing an associated stress fiber increases its dissociation rate from the focal adhesion (Rottner et al, 2001; Lele et al, 2006). Zyxin facilitates actin polymerization at the adhesion by recruiting ENA/VASP proteins as well as the repair and mechano-induced reinforcement of stress fibers (Hoffman et al, 2006; Hoffman et al, 2012; Hirata et al, 2008; Hirata et al, 2008; Smith et al, 2010).

Alpha-actinins are dimeric proteins that belong to the spectrin superfamily. Adhesions mature along the template of actin crosslinked by alpha-actinin, which also acts as a linker to transduce forces between the stress fiber and mature adhesions (Choi et al, 2008; Sjöblom et al, 2008; Roca-Cusachs et al, 2013).

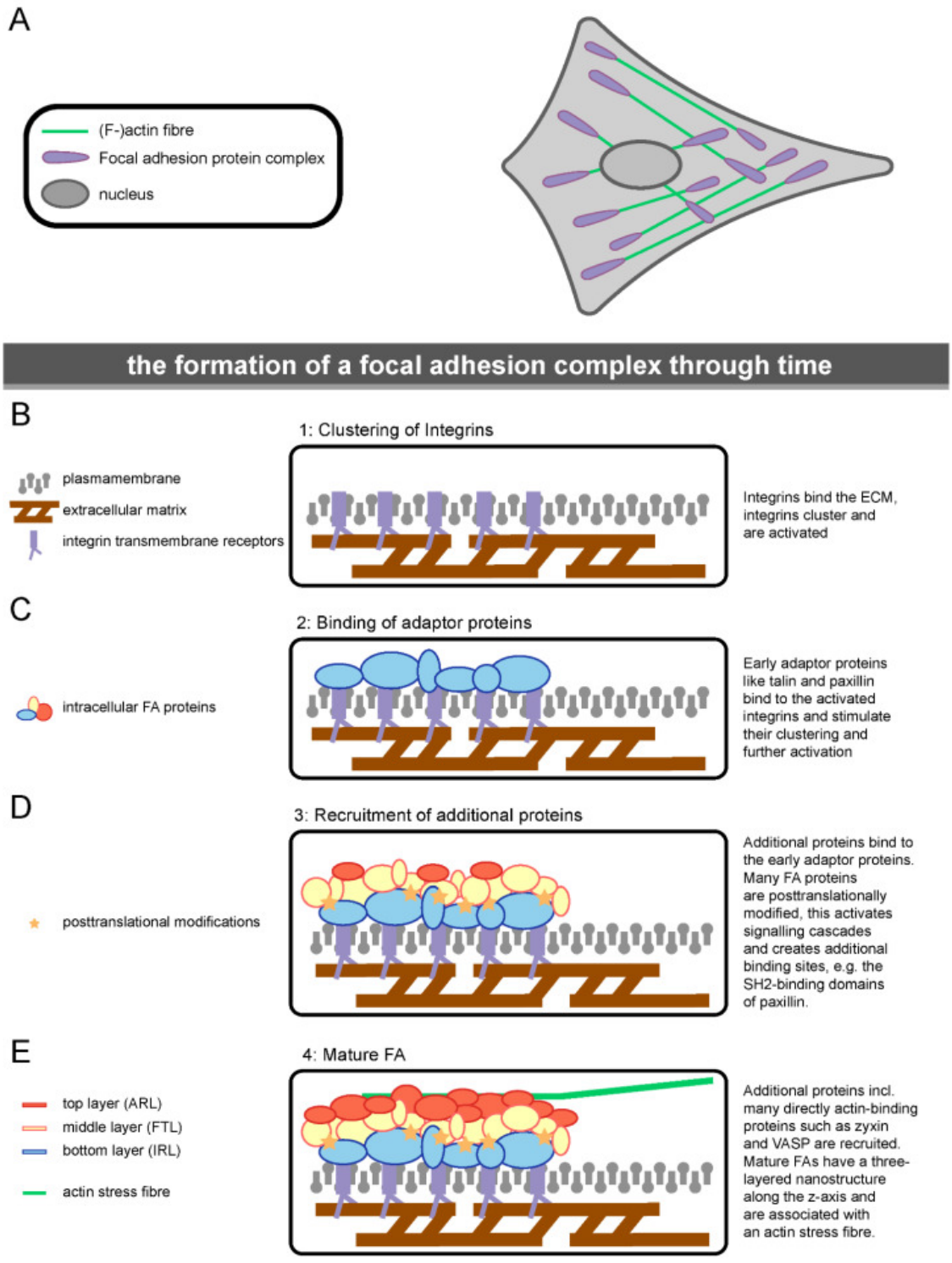

Fig 1.2: Step-by-step maturation of focal adhesions*. From Legerstee, K., & Houtsmuller, A. B. (2021). A Layered View on Focal Adhesions. Biology, 10(11), 1189. (CC BY) license.*

1.4 ACTIN STRESS FIBERS: TYPES AND FUNCTIONS

Stress fibers are higher order actin structures comprised of 10-30 actin filaments bundled by the crosslinking protein alpha-actinin (Cramer et al, 1997; Lazarides & Burridge, 1975). Stress fibers were first observed in non-muscle cells almost a century ago (Lewis & Lewis, 1924) and have been studied in the decades since as long actin filaments stretching across the cell that are closely associated with focal adhesions.

By 1998 (Small et al, 1998), stress fibers in migrating cells were classified as dorsal stress fibers, transverse arcs and ventral stress fibers based on their positions and attachment to focal adhesions. Research in the years since have shed further light on how these subtypes are formed in the cell and their functional significance.

Dorsal stress fibers are non-contractile fibers crosslinked by alpha-actinin and attached to a focal adhesion at their distal end. Dorsal stress fibers form by actin polymerization from the focal adhesion in an mDia-1 dependent manner (Hotulainen & Lappalainen, 2006). These fibers have unipolar actin filaments with the barbed ends arranged towards the adhesion (Deguchi & Sato, 2009), and Rac-1 has been observed to be instrumental in their assembly (Kovac et al, 2013). Dorsal stress fibers rise from the ventral to the dorsal plane of the cell while associated with transverse arcs at their proximal end and transduce forces produced by the contractile arcs to focal adhesions (Burnette et al, 2014).

Transverse arcs are contractile, curved fibers that are arranged parallel to the leading edge of the cell. They are formed by the rearward flow of actin from the lamellipodium, through the end-to-end annealing of bundles containing non-muscle myosin-II (recruited by mDia2) and alpha-actinin crosslinked actin bundles that are derived from the branched actin network nucleated by Arp 2/3 at the leading edge of the cell. This leads to alternating localizations of alpha-actinin and myosin across the arcs, forming a contractile structure (Hotulainen & Lappalainen, 2006; Tojkander et al, 2011; Burnette et al, 2011).

Ventral stress fibers are contractile fibers found in the ventral plane of the cell and attached to a focal adhesion at each end. They are contractile structures with mixed polarity, crosslinked by alpha-actinin and non-muscle myosin II. Ventral stress fibers have different lengths and are variously oriented in the cell. Small ventral fibers (referred as cortical stress fibers) have been shown to form by condensation of the cortical actin meshwork by non-muscle myosin II pulses, with two nascent adhesions anchoring either end of the forming cortical stress fiber (Lehtimäki et al, 2021). These fibers are thinner, more dynamic and less contractile compared to prominent ventral stress fibers in the cell. Long ventral stress fibers in U2OS cells have been observed to form from the actin crosslinking of dorsal stress fibers with transverse arcs where two dorsal stress fibers attached to a section of transverse arc transform into a straight fiber through contractile forces (Hotulainen & Lappalainen, 2006). In addition to these mechanisms of formation, the dynamic reorganization of ventral stress fibers needs further investigation. Early observations of ventral actin dynamics in spreading cells after Latrunculin B washout assays showed that actin polymerization at adhesions coupled with adhesion dynamics lead to remodeling of the ventral actin network (Zimerman et al, 2004). Such ventral stress fiber remodeling had also been theorized (Small et al, 1998) as a method for VSF elongation. Our investigations of ventral stress fiber remodeling build on these observations to describe how smaller ventral fibers can 'merge' at focal adhesions through a process involving contractile annealing of merging fibers and adhesion disassembly to form a single, longer ventral fiber. This study is described in detail in Chapter 2.

Stress fibers have functional roles in cellular force generation and motility. Dorsal stress fibers and transverse arcs at the leading edge promote adhesion maturation through actin polymerization by providing tension forces as well as a structural template for the assembly of adhesion components (Parsons et al, 2010; Oakes et al, 2012). Ventral stress fibers function in retraction of the trailing edge in migrating cells by producing contractile forces (Vicente-Manzanares et al, 2011). Experiments with laser nanosurgery have shown that ventral stress fibers are under the highest tension of all the stress fiber

subtypes (Lee et al, 2018) and model-based traction force microscopy has shown that ventral stress fibers produce the strongest traction forces of all the stress fiber subtypes (Soiné et al, 2015). Ventral stress fibers also influence the direction of migration by reorienting towards the long axis through separating and attaching to different adhesions, acting as a 'rudder' for the migrating cell (Rid et al, 2005).

1.5 METHODS OF ACTIN STRESS FIBER AND FOCAL ADHESION ANALYSIS

Actin stress fibers and focal adhesions are structurally and functionally linked through mechanical tension and regulated by contractile forces stimulated by RhoA (Chrzanowska-Wodnicka & Burridge,1996). Nascent adhesions at the leading edge mature in the direction of actin flow and act as a molecular clutch that couple the force of actin polymerization with the forward momentum in the lamellipodium. (Case & Waterman, 2015). Stress fiber subtypes are characterized by their attachment to adhesions, which in turn signify their location and functional relevance in the cell (Vallenius, 2013). The linked dynamics of these structures lead to linked phenotypes such that changes in the number and distribution of stress fibers are accompanied by a corresponding change in focal adhesions as well.

Inspite of the interdependence of stress fibers and adhesions, the quantitative analysis of actin stress fibers and focal adhesions in cellular studies have largely been carried out using separate channels employing either manual evaluation or with the help of computational tools. To facilitate the quantification of each structure, a number of software tools and methodologies have been developed that investigate the characteristics and dynamics of either focal adhesions or stress fibers.

To analyze focal adhesions in cells at a basic level, scientists can identify them through thresholding and segmentation algorithms in image analysis softwares such as Fiji. Such analysis has issues of reproducibility and bias along with being very labor-intensive. Algorithms developed by Buskermolen, et al (Buskermolen et al, 2018) and

Broussard, et al (Broussard et al, 2015) facilitate this process by automating quantitative analysis and providing characteristics of the adhesions. The Focal Adhesion Analysis Server (Berginski & Gomez, 2013) provides a computational tool for automated analysis of adhesions in static images and videos, facilitating analysis in large datasets. Similarly, analysis of actin filaments and fibers in cells can be performed through segmentation in image analysis softwares, facilitated by MATLAB algorithms (Rogge et al, 2017) and computational tools such as Filament Sensor (Eltzner et al, 2015), CytoSeg (Nowak et al, 2020) and SFEX (Zhang et al, 2017).

While scientists could thoroughly analyze focal adhesions or stress fibers through these methods, a single computational tool that coupled their analysis was still not present. Thus, we created an integrated focal adhesion-stress fiber analysis module called the Focal Adhesion Filament Cross-correlation Kit (FAFCK). This computational tool has a Focal Adhesion Sensor module for adhesion detection and characterization, a Filament Sensor module for filament detection and analysis as well as a correlation module for coupled focal adhesion-stress fiber detection and analysis. This tool is suited to analyzing large datasets and provides an evaluation module to optimize custom processing of images. By correlating the filaments with adhesions, the tool provides information on stress fiber subtypes on basis of adhesion association which would prove vital to characterize specific phenotypes of stress fiber architecture in cellular studies. This computational tool is introduced in depth in Chapter 3.

CHAPTER 2:

MERGING OF VENTRAL FIBERS AT ADHESIONS DRIVES THE REMODELING OF CELLULAR CONTRACTILE SYSTEMS IN FIBROBLASTS.

This chapter is published in bioRxiv and submitted under the same title to Cytoskeleton.

Narasimhan, S., Holmes, W. R., & Kaverina, I. (2022). Merging of ventral fibers at adhesions drives the remodeling of cellular contractile systems in fibroblasts. *bioRxiv*.

2.1 ABSTRACT

Ventral stress fibers (VSFs) are contractile actin fibers present in the ventral plane of the cell and existing in a dynamic attachment with cell-matrix focal adhesions. VSFs are critical in cellular mechanobiological functions such as traction force production, cell polarization, and migration. VSF within their intracellular network vary from short, thinner fibers that are randomly oriented to long, thick fibers that span along the whole long axis of a cell. *De novo* VSF formation was shown to occur by condensation from the cortical actin mesh or by crosslinking of other stress fiber subtypes (dorsal stress fibers and transverse arcs) at the cell front. However, formation of long VSFs that extend across the whole cell axis is not well understood. Here, we report a novel phenomenon of VSF merging in migratory fibroblast cells, which is guided by mechanical force balance and contributes to VSF alignment along the long cell axis. The mechanism of VSF merging involves two steps: connection of two ventral fibers by an emerging myosin II bridge at an intervening adhesion and intervening adhesion dissolution to form a cohesive, contractile VSF. Our data indicate that these two steps are interdependent, since under conditions where adhesion disassembly is slowed, formation of the myosin bridge is slowed as well. Cellular data and computational modeling show that the angle of contact between merging fibers decides successful merging, with angles closer to 180 yielding merging events and shallower angles leading to merge failure. Our data and modeling further show

that merging increases the share of uniformly aligned long VSFs, which would contribute to directional traction force production. Thus, we thoroughly characterize merging as process for dynamic reorganization of VSFs in steady state, investigating the steps and variants of the process as well as its functional significance in migratory cells.

2.2 INTRODUCTION

The actin cytoskeleton in a cell plays an integral role in cell polarization, migration, and force production (Burridge & Wittchen, 2013). Filamentous actin structures in migrating cells include branched and interlocked networks found in lamellipodium and the cortical mesh, parallel actin bundles in filopodia and antiparallel actin bundles in stress fibers (Hohmann & Dehghani , 2019). Actin stress fibers are higher order structures formed by crosslinked bundles of 10-30 actin filaments (Cramer et al, 1997). Actin stress fibers and focal adhesions are closely linked in terms of structure and dynamics (Gardel et al, 2010; Ciobanasu et al, 2012; Burridge & Guilluy, 2016). Actin polymerization initiates in nascent focal contacts (Choi et al, 2008), while further maturation of focal adhesions depends on both the tension applied and the structural template offered by the growing actin filament (Oakes et al, 2012).

Stress fibers in a migrating mesenchymal cell can be divided into three main subtypes based on their location and attachment to focal adhesions – dorsal stress fibers, transverse arcs and Ventral Stress Fibers (VSFs), as depicted in **Fig 2.1A** (Small et al, 1998; Pellegrin & Mellor, 2007; Vallenius, 2013; Letort et al, 2015). Dorsal stress fibers are non-contractile fibers that are crosslinked by alpha-actinin. They are attached to the substrate through a single focal adhesion at their distal end and rise from the bottom to the top of the cell (Hotulainen & Lappalainen, 2006; Kovac et al, 2013). Transverse arcs are curved, contractile, α-actinin- and myosin II-associated actin bundles that form an interconnected network with dorsal stress fibers, rising to the upper planes of the cell. Transverse arcs are not attached to focal adhesions, and their contractile forces are

transduced to the substrate by dorsal stress fibers and their associated adhesions (Hotulainen & Lappalainen, 2006; Heath, 1983; Burnette et al, 2014).

Ventral stress fibers (VSFs) are arguably the most significant actin assemblies in a migrating mesenchymal cell. They are prominent, discrete contractile fibers in the ventral plane of the cell, consisting of actin filaments crosslinked by alpha-actinin and associated with myosin II stacks. They are attached to the substrate through a focal adhesion at each end. VSFs exist in many lengths and various angles with respect to the main cell axis, with longer VSFs more aligned towards the major axis of the cell. They produce the majority of cellular traction forces and are instrumental in rear retraction during migration (Small et al, 1998; Livne & Geiger, 2016; Soiné et al, 2015; Ghilardi et al, 2021). Although these important structures have been described several decades ago, their dynamics and mechanics are far from being fully understood.

In a migrating cell, the actin cytoskeleton undergoes continuous polymerization and depolymerization as well as remodeling of the actin filament organization within existing fibers and networks. Early studies of actin dynamics in embryonic chick heart fibroblasts visualized by microinjected tetramethylrhodamine-actin indicated complex remodeling of existing fibers and bundles with multiple fusion and splitting events (Wang, 1984).

Later, a series of major studies more specifically targeted the origin of VSFs during cell migration. It was shown that VSF formation in osteosarcoma (U2OS) cells occurs by fiber crosslinking between stress fiber subtypes in upper cell planes. During this process, two non-contractile dorsal stress fibers connect with the ends of a contractile transverse arc, leading to formation of a VSF. When the structure resolves into a straight fiber, the focal adhesions of the dorsal stress fibers are found at both ends of the newly formed prominent VSF (Hotulainen & Lappalainen, 2006; Tojkander et al, 2015). A different scenario has been described for thinner, smaller cortical stress fibers, which can form by condensation of cortical actin mesh between two adhesions in the ventral plane of the cell (Lehtimäki et al, 2021; Vignaud et al, 2021). In addition to those *de novo* VSF

formation mechanisms, the number of VSFs can be increased by remodeling of the existing VSF network; when large focal adhesions undergo splitting; so that each fiber it is attached to becomes a new VSF as a result (Young & Higgs, 2018).Altogether, the dynamics of VSF initiation has been fairly well studied. In contrast, VSF remodeling beyond their formation has not been analyzed in such great detail. One question left behind is how short VSFs formed close to the cell edge are transformed into long ones. Because VSFs provide forces to contract the cell body in the direction of movement, it is essential that they extend all the way along the long cell axis. Our study reported here is a step into understanding the interplay of adhesion dynamics, actin bundle remodeling and myosin contractility-driven forces, leading to VSF extension and alignment necessary for efficient cell movement.

We report a method of VSF extension in migrating fibroblasts that involves the merging of two ventral fibers at an intervening adhesion by formation of a myosin-II bridge to form a single VSF. In contrast to previously described VSF formation processes, this merging does not involve fibers from upper cell layers but occurs solely in the ventral cell plane. By experimental and computational means, we find that adhesion dynamics is a critical step for VSF merging, and that merging efficiency is guided by contractile forces exerted to the adhesion by myosin contractility. We observe that the merging process is used for dynamic reorganization of VSFs in steady state according to cellular needs such as forming protrusions, cell turning or simply to change the distribution of VSFs in the cell. In this paper we thoroughly characterize merging as a new paradigm for remodeling the ventral contractile system in cells.

2.3 RESULTS AND DISCUSSION

2.3.1 VENTRAL STRESS FIBERS REMODEL BY MERGING AT INTERVENING FOCAL ADHESIONS

To analyze dynamics of ventral contractile cytoskeleton in motile MRC5 cells *(lung fibroblast cells, ATCC®),* we visualized contractile fibers and focal adhesions by expression of GFP-Myosin light chain and mCherry-Vinculin respectively. These data revealed that in process of their reorganization, VSFs consistently merge at intervening focal adhesions (**Fig 2.1B**). In each merging event, a pre-existing VSF (referred to as a primary fiber) becomes involved in merging as a newly forming VSF (referred to as a secondary fiber) attaches to one of its end adhesions (referred to as an intervening adhesion).

While the primary fiber may arise by various mechanisms and exist in a cell for a significant time prior to merging, the secondary fibers predominantly form anew (**Fig 2.1C**). Visualization of GFP-Utrophin indicates that secondary fibers arise from the disordered actin mesh by spontaneous condensation of the mesh into discrete fibers. This effect is similar to cortical stress fiber formation (Lehtimäki et al, 2021), except that instead of forming with two adhesions on each end, the secondary fibers formed proceed to attach to a preexisting primary fiber for further consolidation into a VSF. Interestingly, a similar process of actin condensation between two adhesions with subsequent stress fiber fusion was described during reassembly of the actin network following complete actin depolymerization in Latrunculin B washout assays (Zimerman et al, 2004). This suggests that a newly forming secondary fiber possibly involves not only condensation of preexisting actin filaments but enhanced actin polymerization at these sites.

After attachment of the secondary fiber to the intervening adhesion, the primary and secondary fibers are bridged by contractile material as visualized by myosin incorporation. In parallel, the intervening adhesion dissolves and the structure is seamlessly joined into a single, straight, contractile fiber (**Fig 2.1B**).

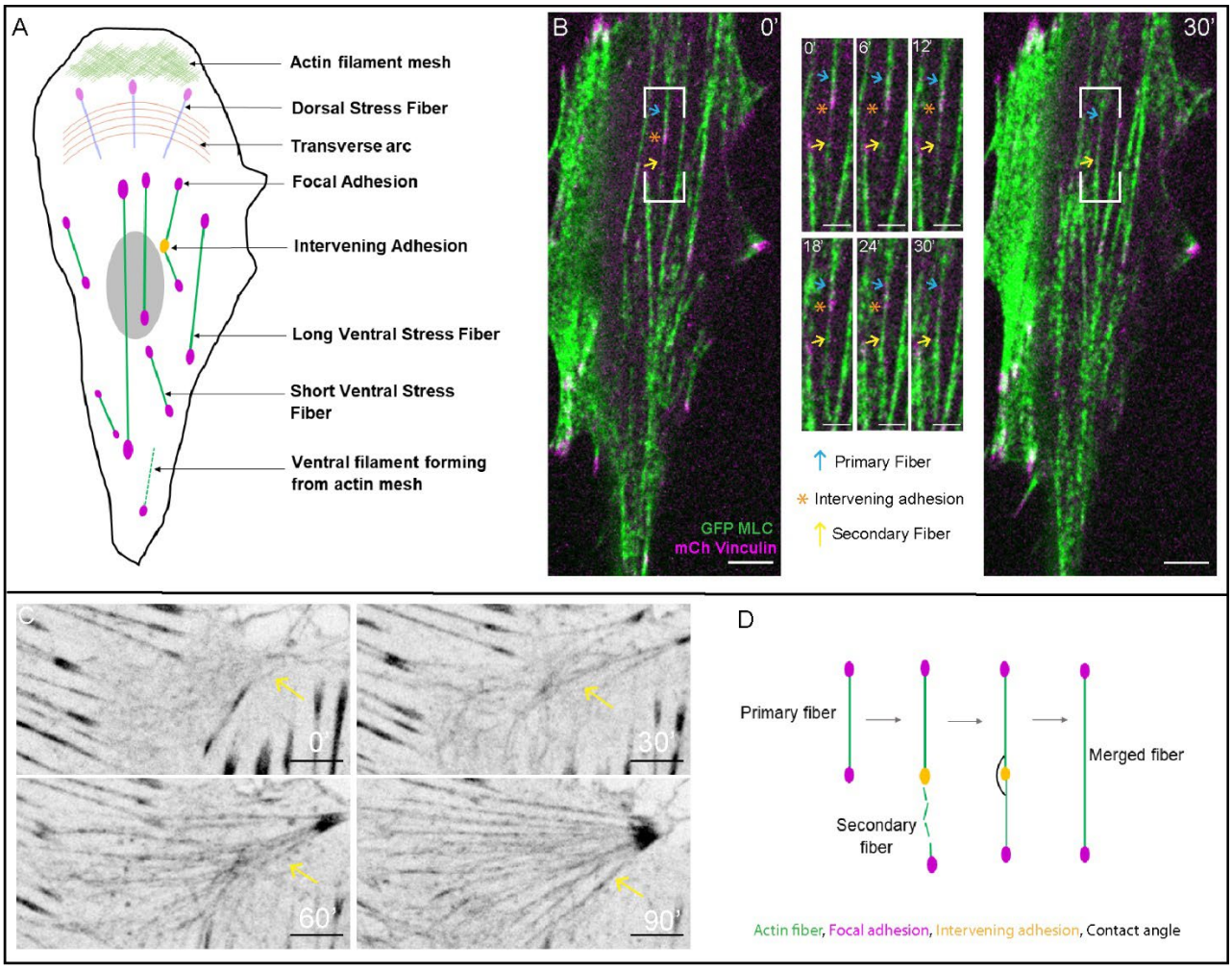

Figure 2.1: Ventral stress fibers remodel by merging at intervening focal adhesions

A) Schematic of ventral view of a migrating cell with different actin stress fibers marked. The green fibers denote ventral stress fibers (VSFs) at the bottom plane attached to magenta focal adhesions on either end. VSFs are of many lengths and variably oriented along the cell's main axis. Two VSFs are shown merging with an intervening adhesion between. Formation of actin fiber by coalescence from the actin mesh is marked. Stress fiber subtypes in upper z planes such as dorsal stress fibers and transverse arcs are also shown in faded colors. B) Ventral plane timelapse of MRC5 cell plated on 1 µg/ml Fibronectin substrate expressing GFP-Myosin Light Chain (MLC, green) and mCherry Vinculin (magenta) showing a merging event. Boxes on cell images at 0 min and 30 min note position of the merge event in the insets. Insets show merge event where a newly formed secondary ventral fiber (yellow arrow) is attached to the primary ventral fiber (Blue

arrow) at the intervening adhesion (orange asterisk). As the intervening adhesion dissolves, the merging fibers are joined into a single merged ventral fiber by 30 min. Scale bar= 10 μm (all). C) Ventral plane timelapse of MRC5 cell plated on 10 μg/ml Fibronectin substrate expressing GFP- Utrophin showing secondary fiber formation by actin mesh condensation. The disordered actin mesh in 0 min condenses spontaneously into filaments. Scale bar= 10 μm. D) Schematic of merging showing a pre-existing primary fiber attached to two adhesions. Secondary fiber forms and attaches to an end adhesion, which becomes the intervening adhesion. As the intervening adhesion disassembles, the two fibers are merged into one. Black arc denotes contact angle of the merging fibers.

In addition to the most common scenario of merging described above, we found variants on the process (**Fig 2.S1**). One variation occurs when the merging fibers pull away from the intervening adhesion (**Fig 2.S1A,B**). Then, adhesion can dissolve on its own (7% of events) or at the lateral side of the merging fibers (12% of events). We reason that in such scenarios, adhesion dissolution is not likely to be a limiting factor of the merging process. The second variation involves splitting of the primary fiber along its length**,** so that part of the primary fiber merges with the secondary fiber and the other part exists as an independent VSF (**Fig 2.S1C,D,** 15% of events). Finally, while in the majority of events secondary fiber is newly formed, a pre-existing VSF can also play this role. In such cases (12% of events), a part of pre-existing secondary fiber attaches to the intervening adhesion and continues merging into a new VSF, while the rest of the pre-existing fiber disassembles (**Fig 2.S1E,F**).

All variants of the merging process are not mutually exclusive and, in different combinations, provide a significant flexibility to VSF remodeling. In most cases, we observe that VSFs formed by merging are relatively long and thick compared to the thinner, smaller cortical stress fibers (Lehtimäki et al, 2021, our observations). At the same time, VSF formation via merging of transverse arcs with dorsal stress fibers (Hotulainen & Lappalainen, 2006) is rarely observed in MRC5 fibroblasts. Thus, VSF merging which

combines preexisting ventral fibers and actin mesh in the cell can be considered a most efficient method of large VSF formation in this cell type. We suggest that it is a significant part of contractile cytoskeleton remodeling in motile mesenchymal cells.

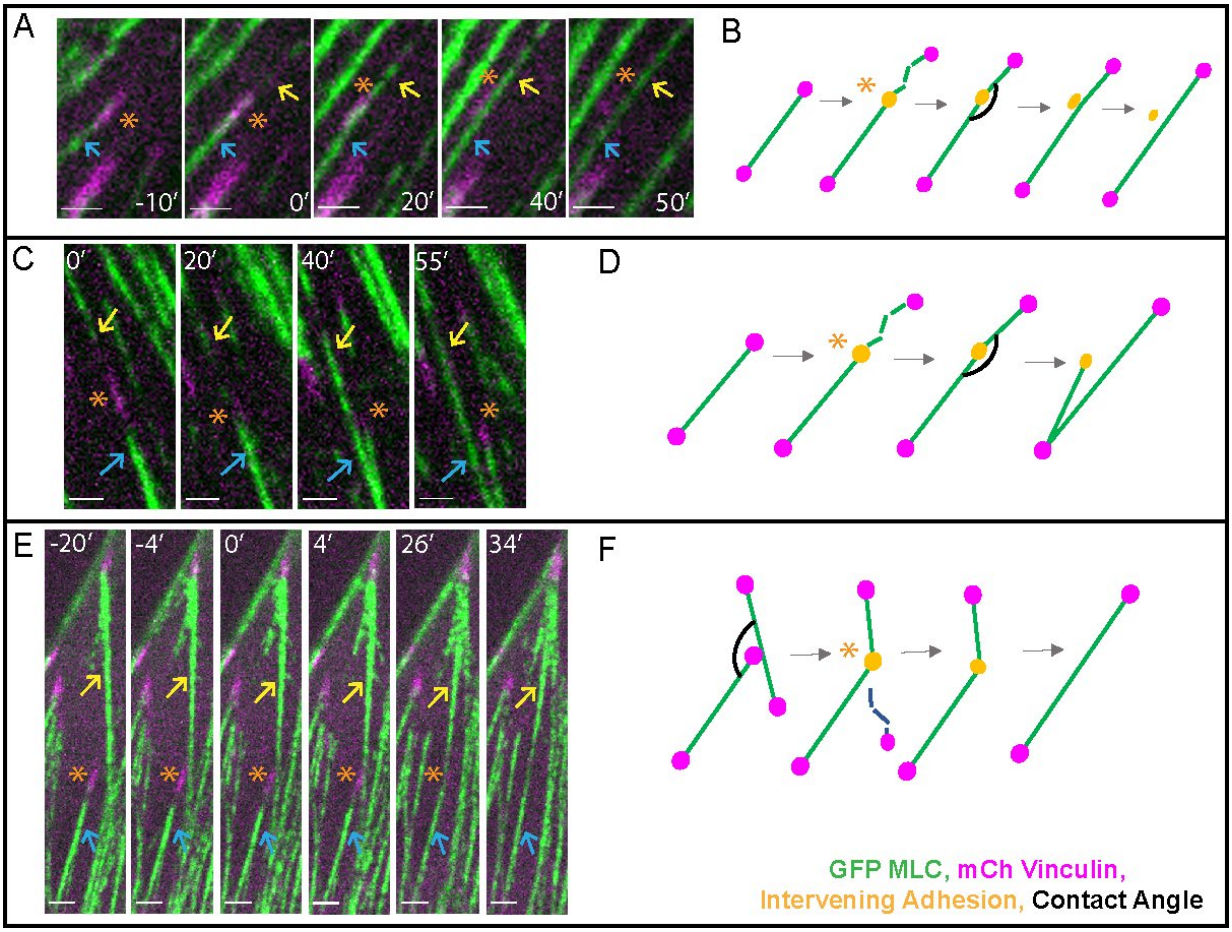

Figure 2.S1: *A) Ventral plane timelapse of MRC5 cell plated on 20 µg/ml Fibronectin substrate expressing GFP-Myosin Light Chain (MLC, green) and mCherry Vinculin (magenta) showing a merging event. The merged fiber pulls off the intervening adhesion after the myosin bridge is formed in this event. Scale bar= 10 µm. B) Schematic shows the merging process in the event in A. C) Ventral plane timelapse of MRC5 cell plated on 20 µg/ml Fibronectin substrate expressing GFP-Myosin Light Chain (MLC, green) and mCherry Vinculin (magenta) showing a merging event. The primary fiber and intervening adhesion split from the merged fiber after the myosin bridge is formed in this event. Scale*

bar= 10 μm. D) Schematic shows the merging process in the event in C. E) Ventral plane timelapse of MRC5 cell plated on 10 μg/ml Fibronectin substrate expressing GFP-Myosin Light Chain (MLC, green) and mCherry Vinculin (magenta) showing a merging event. The secondary fiber is a pre-existing ventral stress fiber unlike most events, where it forms anew. After attachment to the intervening adhesion, part of the secondary fiber disassembles, and the primary and secondary fibers are merged. Scale bar= 5 μm. F) Schematic shows the merging process in the event in E.

2.3.2 TWO STEPS OF THE MERGING PROCESS: CONTRACTILE "BRIDGE" AND ADHESION DISSOLUTION

Based on our observations, in order to form a uniform, merged VSF two main steps are needed: (1) formation of the myosin-containing bridge between the primary and secondary fiber over the intervening adhesion and (2) the dissolution of the intervening adhesion. Those steps are readily detected by myosin and vinculin dynamics at the point of merging **(Fig 2.2A)**. To investigate the formation of the myosin bridge and adhesion disassembly, we analyzed myosin and vinculin intensity by linescans at the merge point over time (see representative graphs of linescans in specific frames, **Fig 2.2B**). Myosin bridge formation is manifested in the intensity of myosin at the merging point reaching the same level as myosin intensity in the initial primary fiber (**Fig 2.2C**, see methods for analysis details*).* At the same time, the maximum intensity of vinculin over the merge point decreases to cellular background levels as the adhesion disassembles (**Fig 2.2C**). These data indicate that both fiber crosslinking and adhesion dissolution are structural steps potentially important for formation of a new VSF. We propose that contractile cohesion through myosin bridging at the merge point plays a major role in forming a functionally integral fiber. In addition, the initial step to join the separate fibers could involve an actin crosslinking protein, such as alpha-actinin, which is involved in filament bundling in VSFs (Tojkander et al, 2012) and is enriched at focal adhesions (Kanchanawong et al, 2010; Ye et al, 2014). Another important question is how adhesion

dissolution couples into the connection of primary and secondary fibers during merging. As mechanosensitive signaling hubs, focal adhesions and actin dynamics are closely linked (Gardel et al, 2010; Gupton & Waterman-Storer, 2006). Thus, investigating how the rate of adhesion disassembly affects fiber joining is needed to understand VSF merging.

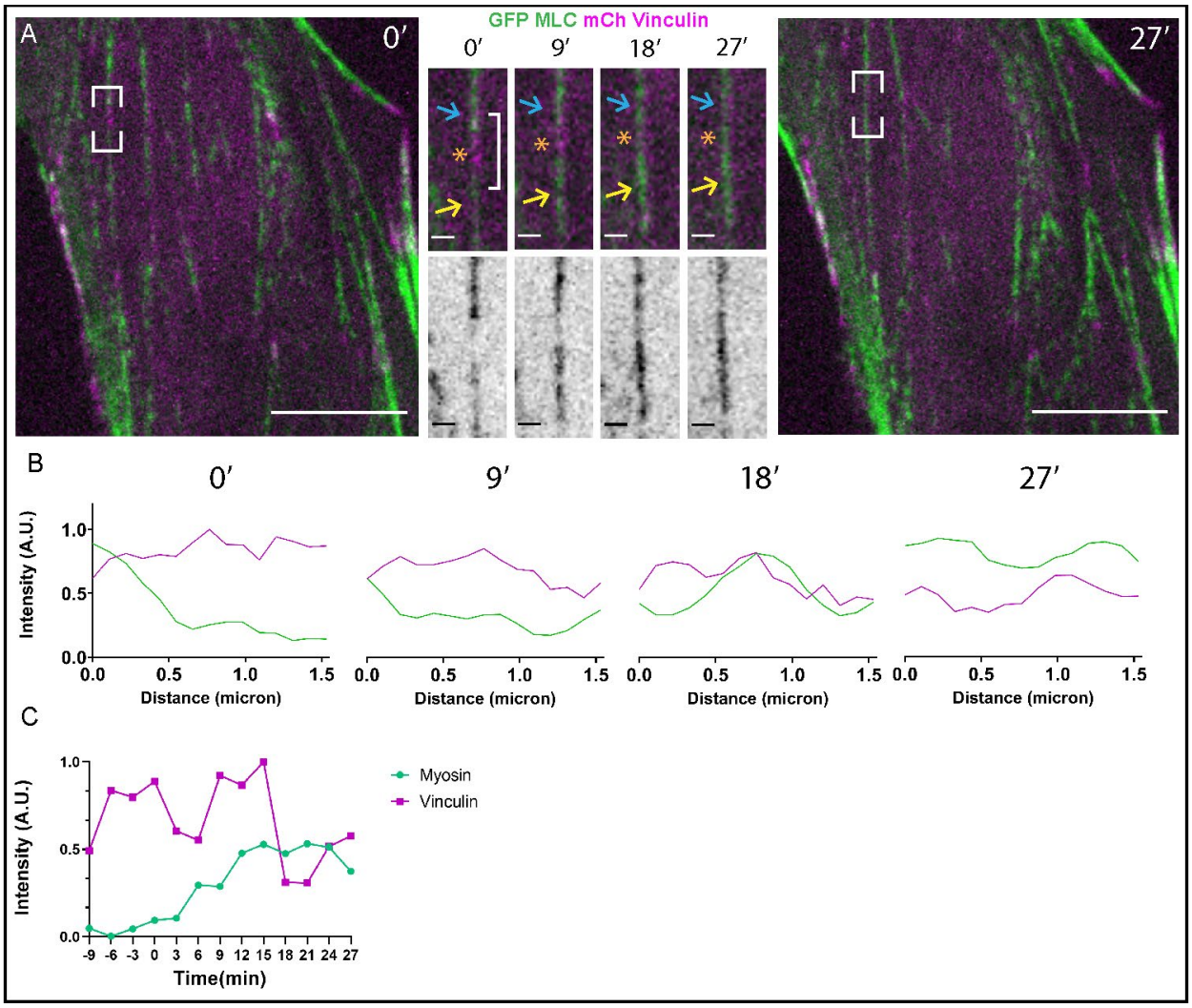

Figure 2.2: Myosin bridge formation over the intervening adhesion connects the merging fibers

A) Ventral plane timelapse of MRC5 cell plated on 1 µg/ml Fibronectin substrate expressing GFP-Myosin Light Chain (MLC, green) and mCherry Vinculin (magenta)

showing a merging event. Boxes on cell images at 0 min and 27 min note position of the merge event in the insets. Insets show the point of merging from 0 min (secondary fiber (yellow arrow) attachment to intervening adhesion (asterisk- orange above, red below) of primary fiber (blue arrow)), 9 and 18 min with merge-in-progress, 27 min with a merged fiber. Myosin bridges over the initial gap in place of the intervening adhesion as the fibers join, as seen by the continuous signal over the fiber. Scale bar= 10 μm (cell), 1 μm (insets). B) Plot profiles of Vinculin (magenta) and Myosin (green) intensity over length of the intervening adhesion at each time point. The vinculin peak at 0 min decreases as the intervening adhesion dissolves and the myosin signal increases by 27 min as the fibers are joined by the myosin bridge. C) Graphs of myosin and vinculin intensity parameters at the merge point over time. Myosin is denoted by ratio of minimum/maximum intensity, vinculin is denoted by maximum intensity.

2.3.3 ADHESION DISASSEMBLY IS NEEDED FOR EFFICIENT MERGING

We investigated the importance of intervening adhesion disassembly in merging by plating cells on substrates with varying concentrations of fibronectin- low Fn (1 μg/ml) substrate and high Fn (20 μg/ml) substrate.

Interestingly, we found that VSF merging occurs faster on low Fn substrate (**Fig 2.3A**) compared to similar event on high Fn substrate (**Fig 2.3B**). Measuring the time taken to form a uniform fiber by merging showed a significant difference between low and high Fn conditions (**Fig 2.3C**). Investigating the dynamics at the point of merging further, we found that myosin bridge formation is also delayed in high Fn concentrations (**Fig 2.3D**). High fibronectin substrate concentration has been established to delay adhesion disassembly (Brennan & Hocking, 2016). Indeed, analyzing adhesion disassembly rates in our cell model with the Focal Adhesion Analysis Server (FAAS) (Berginski & Gomez, 2013) show that rates in high Fn concentration are significantly slower than those in low FN concentration (**Fig 2.3E**).

We surmise that the physical presence of the persistent adhesion in high FN conditions delays building of the contractile bridge, thus contributing to the overall delay in the merging process.

This result is not unexpected given the mechanosensitive nature of adhesion-stress fiber dynamics. We envision that when the adhesion plaque is present, tensile forces produced by both primary and secondary fibers are transmitted to the substrate (ECM), thus there is not strong force in the future bridge region. This would slow down mechanosensitive rearrangement of actin and completion of the merge. From the molecular point of view, mechanosensitive processes in effect in merging can involve not only myosin incorporation but also actin polymerization, for example via mechanosensitive mDia-1-mediated process (Riveline et al, 2001; Valencia et al, 2021). Another element that could contribute to this dependency is that organization of the actin filament bundle associated with focal adhesions differs from the actin arrangement within a contractile fiber (Martins et al, 2021). It is possible that the presence of adhesion proteins prevents a significant region of antiparallel actin filament overlap sufficient for efficient myosin incorporation.

It is important to keep in mind that adhesion dynamics also depends on tensile force applied to the adhesion by associated stress fibers (Wolfenson et al, 2011; Dumbauld et al, 2010; Parsons et al, 2010). The balance of forces from both primary and secondary fibers would lead to growth vs disassembly of the intervening adhesion as a consequence of merging and provide mechanical feedback between adhesion dynamics and fiber merging process.

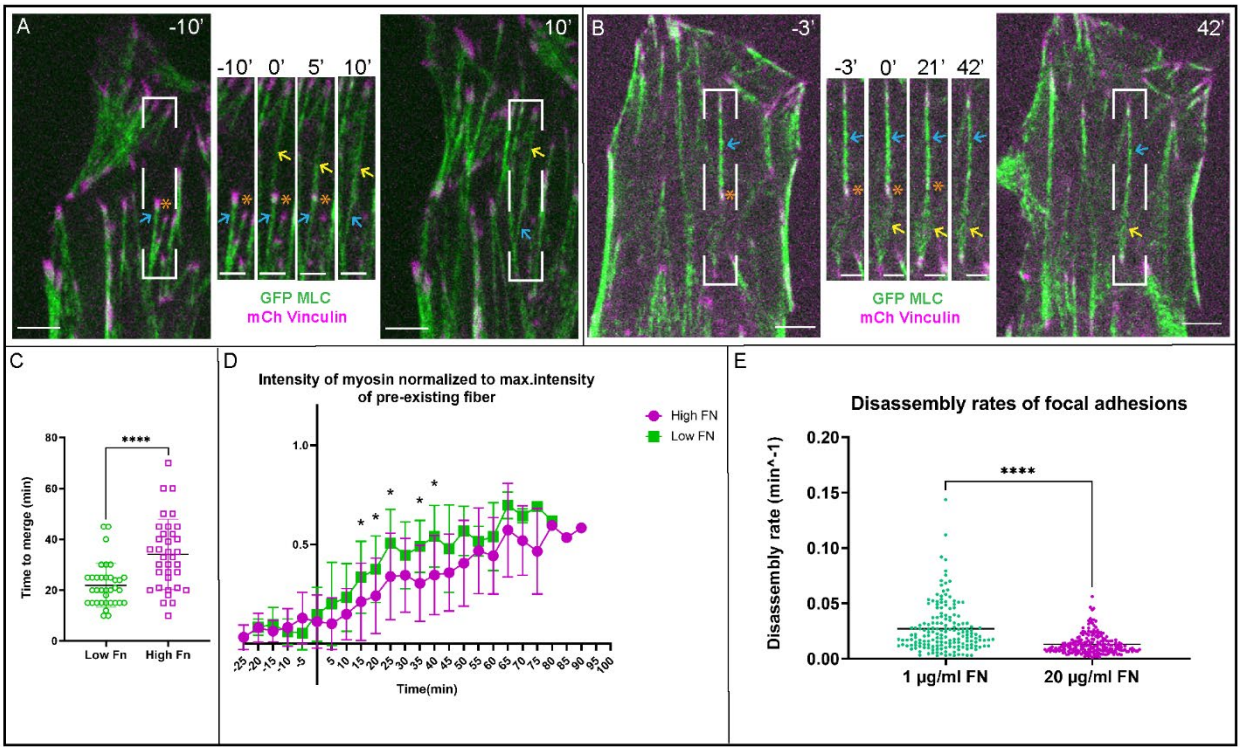

Figure 2.3: Adhesion disassembly is needed for efficient merging

A) Ventral plane timelapse of MRC5 cell plated on 1 µg/ml Fibronectin substrate expressing GFP-Myosin Light Chain (MLC, green) and mCherry Vinculin (magenta) showing a merging event. Boxes on cell images at -10 min and 10 min note position of the merge event in the insets. Insets show merge event where a newly formed secondary fiber (yellow arrow) is attached to the primary fiber (blue arrow) at the intervening adhesion (asterisk). As the intervening adhesion dissolves, the merging fibers are joined into a single merged ventral fiber by 10 min. Scale bar= 10 µm (all). B) Ventral plane timelapse of MRC5 cell plated on 20 µg/ml Fibronectin substrate expressing GFP-Myosin Light Chain (MLC, green) and mCherry Vinculin (magenta) showing a merging event. Orange boxes on cell images at -3 min and 42 min note position of the merge event in the insets. Insets show merge event where a newly formed secondary fiber (yellow arrow) is attached to the primary fiber (blue arrow) at the intervening adhesion (asterisk). As the intervening adhesion dissolves, the merging fibers are joined into a single merged ventral fiber by 42 min. Scale bar= 10 µm (all). C) Time taken to merge (including both adhesion disassembly and continuous myosin fiber formation) for 35 events each in low and high

*Fibronectin conditions. Merge events on high Fibronectin substrate are significantly slower. (Mean for Low Fn= 21.97 min, Mean for High Fn= 34.06 min, Mann-Whitney test, P < 0.0001, exact, two tailed, Mean and SD on graph) D) Averaged graphs of myosin intensity parameters for 17 events each in low and high Fn conditions. Myosin datapoints represent the min/max intensity ratio as described in methods. Data points represent the mean and error bars represent SD. * P ≤ 0.05, T-test for normal distributions and Mann-Whitney test for non-normal distributions, two-tailed P value for either test. E) Graph of focal adhesion disassembly rates for cells plated in low (1 μg/ml) vs high (20 μg/ml) Fn substrate. N=172 adhesions (low Fn, mean = 0.02694 min-1) and 206 adhesions (high Fn, mean= 0.01299 min-1). Line on graph represents the mean. Mann Whitney test, two tailed, P<0.0001 (approx).*

2.3.4 PARALLEL ANGLE OF CONTACT AT THE MERGE POINT FACILITATES SUCCESSFUL MERGING

To explore how mechanistic feedback could influence dynamics and success of merging events, we constructed a computational model of the force interactions between the primary and secondary fibers along with the intervening adhesion (**Fig 2.4A,B**). Fibers are modeled as simple contractile elements, while the intervening focal adhesion is modeled as a catch bond (Kong et al, 2009) whose substrate dis-association rate decreases with increasing applied force (i.e. force prolongs bond lifetime). The purpose of this modeling is to assess how the force interactions between two interacting fibers affect the dynamics of the intervening adhesion.

The main prediction of our model is that when merging fibers are positioned in a straight line, the tensile forces cancel each other, depriving the adhesion of the forces needed to stabilize it, leading to its disassembly. However, at a sharper interaction angle, the increased net force applied to the adhesion stabilizes the adhesion and at yet sharper angles, the net force exceeds the original force applied by the original fiber (**Fig 2.4A,B**).

This angle of interaction dependence is a consequence of the force interactions between the two fibers and intervening adhesion. Assuming the adhesion is not accelerating, it must be in force balance such that the pulling from the two fibers is balanced by the substrate contact force. When two fibers meet at an angle such that they are nearly parallel to each other, the two contractile fiber forces counterbalance each other, leaving little net force for the substrate force to counterbalance. Due to the force dependent nature of the catch bonds, this lack of substrate force leads to dissolution of the adhesion. However, when the fibers meet at a sharper angle, the two fibers counteract each other less, leading to a larger adhesion force that stabilizes the catch bond. Thus, the angle dependent force applied to the intervening adhesion, combined with the force dependent nature of the catch bond leads to angle dependent stability of the intervening adhesion.

We have then tested this prediction by investigating how the contact angle between primary and secondary fibers in live cells would contribute to the success of merging. We found that successful merges occurred only when the initial angle between merging fibers was close to 180 degrees, such that the merging fibers are almost aligned in a straight line at the moment of initial connection (**Fig 2.4B,C,D**). In contrast, fibers that connected at an adhesion in sharper angles frequently failed to merge. We have categorized failed merges based on the stability of the secondary fiber attachment to the intervening adhesion. In category 1, the secondary fiber emerges and attaches to an adhesion but exists only for a short period and dissolves before the adhesion has a chance to undergo disassembly (**Fig 2.4B,C,E**). For sharper contact angles, which according to our computational model do not allow for rapid remodeling, we suggest that the attachment of secondary fibers to an existing adhesion cannot be stabilized. Instability of attachment could be explained by the alignment of actin filaments above the adhesion (Martins et al, 2021), which prevents efficient myosin incorporation. Rapid adhesion disassembly and restructuring of actin into an opposite polarity array would be needed to form a continuous contractile VSF structure, as observed in successful merges at angles close to 180 degrees (**Fig 2.4B,C,D**).

In category 2, the secondary fiber attaches for an extended time, indicating that a stable connection with the adhesion has formed. In such a scenario, the failed merge is followed by either dissolution of the primary fiber (**Fig 2.4F**) or the long-term persistence of both fibers in a V-shaped arrangement (**Fig 2.4G**). In both cases of category 2, the angle between the two fibers is sharp, and the intervening adhesion does not dissolve in the course of observation. We speculate that in this scenario, connection of the secondary fiber to the inner side of intervening adhesion allows for rapid stabilization of attachment due to the pre-existing proper actin polarity. The merge, however, cannot be completed because the mechanosensitive feedback prevents adhesion turnover. Moreover, when a V shaped structure is formed, the adhesion often grows due to the increased pulling forces from the primary and secondary fibers, consistent with the views in the field. Overall, our analysis shows that mutual positioning of the merging fibers dictate the balance of contractile forces at the adhesion, and, consequently, the success of the VSF merging process.

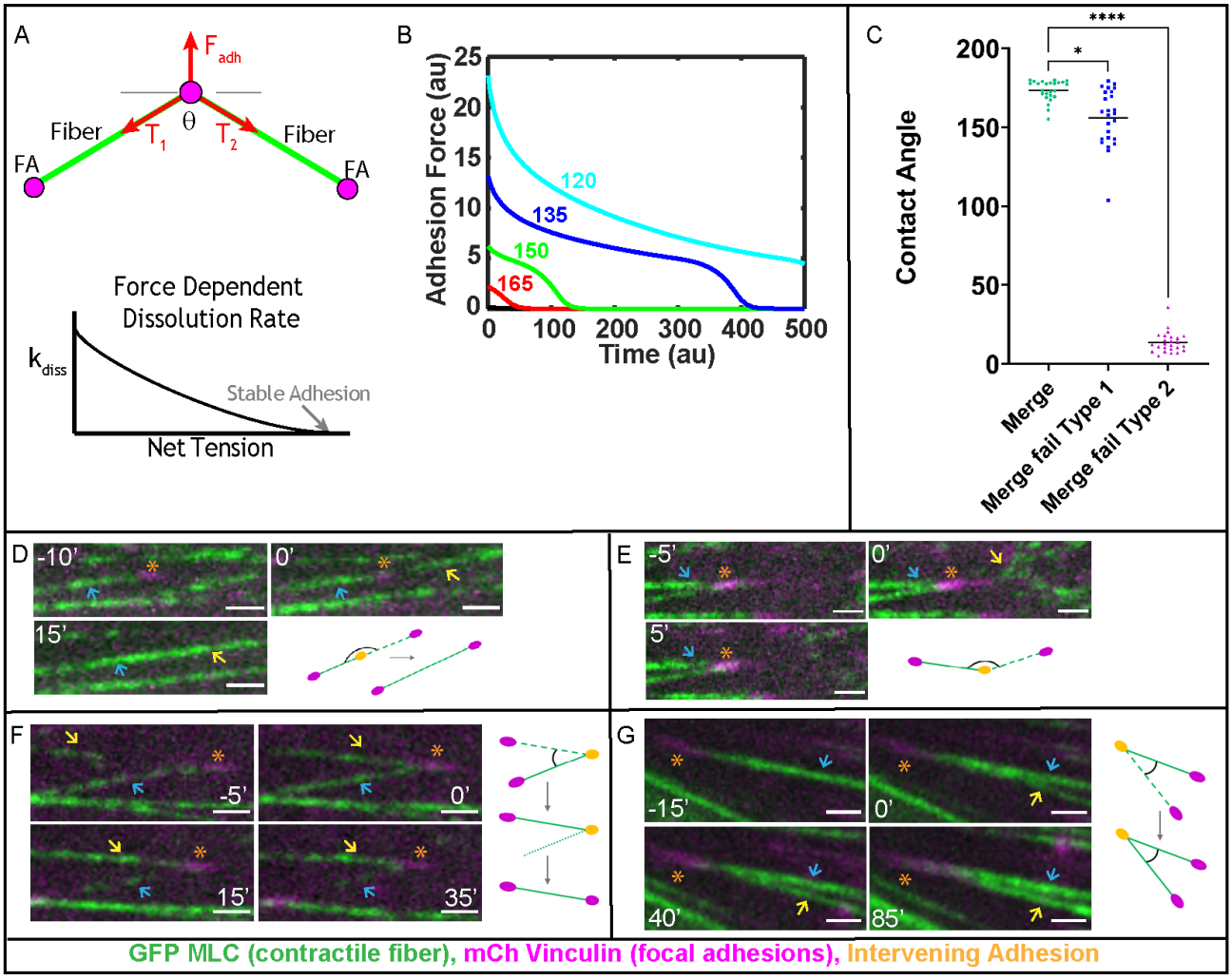

Figure 2.4: Parallel angle of contact at the merge point facilitates successful merging

A) Top) Schematic illustration of the forces applied to an intervening adhesion between two associated stress fibers. Bottom) Schematic illustration of the force dependent stability of adhesions. The net tension of the contractile stress fibers is balanced by the adhesion-substrate force. We assume that above a certain applied force, the adhesion is stable and below this critical force the adhesion dissolves with a force dependent rate; lower forces applied to the adhesion yield more rapid dissolution. B) Computational simulation results showing the adhesion force as a function of the angle at which two fibers associate (θ =165,150,135,120 degrees). The slow phase of adhesion force drop results from contractile stresses straightening the joint fiber while the abrupt drop in force results from the adhesion dissolving. Sharper association angles yield longer adhesion

*lifetimes. See Modeling Methods for further details. C) Graph of contact angles between the primary and secondary fiber in successful merges (Merge, mean=173.5 degrees), unsuccessful merges where the secondary fiber doesn't connect fully (Merge fail Type 1, mean=156.1 degrees) and unsuccessful merges where the secondary fiber connects but a merging does not occur (Merge fail Type 2, mean=13.71 degrees). (n=75 total (25 each condition), Kruskal-Wallis test (two tailed), Dunn's multiple comparisons, * P ≤ 0.05, **** P ≤ 0.0001, line represents the mean). D-G) Ventral plane timelapse of MRC5 cell plated on 20 µg/ml Fibronectin substrate expressing GFP-Myosin Light Chain (MLC, green) and mCherry Vinculin (magenta) showing a D) successful merging event E) unsuccessful merging event where secondary fiber doesn't properly connect to the intervening adhesion F) unsuccessful merging event where secondary fiber connects, but the merge doesn't occur due to primary fiber disassembly G) unsuccessful merging event where secondary fiber connects and merge doesn't occur but V shaped structure formed remains for several minutes. In all panels, the secondary fiber is marked by a yellow arrow, the primary fiber is marked by a blue arrow and the intervening adhesion is marked by an orange asterisk. Scale bar= 10 µm.*

2.3.5 MERGED FIBERS ARE ALIGNED TO THE MAJOR AXIS OF THE CELL

While our data indicate that VSF merging is a significant part of actin network remodeling in motile fibroblasts, we have also addressed how this process affects overall VSF network organization. In motile cells, the main contractile force must be aligned with the direction of migration, which is, in a directionally moving fibroblast, the direction of the long cell axis. Accordingly, stress fiber alignment with the long axis defines efficiency of cell translocation.

To analyze the impact of merging to the subpopulation of aligned stress fibers, we calculated the angles of merged fibers with respect to the long axis of the cell. **Fig 2.5A and B** shows that VSFs formed by merging are aligned within 25 degrees of the major axis of the cell. Computational modeling further shows that merging contributes to

global alignment of VSFs by reducing the variance of VSF orientation in the cell (**Fig 2.5C, D**). To demonstrate this, we created a computational model of the interactions between a population of stress fibers and simulated the length and angle distribution of the resulting network when they are and are not allowed to merge. When merger is present, the resulting VSF network is better aligned with the cell axis (**Fig 2.5D**) and longer (5-10 μm) fibers (**Fig 2.5C**) are observed. Thus, merging of VSFs both promotes the formation of longer fibers, and helps ensure those fibers are better aligned with the direction of migration. Both factors are necessary to facilitate the efficient transmission of force into directed migration.

Stress fibers have been established as instrumental for cellular force production (Kassianidou & Kumar, 2015), and VSFs in particular are the major traction force producers in the cell (Soiné et al, 2015). Our results indicate that out of smaller stress fibers, those which are aligned similarly to each other and to the long cell axis merge more efficiently (**Figs. 2.4 and 2.5**). We speculate that this would enhance the VSF subpopulation coaligned with the direction of cell migration. At the same time, VSFs oriented at a bigger angle to the direction of migration cannot merge and remain small, thus only slightly contributing to the force balance in a cell. Thus, the uniform alignment of VSFs via merging contributes to directional, contractile force production by the cell, which underpins cellular functions such as cell polarization and rear-retraction during migration (Vallenius, 2013; Kassianidou & Kumar, 2015; Lee et al, 2018).

To conclude, in this paper, we have characterized the novel phenomenon of merging as a process for VSF formation, through experimental and computational methods. Merging occurs in the ventral plane of the cell and involves both actomyosin fiber crosslinking and focal adhesion dynamics to form a new VSF. The success of merging is dictated by the balance of contractile forces at the point of merging. In a subsequent functional feedback, merging itself directs the force landscape of the cell by modulating uniform alignment of ventral stress fibers.

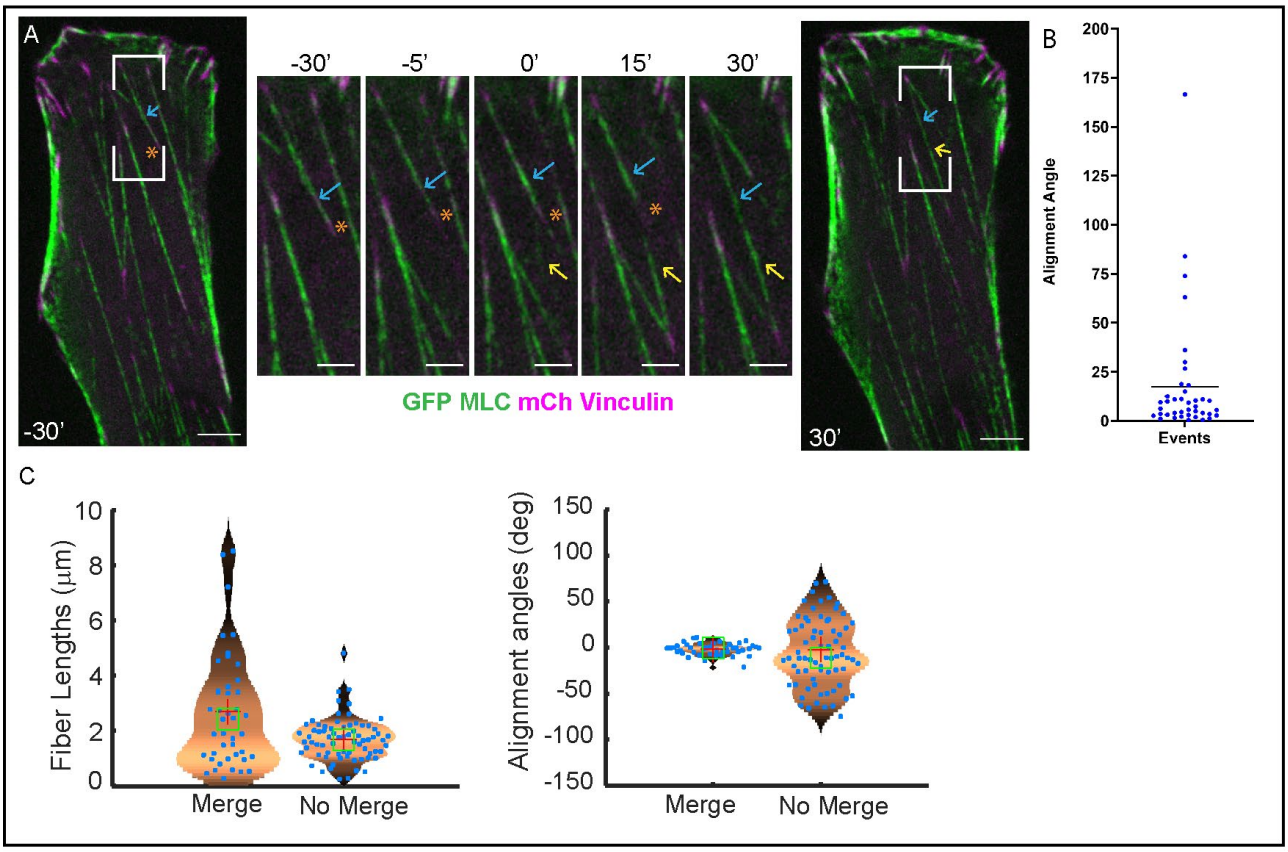

Figure 2.5: Merged fibers are aligned to the major axis of the cell.

A) Ventral plane timelapse of MRC5 cell plated on 20 µg/ml Fibronectin substrate expressing GFP-Myosin Light Chain (MLC, green) and mCherry Vinculin (magenta) showing a merging event. Boxes on cell images at -30 min and 30 min note position of the merge event in the insets. Insets show merge event where a newly formed secondary fiber (yellow arrow) is attached to the primary fiber (blue arrow) at the intervening adhesion (asterisk). As the intervening adhesion dissolves, the angled merging fibers are joined into a single, straight merged ventral fiber that is aligned to the major axis of the cell. Scale bar= 10 µm (all). B) Graph of alignment angle of the merged fiber with the major axis of the cell (angle data points are the difference in angle between the merged fiber and the major axis) (n=40, mean=17.37 degrees, line represents the mean) C) Outcome of computational simulations showing the distribution of fiber lengths and alignment angles in simulations where stress fiber merger is either present or not present.

Results demonstrate that when merger is present, longer fibers result and the distribution of fiber angles is less variable.

2.4 FUNDING AND AUTHOR CONTRIBUTION

This work was supported by National Institutes of Health (NIH) grants (R01-DK106228 (to IK and WRH), R01-GM052932 (to WRH) and R35-GM127098 (to IK)) and American Heart Association (AHA) predoctoral fellowship 18PRE33990479 to SN. We thank Hamida Ahmed for technical help.

SN performed the cellular experiments, analyzed the data and wrote the manuscript. WRH performed computational modeling and wrote the manuscript. IK designed experimental and analytical strategy and wrote the manuscript. All authors provided intellectual input, edited and approved the manuscript.

2.5 MATERIALS AND METHODS

Cell culture:

MRC5 cells (*human lung fibroblasts, ATCC® Cat# CCL-171TM, RRID:CVCL 0440*) were maintained in MEM media (*Cat# 11095080, Thermo Fisher Scientific*) supplemented with 10% fetal bovine serum, 100 µM penicillin and 0.1 mg/ml streptomycin in 5% CO2 at 37°C. In live-cell microscopy, the cells were maintained on the microscope stage in 5% CO2 at 37°C. Cells were seeded on glass bottom dishes (*Cat# P35G-1.5-14-C, MatTek*) that were coated with fibronectin (*Cat# FC010, EMD Millipore*) 48-72 hours before experiments. Dishes were plasma cleaned before coating with 1 or 20 µg/ml fibronectin and used without plasma cleaning for coating with 10 µg/ml fibronectin.

Expression constructs:

pEGFP-gamma-Myosin Light Chain (Courtesy of Dr. Rex Chisholm, Northwestern University) was used to visualize contractile actin fibers in the cell. mCherry-Vinculin (Courtesy of Dr. Michael Davidson, Florida State University) was used to visualize focal adhesions. GFP-UtrCH (Courtesy of Dr. William Bement, University of Wisconsin-Madison) was used to visualize actin fibers and actin plaques at adhesions. Cells were transfected by the AMAXA NucleofectorTM 2b device (Cat# AAB-1001, Lonza, Program A-024) according to manufacturer's instructions.

Microscopy:

Live-cell confocal spinning disk microscopy was used to visualize VSF dynamics. We used a CSU-X1 (Yokogawa Spinning Disk Field Scanning Confocal System) coupled with the Nikon Eclipse Ti-E inverted microscope. Images were acquired with an Apo TIRF 100× oil lens (NA 1.49) and Andor DU-897 X-11240 cameras. 3D confocal image stacks (step size: 200 nm) were captured every 1.5, 3 or 5 min, over a period of several hours. We visualized GFP-constructs with the 488 laser line, and mCherry Constructs with the 568 laser line.

Image preparation for figures:

Representative images and videos were prepared using Fiji (Ver 2.0.0 rc69-1) (Schindelin et al, 2012). Maximum Intensity Projection of the ventral planes of the cell (400-600 nm total thickness) were used in representative figures and supplemental videos. In figures and videos, brightness and contrast were adjusted for each channel to make structures clearly visible (no gamma adjustments). StackReg plugin (Thevenaz et al, 1998) in Fiji was used to align image slices through time. Representative images and videos were resized in scale though bicubic interpolation and rotated to show the relevant event.

Data analysis:

We analyzed the merging events in the cell by manually tracking the dynamics in Fiji. The point of visually observing a secondary fiber attached to the

intervening adhesion and primary fiber was assigned time “0 min”. To estimate the time taken to merge (***Fig 2.3C***), we manually tracked the time from 0 min to the frame where both a seamless myosin bridge was present and adhesion signal was not present. 35 events each were tracked in the low (1ug/ml fibronectin substrate) and high (20ug/ml fibronectin substrate) datasets. To further quantitatively analyze the formation of the myosin bridge at the merge point over time (***Fig 2.3D***), we drew linescans (line width: 3 pixels) using the segmented line tool in Fiji for each time frame of a merging event. We then subtracted the background intensity and averaged the values over approx. 1 micron.

To assess myosin bridge formation, we needed a parameter indicating when the myosin intensity in the merging region becomes similar to the myosin intensity of the stress fiber. We used the ratio of minimum value/maximum value of myosin in each linescan. As the bridge formed, the ratio increased closer to 1 because of myosin incorporation forming a cohesive line between the merging fibers. If there were negative values for myosin intensity (due to signal fluctuation and background subtraction), we assigned that value to “0” (subtracted the lowest negative value in the event from each intensity value). This ensured that all min/max ratios were positive. The curves were aligned by assigning the time point of maximum intensity of vinculin in each event as ‘0 min’ and 17 events each in low and high FN condition were averaged to form a curve in Graphpad Prism (Ver 9.0.0 for Windows, GraphPad Software, San Diego, California USA, www.graphpad.com). We tested for normality of distribution using the Shapiro-Wilk test, Student’s t-test was performed for the normally distributed values, Mann-Whitney test was performed for non-normally distributed values at each time point to assess the significance.

We used the Focal Adhesion Analysis Server (Berginski & Gomez, 2013) to calculate the disassembly constants of adhesions in the low and high fibronectin substrate conditions. A semilog plot of fluorescent intensity of vinculin as a function of time was plotted by the software based on the protocol in Webb et al (Webb et al, 2004). The slope of this graph determines the apparent rate constant of adhesion dissociation. The input files were thesholded in the software according to recommended input protocol, the

threshold level was chosen for each movie based on best judgement of the investigator to compensate for variable adhesion marker expression.

To calculate the angle at the merge point, we marked the angles manually at 0 min by the angle tool in Fiji. 25 events per condition were marked from the high Fn dataset for ***Fig 2.4C***. Kruskal-Wallis test with Dunn's multiple comparisons was performed to assess the significance.

To calculate the alignment of merged fibers in the cell, we fit an ellipse to the cell at the time frame of conclusion of the merge and measured the angle of the long axis. We calculated the alignment angle of the fiber as the difference between the angle of the merged fiber and the long axis angle, for 40 events in ***Fig 2.5B***.

Modeling methods:

We modeled ventral stress fibers (VSFs) as contractile elements with focal adhesions (FAs) on both ends. Both VSFs and FAs possess complex internal structure and dynamics. Modeling the full scope of these dynamics is beyond the scope of this investigation. Our main purpose here is to assess 1) how merger dynamics would influence the broader network of VSFs and 2) how the dynamics of an intervening adhesion influence the merger of primary and secondary fibers. Towards this end, we model VSFs as simple elastic elements and FAs as catch bonds (Kong et al, 2009).

Each VSF is modeled as a collection of discrete nodes $\{x_i\}$ connected by contractile segments represented as simple Hookian springs which can compress or stretch depending on the applied forces. The first ($i=1$) and last ($i=N$) nodes represented the adhesions, and the remaining internal nodes represent a computational discretization of the VSF.

The internal nodes of the VSF obey the Langevin equation $\gamma_c\left(dx^i/dt - v_c\right) = F_{spring}^{i-1} + F_{spring}^{i+1}$. Here the term on the left is a standard drag term where the drag of the internal node is dependent on the velocity of that node relative to the speed of the cytosolic flow, which we include since the cytosol flows with the body of a moving cell

while VSFs are anchored to the substrate and do not, creating a relative flow. The two spring forces account for the contractile nature of the segment connecting nodes i → i-1 and i → i+1 and take the form $F_{spring} = k\left[\left(x^i - x^{i+1}\right) - \Delta x_{rest}\right]$. Here the rest length of each segment of a particular VSF is taken to be the same (i.e. a uniform discretization). The rest lengths of all segments are initialized at 0.5 μm and all fibers are initialized as strait entities such that fiber length = segment # * 0.5.

The FA nodes obey modified dynamics since they are subject to forces from the substrate as well. Force interactions between FAs and the substrate can be complex due to the catch / slip dynamics of FAs in different force regimes. Our main goal here is to simply encode the fact that FAs resist motion relative to the substrate, which we model as a drag relative to the substrate with a high drag coefficient. The i = 1 (and similar for I = N) FA node obeys the Langevin equation $\gamma_c(dx^1/dt - v_c) + \gamma_E dx^1/dt = F^2_{spring}$. The first term is again drag imposed by the potentially flowing cytosol, the second term is drag imposed by the substrate adhesion, and the final term is the single spring force between the i=1 and i=2 nodes.

The parameters of this model do not significantly impact its dynamics. We non-dimensionalize the system such that the cytosolic drag coefficient is $\gamma_c = 1$. It may be possible to calculate the drag on a rod immersed in the cytosolic fluid. However, the precise value mainly determines the timescale over which drag forces operate in this simple model, and not the qualitative results, which are our main focus. The spring forces ensure fibers relax to a strait geometry with a determined length and the spring constant only affects the timescale of the relaxation. As such we make the choice $k/\gamma_c = 1$. In simulations not shown, we have taken k=0.1, 10, 100. While this spring constant can affect numerical stability (stiffer spring constant requires smaller simulation time step), this choice does not affect the qualitative outcomes presented in this article. The cytosolic flow (a consequence of cell movement) is taken to be $v_c = 0.007$ μm / s, consistent with observations of fibroblast motility speed (Qin et al, 2015). For all simulations, the computational time step is taken to be $\Delta t = 0.5$ with a final simulation time of $T = 5000$.

In **Figure 2.4**, we model the interaction between two VSFs with these dynamics. In this specific model, one of the internal nodes represents the intervening adhesion and obeys the appropriate dynamics (cytosolic drag, substrate drag, and two spring forces). The goal of this specific model is to determine how the angle of contact influences adhesion stability. Since it is well established that, in appropriate regimes, applied forces strengthen and prevent dissolution of FAs, we consider assume that the friction coefficient $\mu_E(t)$ is time dependent and depends on the force applied to the adhesion.

This time / force dependence is modeled as $d\gamma_E/dt = -k_{diss}\gamma_E$. The rate of dissolution is force dependent and for simplicity is modeled as a linear function where increased force yields a lower rate of dissolution: $k_{diss} = 0, F > F_{max}$, and $k_{diss}/k_{max} + F/F_{max} = 1, 0 < F < F_{max}$. The k_{max} parameter controls the maximum speed of dissolution and for simplicity we set $k_{max} = 1$. We calibrate F_{max} so that the terminal node adhesions are stable and set $F_{max} = 5$. This choice does affect results somewhat. Specifically, it affects the contact angle at which adhesions become unstable. Wider ranges of contact angles become stable for smaller values of this parameter. The essential explanation for this is that this parameter defines the window of forces $[0, F_{max}]$ where the adhesion is insufficiently loaded to be stable, and more acute interaction angles produce larger loadings.

For **Figure 2.5**, we model the interaction between fifty initial fibers (with initial length 2.5 μm) to assess how the merger dynamics influence the length and angular distribution of resulting fibers. To create the initial condition for all simulations, we randomly insert fifty fibers allow those to merge where overlaps occur such that the new fibers are non-overlapping. We then simulate two model conditions: one where fibers that come in close proximity merge, and another where merge is not allowed. For simplicity in the merge simulations, we assume that when two fibers come into contact, they successfully merge. It is possible to incorporate rules for conditional success of VSF merger. Here however our purpose is mainly to assess how the presence of merger

influences the resulting distribution of VSFs, not to model the effects of more detailed observations about mergers.

CHAPTER 3:

A FOCAL ADHESION FILAMENT CROSS-CORRELATION KIT FOR FAST, AUTOMATED SEGMENTATION AND CORRELATION OF FOCAL ADHESIONS AND ACTIN STRESS FIBERS IN CELLS.

This chapter is published in PloS ONE under the same title

Hauke, L.*, Narasimhan, S.*, Primeßnig, A., Kaverina, I., & Rehfeldt, F. (2021). A Focal Adhesion Filament Cross-correlation Kit for fast, automated segmentation and correlation of focal adhesions and actin stress fibers in cells. PloS one, 16(9), e0250749.
(* denotes co-first authors)

3.1 ABSTRACT

Focal adhesions (FAs) and associated actin stress fibers (SFs) form a complex mechanical system that mediates bidirectional interactions between cells and their environment. This linked network is essential for mechanosensing, force production and force transduction, thus directly governing cellular processes like polarization, migration and extracellular matrix remodeling. We introduce a tool for fast and robust coupled analysis of both FAs and SFs named the Focal Adhesion Filament Cross-correlation Kit (FAFCK). Our software can detect and record location, axes lengths, area, orientation, and aspect ratio of focal adhesion structures as well as the location, length, width and orientation of actin stress fibers. This enables users to automate analysis of the correlation of FAs and SFs and study the stress fiber system in a higher degree, pivotal to accurately evaluate transmission of mechanocellular forces between a cell and its surroundings. The FAFCK is particularly suited for unbiased and systematic quantitative analysis of FAs and SFs necessary for novel approaches of traction force microscopy that uses the additional data from the cellular side to calculate the stress distribution in the substrate. For validation and comparison with other tools, we provide datasets of cells of varying quality that are labelled by a human expert. Datasets and FAFCK are freely available as open source under the GNU General Public License.

3.2 INTRODUCTION

The shape and mechanics of biological cells depends largely on the cytoskeleton, a dynamic network that functions as the cellular cytoskeleton and produces contractile forces acting on their environment, such as the extracellular matrix (ECM) or neighboring cells. A predominant and essential part of this network is made up of actin filaments that act as structural elements and, importantly, are capable of producing contractile forces when co-assembled with myosin II mini-filaments into contractile stress fibers (Pellegrin & Mellor, 2007).

Geometry and rearrangement of stress fibers is a critical factor during mechanical interactions between the cell and the ECM in many processes (e.g. adhesion, migration, etc.) and must be quantitatively assessed to elucidate the complex mechanical interplay of cells with their surroundings. Interestingly, the pattern of stress fiber formation in human mesenchymal stem cells reveals an optimal matrix elasticity E yielding an anisotropic and polarized acto-myosin fiber structure, which functions as an early morphological marker of mechano-guided differentiation (Zemel et al, 2010; Zemel et al, 2010). This requires a quantitative analysis of the filament structure (e.g. by a simplified order parameter S known from liquid crystal theory as introduced earlier (Zemel et al, 2010), that builds on the unbiased and automated segmentation of stress fibers. Various approaches exist to address this task, among which our recently developed FilamentSensor analysis tool allows for automated detection and quantification of stress fiber structures (Eltzner et al, 2015). However, for a complete functional analysis of cell and matrix mechanics, quantification of both stress fibers and their associated focal adhesions is needed.

Cells adhere to the ECM or surrounding cells via cell-matrix and cell-cell contacts, respectively. These structures function as biochemical anchors and are key to the signaling and mechanical interactions of cells with their surroundings. Focal Adhesions (FAs) are cell-matrix anchors based on trans-membrane proteins integrins, with a multitude of associated proteins on the cytosolic side. Serving as the interface between the SFs and the ECM, FAs have several functions, such as providing cellular

attachment to the substrate, transducing contractile forces to the ECM and facilitating bi-directional transmembrane signaling (Parsons et al, 2010). At the cytosolic side, FAs are structurally and dynamically linked to the ends of SFs (see **Fig 3.1A–C**). The formation and maturation of FAs is dependent on actomyosin-generated tensile forces applied on them through associated SFs (Parsons et al, 2010). In turn, signaling pathways that are mechanically triggered at adhesions lead to actin polymerization and elongation of the fibers at their FA-associated termini (Ciobanasu et al, 2012). Thus, there is an intricate, dynamic association between FAs and SFs that needs to be quantified to fully elucidate their cellular functionality.

Cellular SFs are broadly classified as transverse arcs, dorsal SFs and ventral SFs based on their FA association, which underlies their varied roles (**Fig 3.1D**) (Pellegrin & Mellor, 2007). Actin transverse arcs, which are not associated with FA but rather embedded into the cortical actin meshwork at their termini, are contractile structures that contribute to cell shape but not do not directly exert force onto the environment. Dorsal SFs are associated with FAs at one end and with transverse arcs on the other end. Although they are non-contractile due to their negligible myosin II content, they can exert forces on their terminal adhesion through their association with transverse arcs. Ventral SFs, which are connected to FAs at both ends, are contractile structures that generate majority of cellular traction forces on the substrate (Soiné et al, 2015; Vallenius, 2013). Due to this natural linkage of SFs and FAs, cytoskeletal studies often result in cells with an observed actin SF phenotype having an associated FA phenotype (Guo et al, 2006; Kanellos et al, 2015; Bach et al, 2009; Feng et al, 2013; Kovac et al, 2013). Therefore, incorporating detection of SF-FA coupling in studies would greatly facilitate the complete analysis of their structure and function in cells.

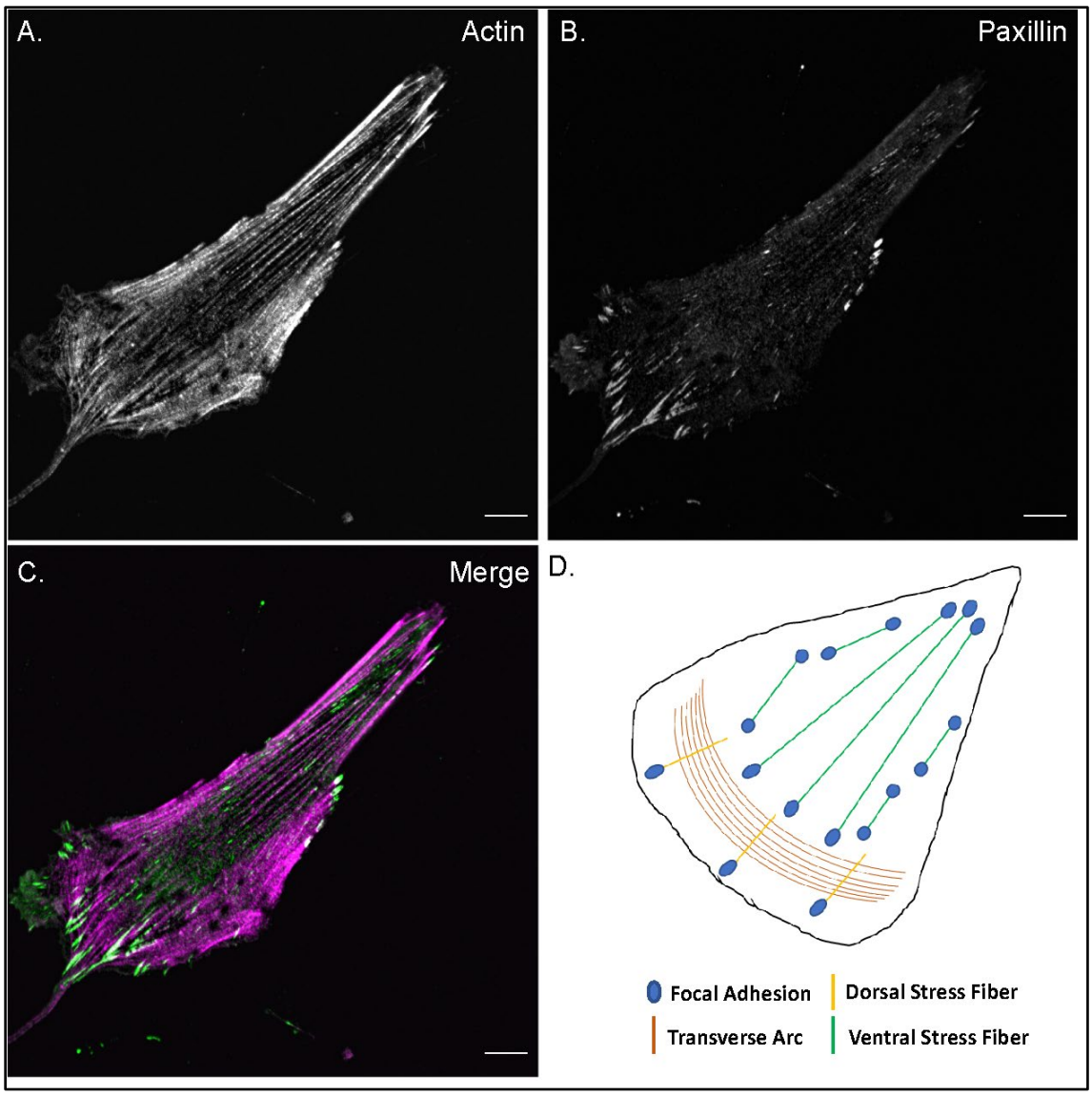

Fig 3.1. Stress fibers and focal adhesions.

Confocal fluorescence microscopy images of an MRC5 cell stained for A) actin filaments (phalloidin) and B) focal adhesions (paxillin). C) Merged color image of the cell with actin filaments in magenta and adhesions in green. All images are of the ventral plane of the cell, scale bar—10 μm. D) Schematic illustration of different stress fiber subtypes and their association with focal adhesions.

Manual evaluation and analysis of FAs and SFs is a laborious, time-intensive process and is always at risk due to the observer's bias. Recently, this process has been aided by several automated analysis tools and algorithms that are optimized either for focal adhesion analysis (such as the Focal Adhesion Analysis Server (Berginski & Gomez, 2013), PAASTA (Broussard et al, 2015), or Buskermolen's segmentation algorithm (Buskermolen et al, 2018), or stress fiber analysis (such as previous version of FilamentSensor (Eltzner et al, 2015), CytoSeg (Nowak et al, 2020) and SFEX (Zhang et al, 2017) and MatLab scripts like Rogge's FSegment (Rogge et al, 2017)).

However, a tool for speedy, unbiased quantification of SFs, FAs, and their mutual coupling is yet missing. Here, we present an integrated FA-SF analysis module called the Focal Adhesion Filament Cross-correlation Kit (FAFCK). This tool is based on our previously published FilamentSensor analysis tool, with added capacities for adhesion detection and characterization, filament analysis and coupled FA-SF correlation for stacks or pseudo-stacks of images with similar properties to streamline analysis of huge datasets. FAFCK detects and quantifies FAs and SFs by means of location, area, length, width, aspect ratio and orientation, with capacity for exporting this information enumerated for each frame, allowing for comprehensive further data analysis (e.g. Python, Matlab, etc.) to elucidate cell and matrix mechanics. Our software package will be particularly helpful for sophisticated mechanical measurements and analysis such as model based traction force microscopy (MBTFM) experiments (Soiné et al, 2015) that takes advantage of the a priori determined positions of focal adhesions and stress fibers in addition to the displacement field in the substrate.

3.3 RESULTS

The Focal Adhesion Filament Cross-correlation Kit (FAFCK) is a comprehensive FA-SF analysis software consisting of two modules: the FASensor, for adhesion detection and the FilamentSensor, for actin filament detection, both of which connect through a correlation function for paired characterization of these structures. To correlate an adhesion with the associated actin filament in the cell, the software relates each adhesion object detected by the FASensor module with corresponding filaments that are detected by the FilamentSensor module. As stand-alone programs with a shared GUI, both routines can be used independently as well.

3.3.1 SEGMENTATION OF FOCAL ADHESIONS BY FASENSOR

The FASensor is the adhesion detection module in the software. It is a robust tool for detection of point-like structures partly based on the FilamentSensor (Eltzner et al, 2015). Based on adapted ImageJ routines (**Fig 3.2**), it analyzes the adhesions in an image as objects which can be exported with characteristics and IDs, with multiple customization options to improve accuracy as desired by the user.

Adhesion detection analyzes and segments the input image (usually a grayscale immunofluorescence (IF) micrograph) of focal adhesions. The module is split into Main, Pre-processing and Focal Adhesion output sections. All images are shown in panels on the right- including the original image of adhesions, the pre-processed image, the thresholded image, and the image with overlay of filaments detected from the filament input (Stress Fiber Overlay). The windows can be split from the interface and zoomed in for user ease. The pre-processing tab allows the user to add optional filters to the image in order to improve the signal to noise ratio and normalize the image. Filters included are the Gauss filter, Laplace filter, Line Gauss filter, Cross-correlation filter, and Enhance contrast filter. Filter queues can be saved for reuse.

The main tab has thresholding controls with automated protocols. The levels can also be altered manually to produce the desired binarized image. Additional filters are

provided for defining the minimum or maximum pixel number per adhesion and the maximum amount of clusters allowed in one image. **Fig 3.3** shows an example view of the main window of the software with focal adhesions and stress fibers detected but correlation not yet run. Detailed explanation of the submenus and functions can be found in the tutorial provided with the software.

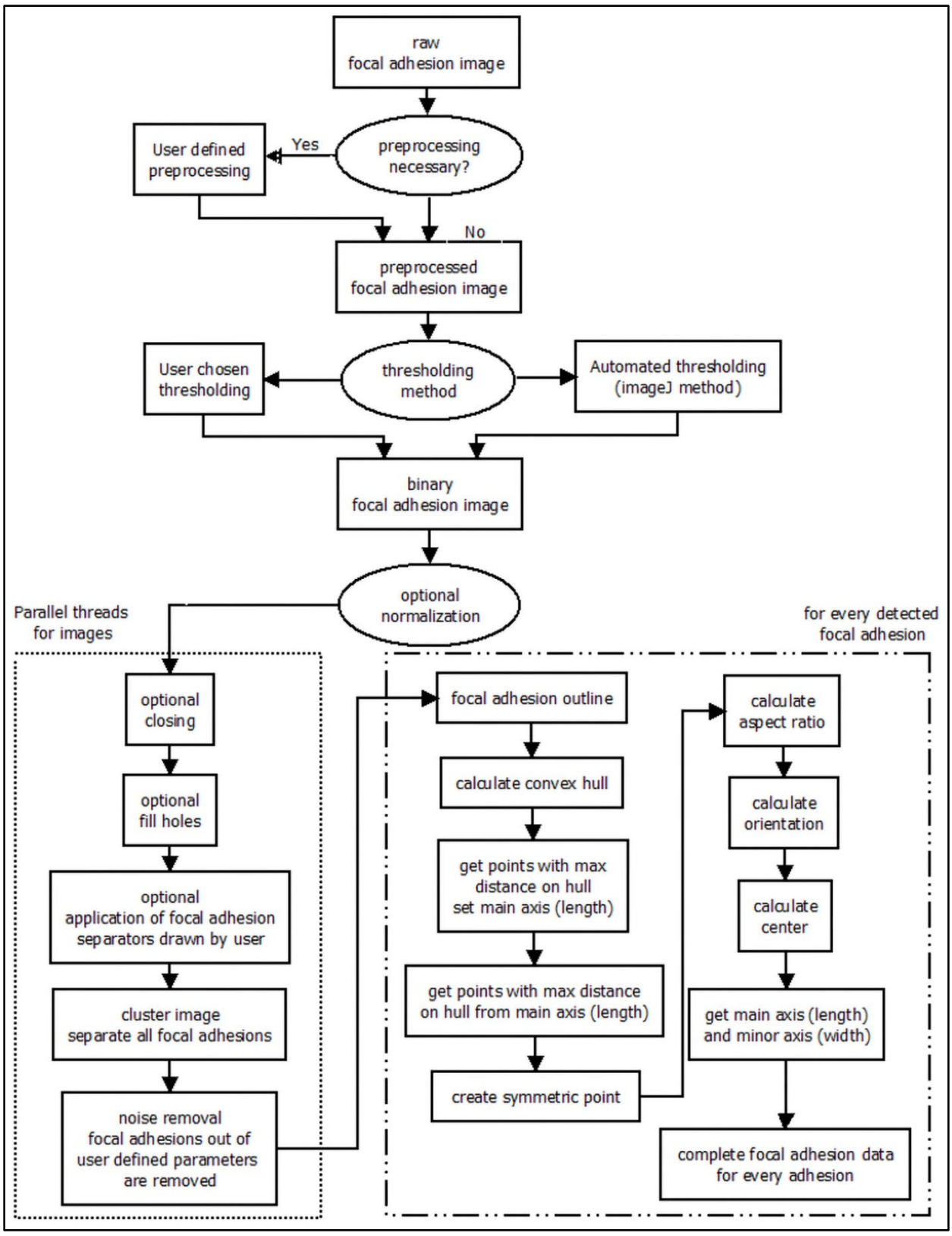

Fig 3.2. Workflow of adhesion detection by FASensor module.

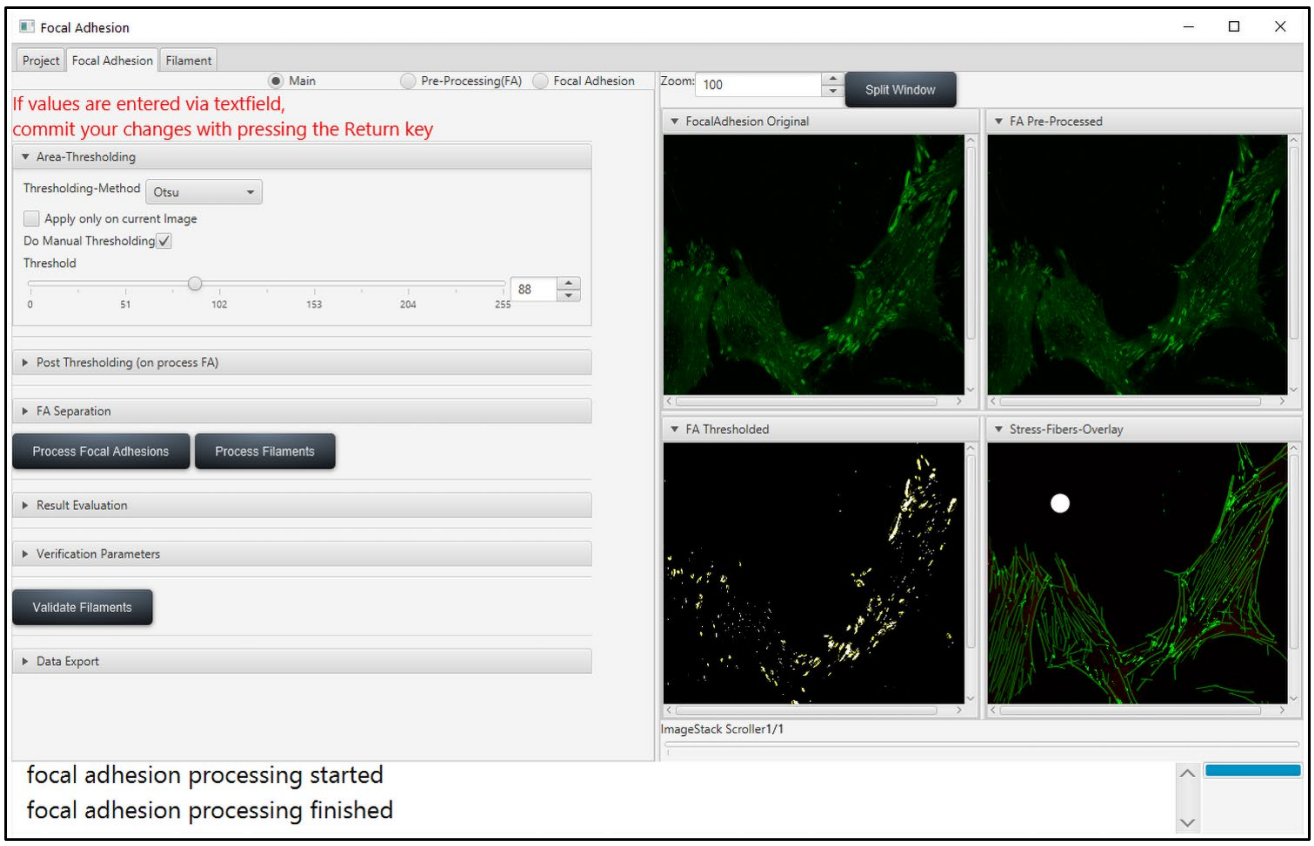

Fig 3.3. Main window of the FAFCK software.

Main window of the GUI consisting of several sub-menus at the left to set threshold, FA size restrictions, validation preferences as well as routine for evaluation against external binary masks and data output options. On the right, processing output is shown and can be customized by the user or detached from the main GUI for a larger view.

On clicking 'Process Focal Adhesions', the adhesion objects are detected. For each adhesion detected, the outline is derived, and a convex hull is calculated. The main axis is set for the points farthest away on the convex hull and for the points farthest away from the main axis, the side axis is set. The aspect ratio, orientation, and center for each focal adhesion is also calculated. The module also allows for further close customization of the detected objects by the user to obtain the most accurate result. In cases where nearby adhesions have been detected as a single one due to poor signal-to-

noise ratio, overlap, artifacts, etc. the user has the option to draw a line on the thresholded image and separate the adhesions at their discretion (see **Fig 3.4A**). Once the lines have been drawn to separate all adhesions as desired, the adhesions can be re-processed to get the split objects in a new map.

The detected FAs are displayed in the table in the Focal Adhesion tab. The ID, XY center position, Length of main axis, Length of side axis, Angle, Area, and Area ellipse of each adhesion are listed in the table. The user can choose to discard a detected adhesion object by selecting the object in the Focal Adhesion original window, on which the boundary turns red, and clicking the remove button under the table. This allows the user to closely edit the adhesion map obtained from the software to remove any inconsistencies based on their expertise. The output focal adhesion map can be exported as a binary mask with outlines and optional numbering with IDs. The output table can be exported as a 'CSV' file and the adhesion detection can be exported as a project 'XML' file.

We illustrate the usage of FASensor with the input image of an MRC5 human fibroblast cell showing adhesions (paxillin) (see **Fig 3.4B**). This input file was preprocessed using Laplace and Gauss filters and thesholded using Intermodes algorithm. With a minimum limit of 10 pixels per adhesion, which corresponds to 0.144 μm^2, adhesion objects were detected by the software (**Fig 3.4C**).

In the post-thresholding section, there is the option to add or opt-out of the closing and filling holes algorithms, by which seemingly disparate objects can be detected as one, especially in cases of large, single adhesion plaques whose signal is not uniform (**Fig 3.4D**). A large, boundary adhesion plaque that is detected as split pieces without the closing and fill holes algorithm can be reprocessed with this algorithm in order to assign it as a single object. After the reprocessing step, the user is able to confirm that the newly joined adhesion matches with expectations.

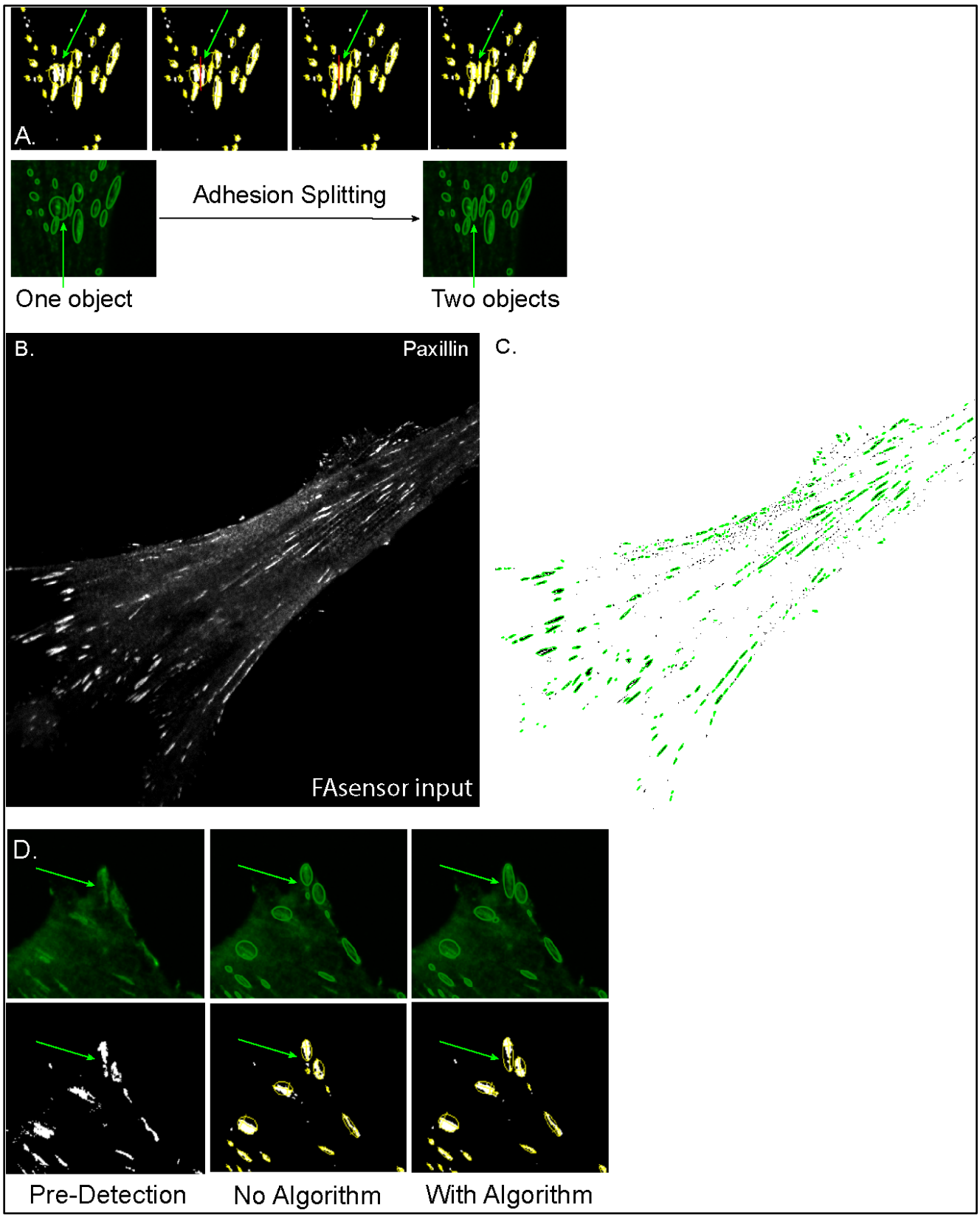

Fig 3.4. Segmentation of FAs by FASensor and subsequent optimization.

A) Montage of adhesion splitting capacity of the FASensor module. (Top) Thresholded image of adhesions (white) have objects detected by module (circled by yellow). Red line is drawn by user to split objects where desired. (Bottom) Before and after images of objects detected in the IF adhesion input, that are split. Green arrow indicates splitting objects in Top and Bottom. B) Input image of focal adhesions (paxillin) in the ventral plane of an MRC5 cell. C) Corresponding segmented adhesion objects (outlined in green) from FASensor. D) Montage showing the closing and filling holes function of the module. (Top series) Objects circled by green detected by FASensor from IF adhesion input. (Bottom series) Objects circled by yellow on thresholded image. (Left) Pre-detection by module (Center) Objects detected when closing and filling holes algorithms are not applied. (Right) Objects detected when closing and filling holes algorithms are applied. Green arrow in the Top and Bottom series indicates the adhesion which is detected as multiple objects without the algorithm and detected as a single object with the algorithm.

3.3.1.1 EVALUATION OF THE FAFCK OUTPUT WITH USER GENERATED OUTPUT

For those using this module to analyze cellular adhesions or stress fibers, it is important to understand how the results compare to their expert opinion and any pre-established routines they already use. To accurately assess the differences between the user's usual routine and the FAFCK output in adhesion detection, our module offers an evaluation option.

In the evaluation panel, a binary adhesion or fiber map generated by the user can be compared with the respective object output generated by FAFCK software (**Fig 3.S1**). Before comparison, additional preprocessing can be applied, for example thickening of outlines. The comparison is done in two ways—an objectwise fashion, where from both the user mask and software output, objects are generated and overlap is checked, and in a pixelwise fashion, where each pixel of user mask and software output is taken into account. The minimal required overlap for object matching between the user mask and output can be manually set by the user. The 'export results' option provides

images of the comparisons and comparison results in a csv file. The results table lists objects that are found in output when compared with the user's mask, objects that are false positives (present only in the software output image, labelled 'eval not matched') and the missed objects that are present only in the user's image (labelled 'truth not matched'). The pixel sizes of all objects are given along with the number of pixels that overlap in the common objects. The output table also gives the cases where the sensor detects multiple objects in output for one object in the mask marked by the expert (multiMatchesOneToN) and cases where the sensor detects one object in the output for multiple objects marked in the mask by the expert (multiMatchesNToOne).

In the example, shown for FAs, the FASensor output is evaluated against the user generated binary adhesion mask (**Fig 3.S1B**) from the IF image using Fiji software (Schindelin et al, 2012). On the landing page of the graphical user interface, the user can also import two binary masks of various origins to execute the evaluation without running the software to get an output first. As with all parts of the software, the evaluation tool can work on OME-TIFF files to provide fast evaluation of large datasets. **Fig 3.S1C** shows the result maps of objectwise and pixelwise evaluation between FASensor output and the user's mask. The evaluation maps assume the user generated mask as true, highlighting the found and missing categories on it and superimposing false positives from software output on the mask as well. The tables **3.S1D and E** show the tabulated results for the different categories in objectwise and pixelwise evaluation respectively.

A.

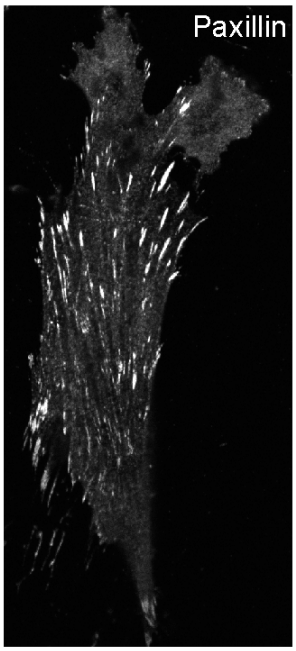

B.

C. Software output evaluation

FASensor output

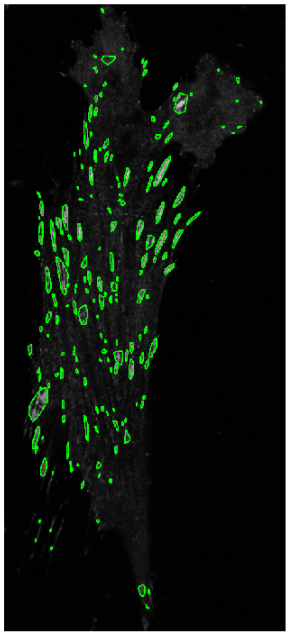

Objectwise Eval

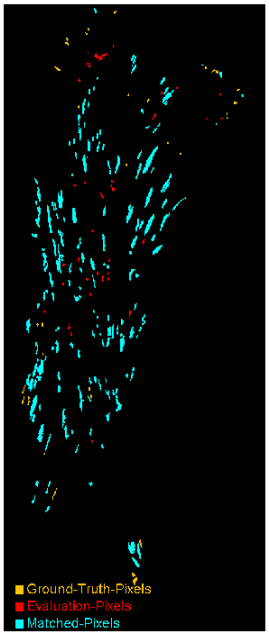

Pixelwise Eval

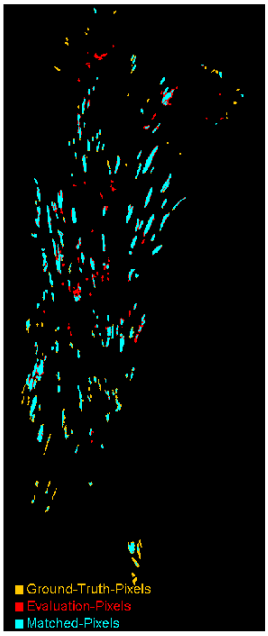

D. Objectwise Eval

Parameter	Values
Objects found	171
Objects missed	34
Objects FP	36
MultimatchesonetoN	2
MultimatchesNtoone	19

E. Pixelwise Eval

Parameter	Values
Matches	9352
Hit rate	0.8052
Miss rate	0.1948
False Positive rate	0.2373
False negative rate	0.0049

Fig 3.S1: Evaluation of adhesions marked by user expert in Fiji vs those detected by the software module.

A) FASensor input of IF adhesion image showing the ventral plane of a MRC5 cell immunostained with paxillin. B) Binary mask of adhesion ROIs marked by user expert C) (Left-Right) Output adhesion objects detected by FASensor from input of A, Objectwise evaluation map of mask vs output, Pixelwise evaluation map of mask vs output. (in all evaluation images, found- blue, missed-yellow, false positive-red). D) Objectwise evaluation results tabulated. E) Pixelwise evaluation results tabulated.

The input routine, in terms of filters and thresholding method used, affects similarity of the FASensor output to user drawn mask. **Fig 3.S2** shows how objects detected by FASensor are more similar to the user mask when an appropriate input routine is used instead of default settings. From input of **Fig 3.S2A** , FASensor output is derived in two ways: unoptimized (filter settings and thresholding that is default coded in the software and not necessarily appropriate for the cell) and optimized (appropriate filter settings and thresholding adjusted by the user). These settings can consist of filters applied to the whole image, manually set thresholding algorithm parameters, applying or not applying the closing and fill holes options, setting boundary conditions for focal adhesion size, and finally separating focal adhesions via user input. Objectwise evaluation of the outputs with user mask (**Fig 3.S2B**) is shown in **Fig 3.S2C** for unoptimized output and **Fig 3.S2D** for optimized output, where found and missing categories as compared to output on the left are highlighted on the user mask and false positives from output are superimposed on the mask as well. In the unoptimized output, the pronounced background signal at the input cell border is fused as large plaques, detected objects deviate from the user mask and many false positives are present. By using an appropriate, optimized input routine, the focal adhesion signal is separated well from the background and adhesions are detected. More detected adhesions match with the user mask and false positives are largely diminished as well. The results are summarized in **Fig 3.S2E**.

There is an increase in the multiMatchesOneToN parameter for the optimized routine, because the optimized input routine finely detects adhesions in the boundary areas of high background, where some of them have been marked as large single adhesions by the user when the signal couldn't be distinguished finely by eye. Thus, several objects detected by the output in these areas are matched to one object marked by the user. Conversely, if the output had detected a large object from signal that was distinguished as several objects by the user, that would result in an increase in the multiMatchesNToOne parameter.

Fig 3.S2: Using an optimal input routine increases the similarity of output with user mask.

A) Grayscale image of adhesions, ventral plane of MRC5 cell immunostained for paxillin. B) Binary mask of adhesion ROIs manually marked by user expert from A through Fiji software. C) Un-optimized output vs user mask comparison (Left) FASensor output (Right) Objectwise evaluation map (found- blue, missed-yellow, false positive-red) D) Optimized output vs user mask comparison (Left) FASensor output (Right) Objectwise evaluation map (found- blue, missed-yellow, false positive-red) E) Table comparing results between un-optimized and optimized evaluations.

A.

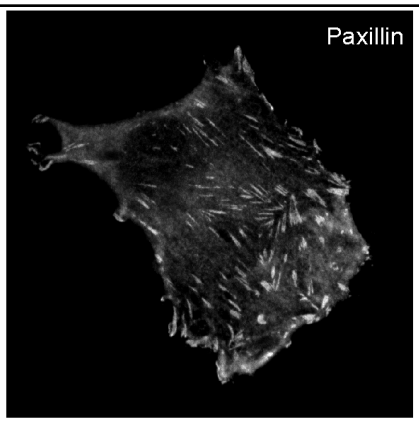

B.

C. Un-optimized software output evaluation

FASensor output

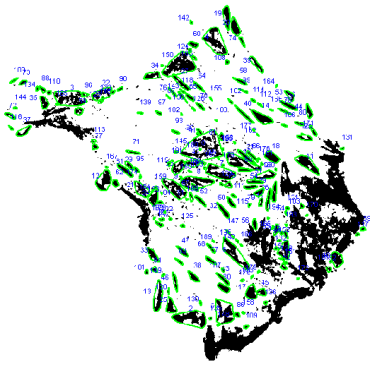

Objectwise Eval

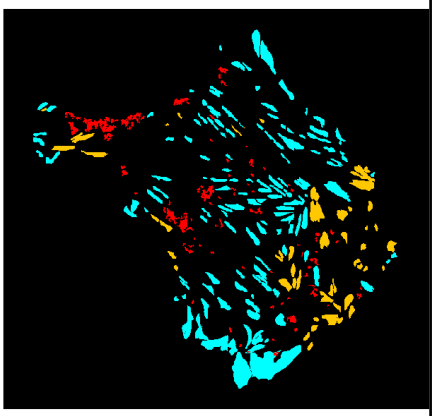

D. Optimized software output evaluation

FASensor output

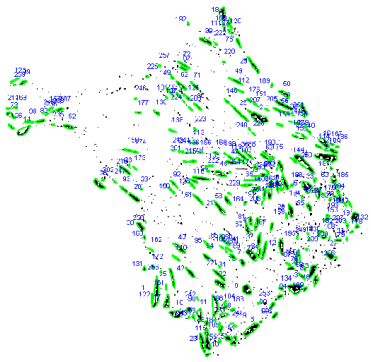

Objectwise Eval

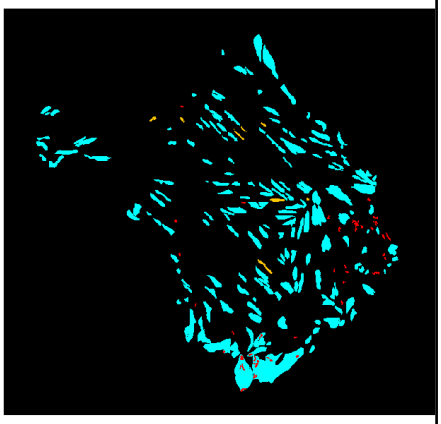

E.

Parameter	Un-optimized	Optimized
Objects found	114	148
Objects missed	43	9
Objects FP	85	37
MultimatchesonetoN	8	40
MultimatchesNtoone	8	0

3.3.2 FASENSOR OUTPUT PERFORMANCE WITH VARYING IMAGING CONDITIONS AND LEVELS OF OPTIMIZATION

To test FASensor's robust detection of focal adhesions on a variety of image qualities, we compiled comparison datasets with varying degrees of blur, in which structures were manually labelled by a human expert for comparison. MRC5 cells immunostained for actin filaments and focal adhesions were imaged on a confocal laser-scanning microscope in three conditions with blur introduced in images by altering the size of pinhole to include out-of-focus light. For the Confocal in-focus dataset (**Fig 3.5A**), the pinhole size was 1.2 Airy Units (AU), for the Confocal mild blur dataset (**Fig 3.5B**), the pinhole size was 3 AU and for the Confocal severe blur dataset (**Fig 3.5C**), the pinhole size was 4.7 AU.

Since the FilamentSensor module has been analyzed and published before, we have focused on the FASensor module for manual annotation comparison. We analyzed a set of adhesion images from each imaging condition (in-focus, mild blur and severe blur) in the FASensor software and compared the software results with adhesions manually annotated for the respective images. For manual annotation by the user expert, selected images from the sets were marked for adhesions using the freehand selection tool in Fiji with the aim of being natively user-detected. Images were traced with minimal signal manipulation to compare the base-level manual annotation by eye with the objects traced by FASensor module after processing by software.

To further understand whether and how user involvement such as pre-processing each image in a set differently or splitting ROIs and excluding adhesions makes a significant improvement in software results, we used three different optimization levels. In the unoptimized (UN) level, the user sets a single desired input routine with thresholding and pre-processing parameters for all images in the dataset and derives results from the software. There is no optimization for each cell in the dataset and user involvement is low. In the optimized (OP) level, the user sets a custom input routine for each cell with the optimal thresholding and pre-processing parameters and derives results from the software. This optimization uses the software's capability for pre-

processing and thresholding to enhance adhesion recognition for every cell according to user's discretion. The user involvement is greater than unoptimized in that every cell has a different optimal setting. In the customized (CM) level, the user sets a custom input routine for each cell and further edits the result by splitting ROIs and deleting adhesions detected so that the result is highly customized and similar to the user manually marking the adhesions. Customization is useful for conditions where the user does not have the time to mark adhesions manually but still desires the detected adhesions to exactly fit to their discretion of the adhesion pattern in an image. The user involvement is thus higher than unoptimized and optimized levels.

Comparison of the software output with the manually marked adhesions gives result categories of adhesions that are found, missed or false positives. To compare these three results in the three optimization conditions, we created a similarity coefficient ($\mathcal{SC}$) for adhesion detection that is as follows:

$$\mathcal{SC} = \frac{\sum Found\ FA\ area}{\sum Missed\ FA\ area + \sum False\ positive\ FA\ area}$$

The higher the coefficient, the more similar the detected adhesions are to the human expert's mask.

For the cells in the In-Focus dataset (**Fig 3.5D**) the similarity coefficients show that adhesions detected in OP ($\overline{\mathcal{SC}} = 12.73$) and CM ($\overline{\mathcal{SC}} = 14.83$) sets are significantly more user-similar compared to the UN set ($\overline{\mathcal{SC}} = 4.53$). The similarity coefficient of the OP and CM sets are not significantly different. Just setting optimal pre-processing settings vastly improves similarity of detected adhesions between cells in the in-focus set, even without further time-intensive customization of splitting and deleting detected objects.

For the cells in the mild-blur dataset (**Fig 3.5E**) the similarity coefficients show that OP set ($\overline{\mathcal{SC}} = 7.98$) is not significantly more similar than UN ($\overline{\mathcal{SC}} = 4.47$) or CM ($\overline{\mathcal{SC}} = 10.13$), whereas CM is significantly more similar than UN. Thus, in conditions where

images have some blur, doing both optimal pre-processing and user customization by splitting and deleting adhesions makes it significantly more accurate.

For cells in the severe-blur dataset (**Fig 3.5F**), the similarity coefficients show that OP set ($\overline{SC} = 5.94$) is not significantly more similar than UN ($\overline{SC} = 3.47$), but again CM ($\overline{SC} = 11.74$) is significantly more similar than both other sets. Thus, in conditions where images are blurred, intensive user customization by splitting and deleting adhesions gives the best result.

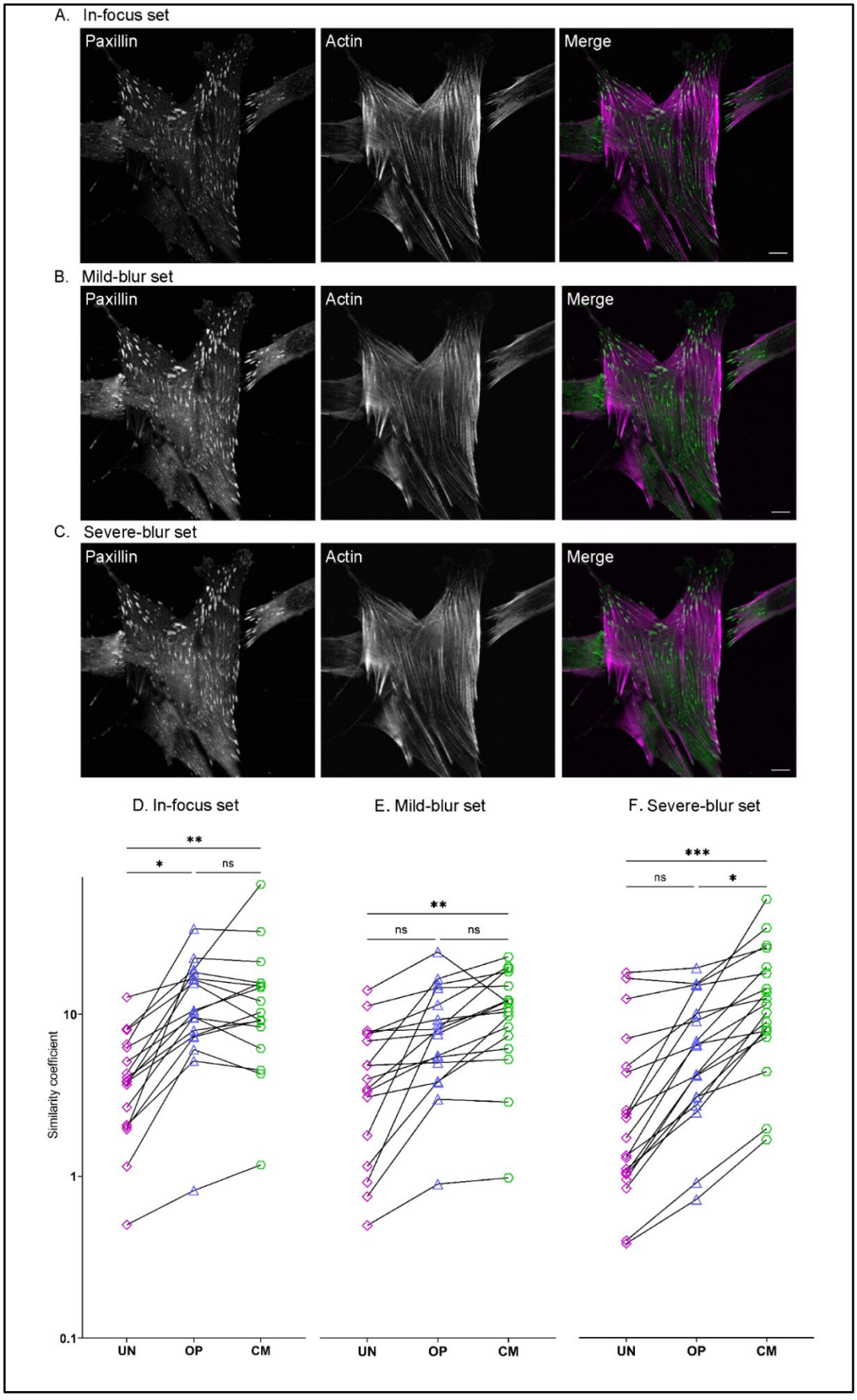
A. In-focus set
Paxillin
Actin
Merge
B. Mild-blur set
Paxillin
Actin
Merge
C. Severe-blur set
Paxillin
Actin
Merge
D. In-focus set
E. Mild-blur set
F. Severe-blur set
**
*
ns
**
ns
ns
***
ns
*
Similarity coefficient
10
1
0.1
UN
OP
CM
UN
OP
CM
UN
OP
CM

Fig 3.5. Datasets' imaging conditions and similarity coefficients ($\mathcal{SC}$) for the datasets by level of optimization.

A-C) Representative images of MRC5 cells fluorescently stained for actin filaments (phalloidin) and adhesions (paxillin) is shown. Scale bar—10 μm. All images were taken with a confocal microscope and are of the ventral plane of the cell. (Left) Grayscale image of the adhesions (Center) Grayscale image of actin filaments (Right) Merged image of the cell with actin filaments in magenta and adhesions in green. A) In-focus setting. B) Mild-blur setting. C) Severe-blur setting. D) $\mathcal{SC}$ *on the y-axis (logarithmic scale) for unoptimized 'UN' (purple squares), optimized 'OP' (blue triangles) and for customized 'CM' (green hexagons) output of analyzed images of the in-focus set (n = 17, UN* $\overline{\mathcal{SC}} = 4.53$*, OP* $\overline{\mathcal{SC}} = 12.73$ *and CM* $\overline{\mathcal{SC}} = 14.83$*), E) Mild-blur set (n = 17, UN* $\overline{\mathcal{SC}} = 4.47$ *, OP* $\overline{\mathcal{SC}} = 7.98$ *and CM* $\overline{\mathcal{SC}} = 10.13$*) and F) Severe-blur set (n = 19, UN* $\overline{\mathcal{SC}} = 3.47$*, OP* $\overline{\mathcal{SC}} = 5.94$ *and CM* $\overline{\mathcal{SC}} = 11.74$*). *** p <0.001; ** p <0.01; * p <0.05 and ns stands for not significant (p >0.05).*

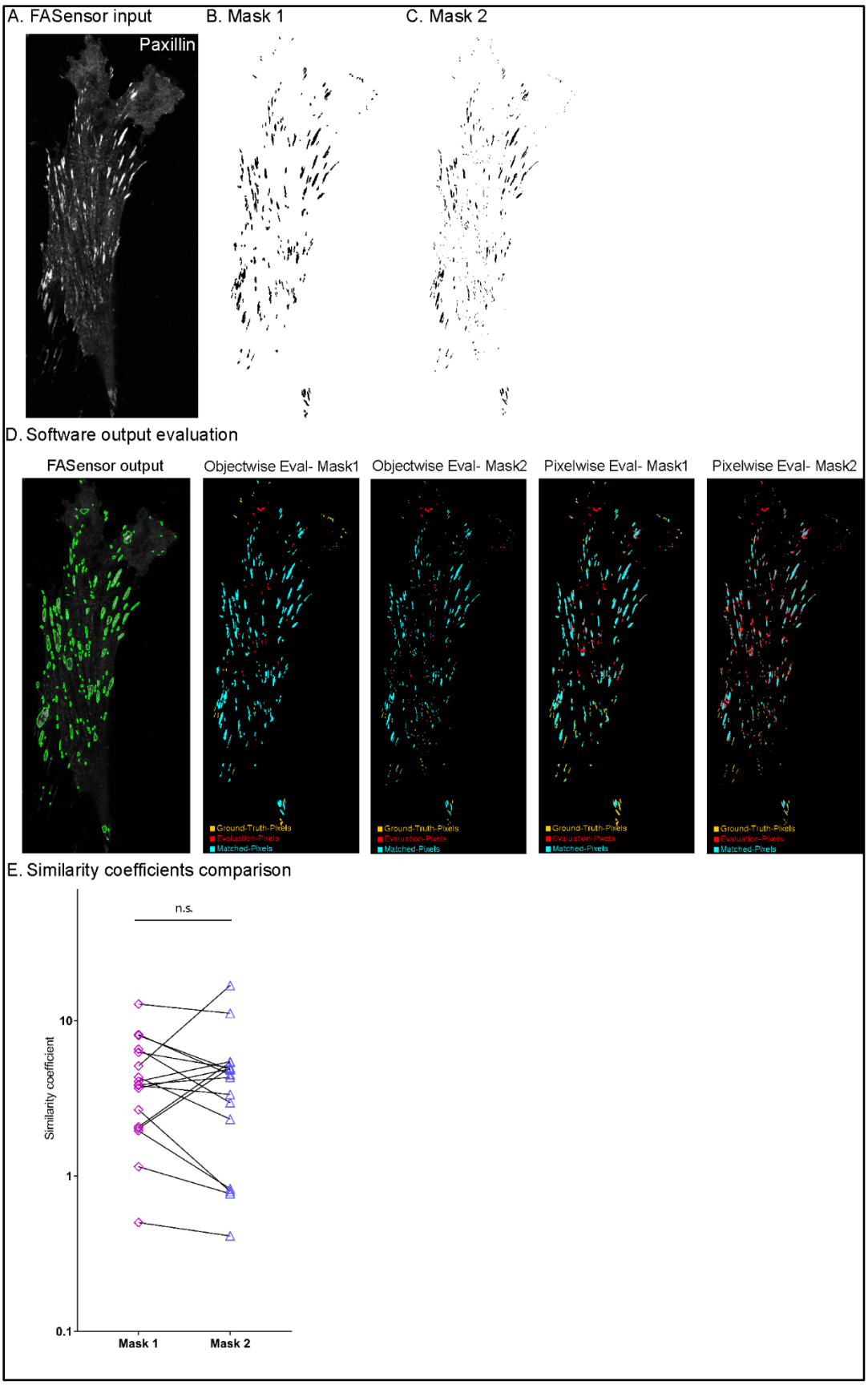
A. FASensor input
Paxillin
B. Mask 1
C. Mask 2
D. Software output evaluation
FASensor output
Objectwise Eval- Mask1
Objectwise Eval- Mask2
Pixelwise Eval- Mask1
Pixelwise Eval- Mask2
Ground-Truth-Pixels
Evaluation-Pixels
Matched-Pixels
E. Similarity coefficients comparison
n.s.
Similarity coefficient
10
1
0.1
Mask 1
Mask 2

Fig 3.S4: Comparison with annotations from two human experts.

A) FASensor input of IF adhesion image showing the ventral plane of a MRC5 cell immunostained with paxillin. B) Binary mask of adhesion ROIs marked by user expert 1. C) Binary mask of adhesion ROIs marked by user expert 2. D) Evaluation output for pixel-wise and object-wise comparison of human expert annotations compared to FASensor output. E) Similarity coefficient of human expert annotated masks, human expert 1 ($\overline{SC} = 4.53$), human expert 2 ($\overline{SC} = 4.63$).

Aggregate analysis (**Fig 3.S3**) of all the adhesions in the sets reveal that false positive adhesions are consistently significantly smaller than found and missed adhesions across optimization levels and missed adhesions are significantly smaller than found adhesions as well. **Fig 3.6** shows graphs comparing the adhesion objects by area in a set across optimization levels.

Aggregate analysis of the in-focus set (**Fig 3.6A**) shows that there is no significant difference between area of the found objects across optimization levels, but both OP (1843) and CM (1802) find more adhesions compared to UN (1451). OP (268) and CM (309) miss less adhesions than UN (660) and CM missed adhesions are significantly smaller than UN. Optimization decreases false positive adhesion area significantly- with CM ($\overline{A} = 0.33\ \mu\text{m}^2$) and OP ($\overline{A} = 0.25\ \mu\text{m}^2$) adhesions being significantly smaller than UN ($\overline{A} = 0.43\ \mu\text{m}^2$) false positive adhesions. OP shows the largest decrease in false positive adhesion size, but CM (296) has the largest decrease in number over UN (497) and OP (465). Thus, optimization of in-focus images primarily increases the accuracy by finding more objects and decreasing false positives by number and area.

Aggregate analysis of the mild blur set (**Fig 3.6B**) shows that there is no significant difference between the area of found objects across optimization levels, but both OP (1740) and CM (1700) find more objects compared to UN (1522). In missed objects both OP ($\overline{A} = 0.66\ \mu\text{m}^2$) and CM ($\overline{A} = 0.64\ \mu\text{m}^2$) have smaller missed adhesion

area compared to UN ($\overline{A} = 0.83\ \mu\text{m}^2$), and less missed adhesions (OP (361), CM (401)) than UN (579) as well. Comparing the false positive objects, OP has lower $\overline{A}(\overline{A} = 0.31\ \mu\text{m}^2$) compared to UN ($\overline{A} = 0.42\ \mu\text{m}^2$) and CM ($\overline{A} = 0.43\ \mu\text{m}^2$), the number of false positives (560) is lower than UN (791) but higher than CM (188). Thus, in mild blur images, optimization method shows improvement over unoptimized by finding more adhesions and having fewer false positives. Customization shows much fewer false positives compared to other levels.

Aggregate analysis of the severe blur set (**Fig 3.6C**) shows that there is no significant difference between area of found objects across optimization levels, but both OP (1520) and CM (1577) find more adhesions than UN (1504). In missed objects, both OP ($\overline{A} = 0.61\ \mu\text{m}^2$) and CM ($\overline{A} = 0.60\ \mu\text{m}^2$) are significantly smaller than UN ($\overline{A} = 0.85\ \mu\text{m}^2$). More adhesions are missed in UN (355) compared to OP (339) and CM (282) as well. Comparing the false positives, UN ($\overline{A} = 0.43\ \mu\text{m}^2$) has the highest mean area $\overline{A}$ compared to OP ($\overline{A} = 0.36\ \mu\text{m}^2$) and CM ($\overline{A} = 0.36\ \mu\text{m}^2$). OP (745) and CM (231) have lower number of false positives compared to UN (1811) as well. Thus, for severely blurred images, optimization method shows improvement over unoptimized by finding more adhesions and having fewer false positives. Customization shows a greater improvement by having much fewer missed adhesions and false positives compared to other levels.

Thus FASensor offers several levels of desired user optimization in a variety of imaging conditions to derive and evaluate an accurate adhesion map from the input.

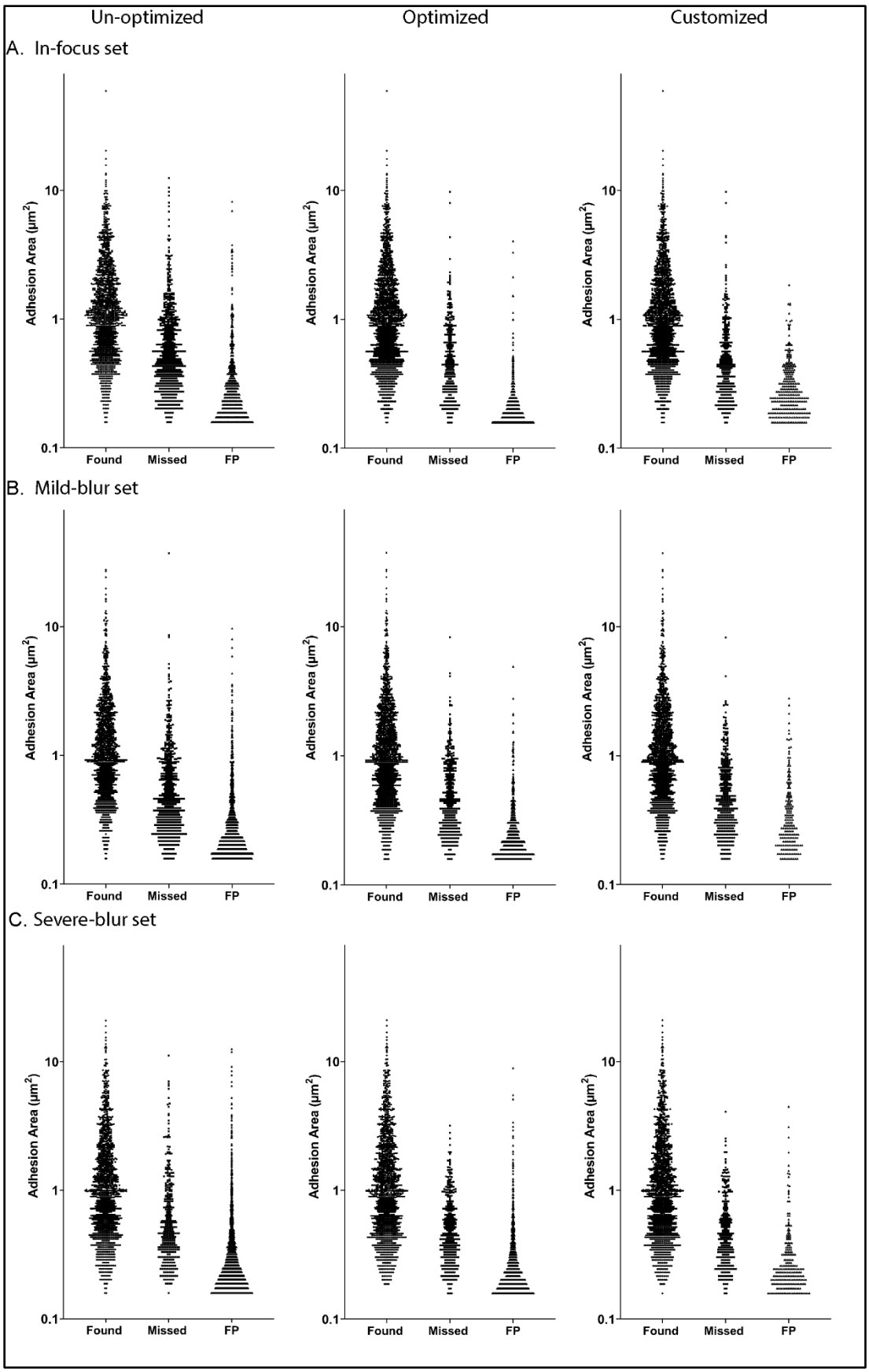
Un-optimized
Optimized
Customized
A. In-focus set
B. Mild-blur set
C. Severe-blur set
Adhesion Area (μm²)
10
1
0.1
Found
Missed
FP

Fig 3.S3: False positives and missed adhesions are much smaller than found adhesions.

Graphs show pooled adhesion objects for found, missed and false positive (FP) categories in a set. Y axis is adhesion area in μm² on a logarithmic scale. Left column shows un-optimized setting graphs, middle column shows optimized setting graphs and right column shows customized setting graphs. A) In focus set (Left) Found n = 1451 $\overline{A} = 1.73\ \mu m^2$*, Missed n = 660* $\overline{A} = 0.86\ \mu m^2$ *and FP n = 497* $\overline{A} = 0.43\ \mu m^2$*; (Middle) Found n = 1843* $\overline{A} = 1.57\ \mu m^2$*, Missed n = 268* $\overline{A} = 0.71\ \mu m^2$ *and FP n = 465* $\overline{A} = 0.25\ \mu m^2$*; (Right) Found n = 1802* $\overline{A} = 1.59\ \mu m^2$*, Missed n = 309* $\overline{A} = 0.68\ \mu m^2$ *and FP n = 296* $\overline{A} = 0.33\ \mu m^2$*; B) Mild-blur set (Left) Found n = 1522* $\overline{A} = 1.64\ \mu m^2$*, Missed n = 579* $\overline{A} = 0.83\ \mu m^2$ *and FP n = 791* $\overline{A} = 0.42\ \mu m^2$*; (Middle) Found n = 1740* $\overline{A} = 1.57\ \mu m^2$*, Missed n = 361* $\overline{A} = 0.66\ \mu m^2$ *and FP n = 560* $\overline{A} = 0.31\ \mu m^2$*; (Found n = 1700* $\overline{A} = 1.60\ \mu m^2$*, Missed n = 401* $\overline{A} = 0.64\ \mu m^2$ *and FP n = 188* $\overline{A} = 0.43\ \mu m^2$*; C) Severe-blur set (Left) Found n = 1504* $\overline{A} = 1.61\ \mu m^2$*, Missed n = 355* $\overline{A} = 0.85\ \mu m^2$ *and FP n = 1811* $\overline{A} = 0.43\ \mu m^2$*; (Middle) Found n = 1520* $\overline{A} = 1.66\ \mu m^2$*, Missed n = 339* $\overline{A} = 0.61\ \mu m^2$ *and FP n = 745* $\overline{A} = 0.36\ \mu m^2$*; (Right) Found n = 1577* $\overline{A} = 1.62\ \mu m^2$*, Missed n = 282* $\overline{A} = 0.60\ \mu m^2$ *and FP n = 231* $\overline{A} = 0.36\ \mu m^2$*.*

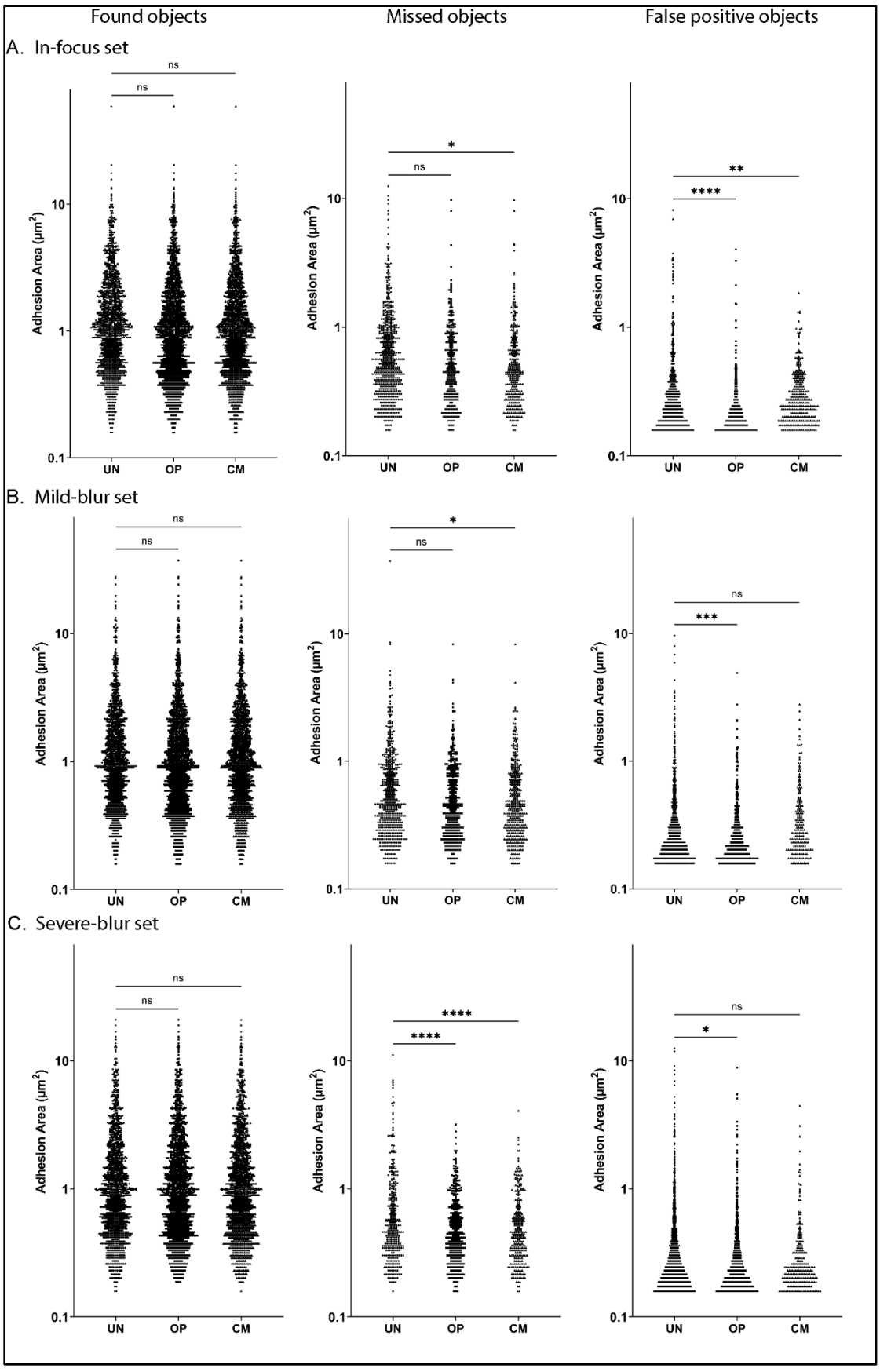
Found objects
Missed objects
False positive objects
A. In-focus set
B. Mild-blur set
C. Severe-blur set
Adhesion Area (μm²)
0.1
1
10
UN
OP
CM
ns
*
**
***
****

Fig 3.6. Comparison of adhesion objects between optimization levels in a set.

*Graphs show pooled adhesion objects for un-optimized 'UN', optimized 'OP' and customized 'CM' analysis. Y axis has adhesion area in μm^2 on a logarithmic scale. Left column shows graphs comparing adhesion objects found in common between user mask and software output. Middle column shows adhesion objects that were missed in output and present only in user mask. Right column shows adhesion objects that are false positive, present only in the software output. A) Graphs for in-focus set B) Graphs for mild-blur set C) Graphs for severe-blur set. **** p <0.0001; *** p <0.001; ** p <0.01; * p <0.05 and ns stands for not significant (p >0.05).*

DETECTION OF STRESS FIBERS WITH FILAMENTSENSOR

The FilamentSensor, as integrated here in the FAFCK, is based on the version published by Eltzner et al in 2015, adjusted to feature stack handling of image sequences and drastically reduced runtime as well as some additions for area calculation. The plugin featured in the FAFCK includes all components included in the stand-alone software, being a preprocessing, line sensor, and filament submenu. The workflow of the software as published before is included in **Fig 3.S5**.

During preprocessing, contrast and brightness can be adjusted for either individual pictures or a whole stack, if needed. These routines are based on ImageJ (Schneider et al, 2012), which is included as an internal library and used wherever possible, as the ImageJ routines are fast and well tested. The main preprocessing step consists of a filter queue which the user can customize to their needs. This is necessary to prepare the original IF filament image for binarization, tackling the issue of crossing filaments that would otherwise be recognized as a network of interconnected, not crossing, filaments. On this image, the binarization is applied and filament objects extracted according to the flowchart shown in **Fig 3.S5**. This is done in parallel threads to improve runtime and subjected to several boundaries the user can determine including minimal and maximal length, maximal curvature, width, restriction to cell area mask, and

more. This flexibility allows for the program to be utilized for a wide variety of filament types. Lastly, the filament subsection allows to filter data for export. The FilamentSensor module offers a set of descriptors of the whole cell such as IDs, area, aspect ratio, length of axes, number of filaments, orientation, brightness, and for each individual filament such as xy position, length, curvature, width, and orientation. For each image file, the filament objects are assigned an individual identifier as done for the focal adhesion objects and a variety of export types are available with the option of superimposing filaments as required.

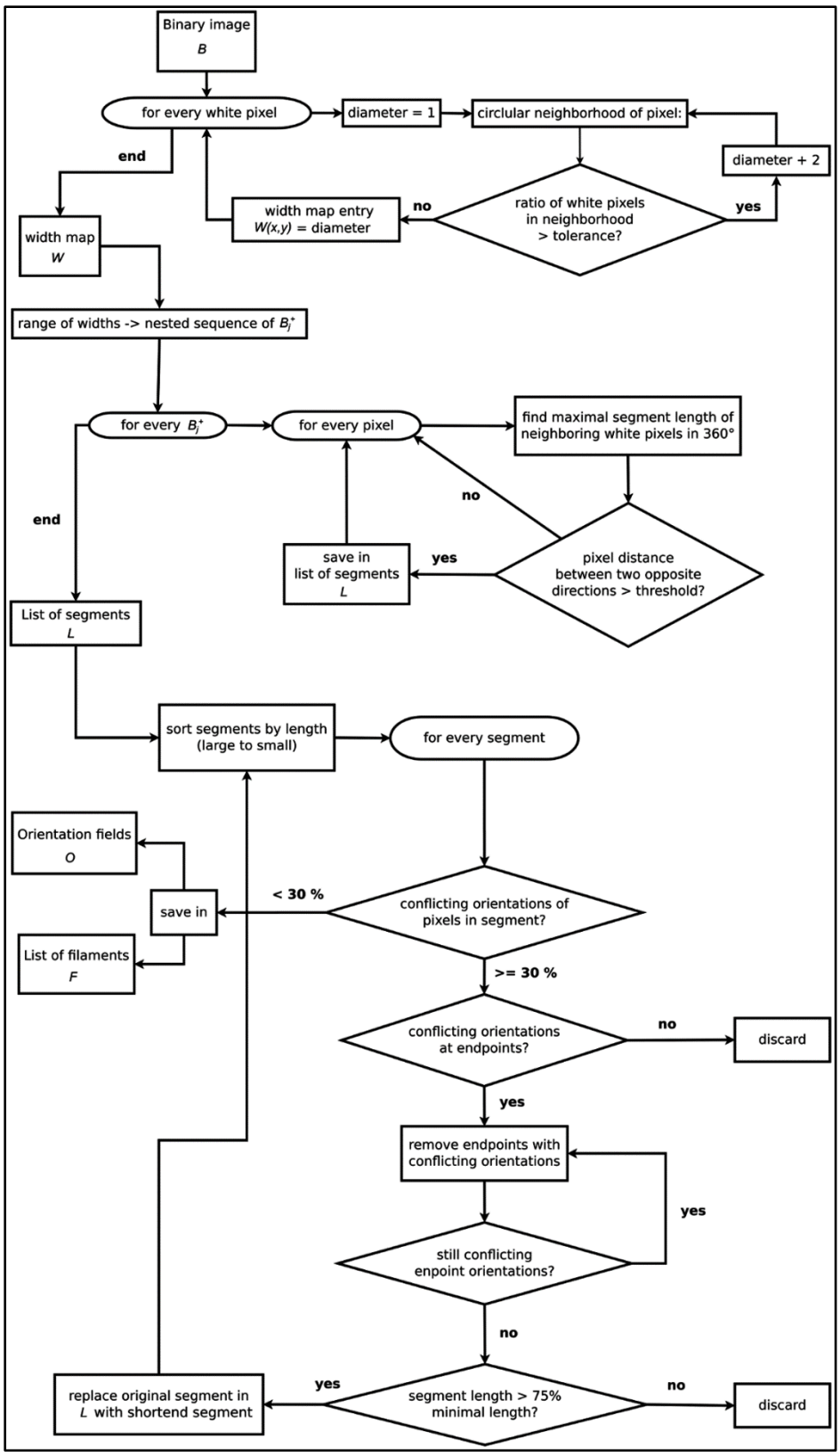

Fig 3.S5: Workflow for FilamentSensor.

CORRELATION OF DETECTED FOCAL ADHESIONS AND ACTIN FILAMENTS IN FAFCK

As focal adhesions and actin filaments are linked structures, the FAFCK module offers correlation of detected focal adhesions from FASensor and filaments from FilamentSensor. The software's workflow is illustrated in **Fig 3.7**.

Using the file name of the original images or image stacks loaded, it is first checked whether input data for both adhesions and filaments exist and single sets are ignored. The focal adhesion objects detected from the input image showing paxillin are paired with the filaments derived from the input image depicting actin (see **Fig 3.8A and 3.8B**).

Both list of found objects are sorted by size and usually tasks start with the larges object. For correlation, one fiber object is taken and all focal adhesion objects are tried for correlation. To reduce computational efforts, only focal adhesions with long axis smaller than fiber total length are tried, assuming a focal adhesion can never be larger than the corresponding fiber. For the focal adhesion objects, the user decides whether the convex hull, fitted ellipse, or true pixels is used for verification purposes. This ellipse is calculated by setting the line between the two points with the greatest distance on the convex hull as long axis and the axis orthogonal to that and with the greatest length as short axis. Furthermore, the area can be artificially increased by increasing the neighborhood in which verification is done. Now, starting from the ends, for each point on the filament, a neighborhood rectangle is created and in the list of focal adhesions with main axis length below filament length, intersecting objects are searched.

The correlation can be done with condition of either validating all filaments that are attached to at least a single adhesion or only validating those with multiple adhesion structures along the filament. Thus, we can clearly categorize filaments by the number of adhesions associated. The data of adhesions by number of filaments associated can also be derived.

The output of the correlation routine consists of the identifier numbers of the respective objects and can consecutively be matched to the data output of the previous routines. Also, verified filaments will be highlighted in the fiber overlay and after verification the fiber data export will be expanded by a 'verification' column with booleans. As with the individual modules themselves, batch analysis of correlation for pairs of FA and SF images are possible as well.

The output is displayed in the Stress Fiber Overlay window in the main tab in FAFCK. The resulting paired filament and focal adhesion IDs are displayed in a table in the Focal Adhesion tab. The results can be exported as a simple overlay or a comprehensive color-coded map (**Fig 3.8C**), verifier tables, and grouped CSV files with details of adhesions and filaments by association with each other.

We used the FAFCK to correlate detected adhesions with filaments in the in-focus dataset (n = 17). We named filaments by adhesion association as MAAF- Multiple adhesion associated filament, SAAF—Single adhesion associated filament and NAAF—Not adhesion associated filament. There were 490 MAAFs, 588 SAAFs and 555 NAAFs, with MAAFs having significantly higher mean fiber length of 13.14 μm compared to SAAFs at 9.29 μm and NAAFs at 7.15 μm (**Fig 3.8D**). Thus, filaments attached to multiple adhesions are longer than those attached to only one adhesion or none. We also analyzed adhesions by number of fibers associated with them and grouped them as AAMF—Adhesion associated with multiple fibers, AASF—Adhesion associated with single fiber and AANF—Adhesion associated with no fibers. AAMFs were much fewer (291) than AASFs (1191) and AANFs (1227) and had significantly larger mean adhesion area ($\overline{A} = 1.21\ \mu\mathrm{m}^2$) compared to AASFs ($\overline{A} = 0.64\ \mu\mathrm{m}^2$) and AANFs ($\overline{A} = 0.34\ \mu\mathrm{m}^2$) (**Fig 3.8E**). The correlation analysis provides a comprehensive picture of adhesion and filament association in cells and can be used to streamline quantitative evaluation of the effective mechanical forces in the stress fiber / focal adhesion system.

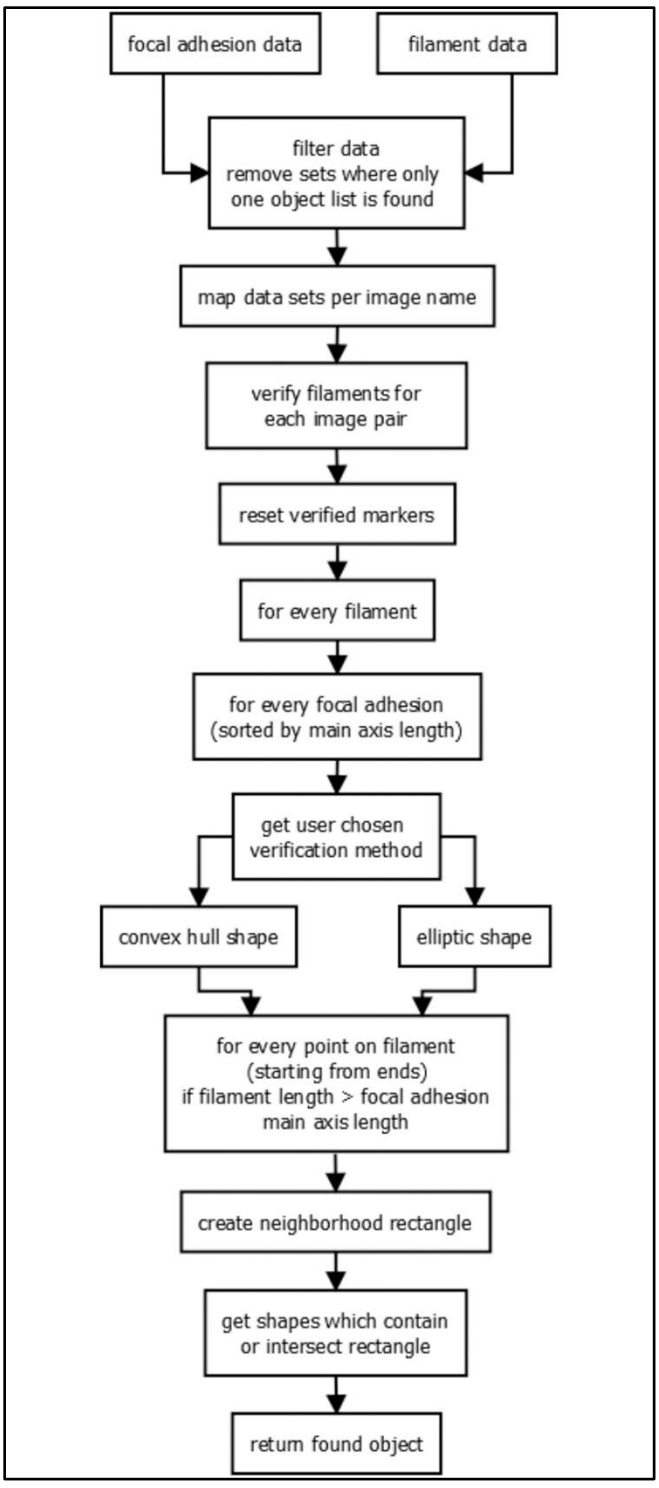

Fig 3.7. Workflow for correlation in FAFCK.

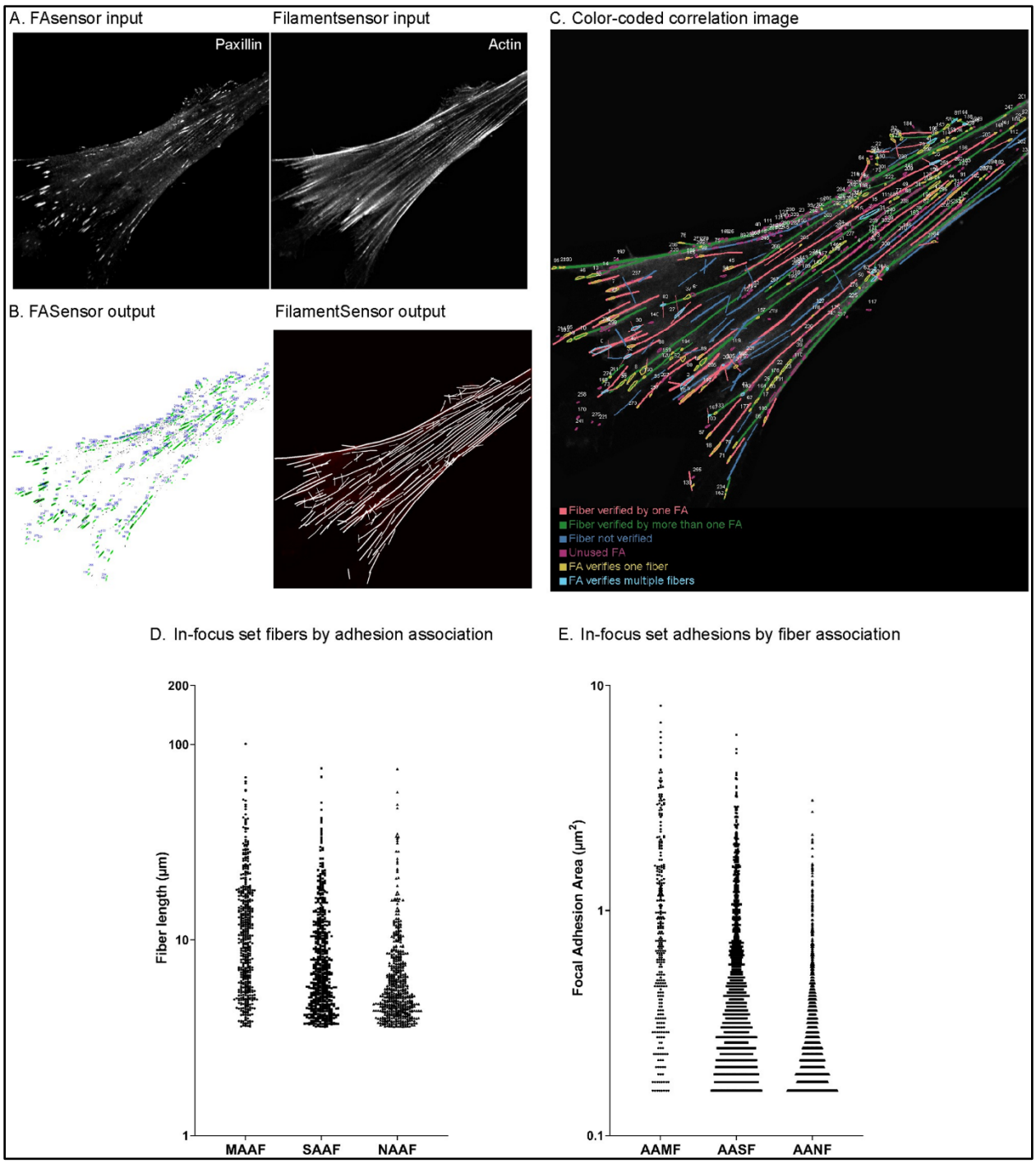

Fig 3.8. Correlation of focal adhesions and actin filaments by FAFCK.

A) Input images of the ventral plane of a MRC5 cell (left) adhesions (paxillin) and (right) actin filaments (phalloidin). B) Map of numbered adhesion objects detected by FASensor (left), map of filaments detected by FilamentSensor (right). C) Color coded map of

correlated adhesions and filaments categorized by association (legend in image). D) Aggregate graph of lengths of filaments categorized by adhesion association in all cells of the in-focus dataset. Y axis is in logarithmic scale. MAAF- Multiple adhesion associated filament, SAAF—Single adhesion associated filament and NAAF—Not adhesion associated filament. E) Aggregate graph of areas of adhesions categorized by filament association in all cells of in-focus dataset. Y axis is in logarithmic scale. AAMF—Adhesion associated with multiple fibers, AASF—Adhesion associated with single fiber and AANF—Adhesion associated with no fibers.

DISCUSSION

Here we present the FAFCK that allows for fast, reliable, unbiased, and systematic detection of fibers and point-like structures and their cross-correlation in cells. While detection and analysis of both types of structures individually is useful, the cross-correlation module will be especially valuable and help to answer open questions on the coupled function of these force-transmitting features in cellular mechanosensing.

There are several notable advantages to our new tool. Importantly, it allows to identify groups of stress fibers associated with zero, one, or more than one focal adhesion. Such classification can be applied to functional differences of stress fibers in cells of specific morphologies. For example, in migrating cells, this allows for a quantification of the relative number and characteristics of transverse arcs (0 FA per filament), dorsal SFs (1 FA per filament), and ventral SFs (≥2 FAs per filament) in large data sets. This analysis can also be applied to other types of actin organization in specialized cell types. The software package can also be used to quantify maximum intensity projections from 3D image sets, making it possible to quickly quantify such structures that would be otherwise difficult and time-consuming to analyze. Furthermore, individual application of filters and optimization allows for an optimal analysis of wide-field images and images with high blur and/or background noise.

There is always a certain degree of error or deviation in computational recognition methods (as false positives and false negatives) as well as bias in the user's native detection of cellular features. Our software package allows for the systematic, streamlined, and unbiased comparison of large data sets to achieve statistical relevance. Since we provide an option to customize output in each image, this also allows for more precise detection of SF types in smaller data subsets. We are currently developing the functionality of the FAFCK such that it would be useful for analysis of time lapse movies, where many frames need to be analyzed consecutively with same settings to quantify the dynamics of stress fibers and adhesions in cells to understand their dynamic organization and how they influence the mechanical coupling of cells and the matrix. While our original motivation for this project was the quantitative analysis of focal adhesion structures and their correlation with stress fibers, this tool can be also used for image analysis of other cellular structures from fluorescence microscopy images. This includes but is not limited to membrane organelles such as lysosomes or mitochondria, that can be detected and also tracked to quantify their cellular dynamics.

For optimal flexibility and potential comparative studies, we provide an import option of external data sets of filaments and FAs (source may be manual detection or from other software). This feature allows for comparison of the computational recognition with individual user perception of the biological reality and also allows for importing data from other image analysis platforms to be used for the correlation analysis. In the light of the continuous improvement of image recognition software in the field we specifically refrained from employing machine learning and big data algorithms to establish a solid classical analysis tool. That said, the future development of FAFCK can surely benefit from big data and deep learning additions.

MATERIALS AND METHODS

Software availability

The FAFCK is available under the GNU Public License and can be used, modified and restributed freely without warranty given by the developers. A version of the software, sources, tutorial, installation notes, and example data can be either obtained by the data package associated with this paper (https://doi.org/10.5281/zenodo.5082933) or via our website (http://www.filament-sensor.de). The FAFCK has been tested on Windows and Linux. For Java 8 and below, the.jar file runs on click on windows. Running the FAFCK on Java 9 is not advised. For Java 10 and above, Java does not contain the JavaFX package, which has to be installed separately and the Path added. Also, we advise to use OpenJDK and OpenJFX which both have to be installed and the Path added on Windows and Linux. Detailed instructions how to do this can be found in the Readme in the data folder or on our website.

Cell culture

MRC5 cells (human lung fibroblasts, ATCC® Cat# CCL-171™, RRID:CVCL_0440) were maintained in MEM media (Cat# 11095080, Thermo Fisher Scientific) supplemented with 10% fetal bovine serum, 100 µM penicillin and 0.1 mg/ml streptomycin in 5% CO2 at 37°C. Media was supplemented with 5 µg/ml Plasmocin (Cat# ant-mpp, InvivoGen) as a prophylactic against mycoplasma contamination.

Fixation and immunostaining

MRC5 cells were seeded on glass coverslips (Cat# NC1129240, Fisher Scientific) that had been coated with 10 µg/ml fibronectin (Cat# FC010, EMD Millipore) for 1 hour. After 24 hours, cells were fixed with 4% paraformaldehyde prepared in CB (cytoskeletal buffer—150mM NaCl, 5mM MgCl2, 5mM EGTA, 5mM glucose, 10mM MES), for 10 minutes at room temperature. They were washed with CB after fixation, permeabilized with 0.25% Triton in CB. Antibodies used are as follows: anti-paxillin mouse primary antibody (1:200, BD Biosciences Cat # 610051, RRID:AB_397463), Alexa Fluor

568 Phalloidin (1:300, Invitrogen, Cat# A12380) and Alexa Fluor 488 conjugated goat anti-mouse IgG secondary antibody (1:300, Thermo Fisher Scientific Cat# A-11001, RRID:AB_2534069). Coverslips were post-fixed for 10 min with 4% PFA in CB at room temperature. They were mounted with Vectashield Mounting Medium (Cat # H-1000–10, Vector Labs) on glass slides (Cat # 12–550-343, Fisher Scientific).

Confocal microscopy

Immunostained samples were imaged using a laser scanning confocal microscope- Nikon A1R HD25 configured with a Ti2-E inverted microscope, with a 100× oil immersion objective (MRD01991, N.A. = 1.49). Three different pinhole settings were used to adjust the amount of out-of-focus light in the images- 1.2 AU (small, in-focus), 3 AU (intermediate, mild blur) and 4.7 AU (large, severe blur). Alexa Fluor 488 was excited with a laser of wavelength 488 nm and Alexa Fluor 568 with 561 nm, respectively.

Input files from microscopy images

To ensure accurate analysis of the desired cell, we edited the IF images with multiple cells in the field of view by outlining the cell of interest, noting the background value and filling the area outside the cell with the background. This edited image was taken as the input for the FASensor and FilamentSensor modules. In cases where simply cropping the image could isolate the cell of interest, we did so.

Manual annotation by human expert

Images were manually marked for FAs by a human expert (17 images for in-focus set, 17 images for mild blur set, 19 images for severe blur set) and in addition the in-focus set was marked by a second independent human expert. FAs were marked using the freehand selection tool in Fiji (Schindelin et al, 2012). The binary mask of marked adhesions were used as input in evaluation against the software's output.

Bulk dataset evaluation analysis

To avoid detecting noise and artifacts, we set the lower limit of adhesion detection in the software to 10 pixels which corresponds to 0.144 μm2 and upper limit at

1000 px which corresponds to 14.4 μm2. The unoptimized routine across the imaging sets is as follows- For In-Focus dataset, Gauss filter (Sigma-1) and Laplace filter (1, 4 neighbor) with Intermodes thresholding at 55 was used. For Mild-Blur dataset, Gauss filter (Sigma-1) and Laplace filter (1.5, 8 neighbor) with Intermodes thresholding at 80 was used. For Severe-Blur dataset, Gauss filter (Sigma-1) and Laplace filter (3, 8 neighbor) with Intermodes thresholding at 80 was used. Further optimization and customization was done according to user discretion.

Closing and Fill holes function was not used for bulk analysis adhesion detection. We used 1 percent minimum matching pixels for object matching in evaluation. Thicken lines function was not used in evaluation. Areas of found and missed adhesions were derived from the pixels column for the user's mask in the result table. Areas of false positive adhesions were derived from the pixels column of the software output in the result table. Pixel values from software results were converted to corresponding micron values using the scale of input image and plotted on graphs. Ordinary one-way ANOVA followed by Dunnett's multiple comparisons test or Tukey's multiple comparisons test was performed using GraphPad Prism (Ver 9.0.0 for Windows, GraphPad Software, San Diego, California USA, www.graphpad.com). For the in-focus set FA-filament correlation analysis, we used the optimization method where each cell had a custom optimal pre-processing filter setting in FASensor. For FilamentSensor, the default settings were used for all cells. For verification, we chose ellipse and a neighborhood of 1.

Batch threshold determination with ThresholdFinder

The ThresholdFinder application is an additional software tool that we provide alongside the FAFCK. From a small amount of user-annotated masks, it determines best applicable thresholding algorithm and setting in the FAFCK software. From the input of original images and binary annotations, the software uses the mask to determine desired regions of the image and feeds this into all thresholding algorithms. To determine found, false positive and false negative rates, the images are processed whole

with the selected algorithm. The value that the respective algorithm would choose without mask input is given, too.

CHAPTER 4:

CONCLUSIONS AND FUTURE DIRECTIONS

The ventral actin cytoskeleton is a complex and dynamic network that involves contractile actin and focal adhesion interactions to create ventral stress fibers that are functionally significant in cellular force production and migration. While the mechanisms of VSF formation have been elucidated in previous literature (Hotulainen & Lappalainen, 2006; Lehtimäki et al, 2021), the process of VSF remodeling and associated adhesion dynamics in steady state conditions needed further study. In addition, a computational tool with customizable algorithms to analyze stress fiber architecture and associated focal adhesions reliably in datasets was sorely needed.

Through my research described in Chapter 2, we have thoroughly characterized a novel process of VSF remodeling in steady state by 'merging' of fibers at focal adhesions in the ventral plane. Using an experimental system of migratory lung fibroblasts and computational modeling, we have shown that merging employs adhesion disassembly and contractile cohesion of smaller fibers to form long ventral stress fibers that are aligned to the cellular axis. Our study shows that the joining of primary and secondary fibers through formation of a myosin bridge and intervening adhesion disassembly are crucial steps in the merging process, and these steps are interlinked in terms of dynamics, affecting the efficiency of merging.

Merging is mechanosensitive and the balance of contractile forces at the merge point is integral to the success of the process. We elucidate the importance of parallel orientation of the merging fibers for efficient merging, and how other conformations lead to strengthening of the adhesion and thus failure of the merge event. Thus, merging serves as a contractile force-mediated process that transforms the ventral actin stress fiber network to create long VSFs and aligns the contractile forces produced.

In future studies of the VSF network, quantitative analysis of the traction stresses produced by the cell using traction force microscopy (Plotnikov et al, 2014) will provide a deeper view into how the dynamic force landscape relates to the changing VSF network as a result of merging, given that VSFs have been shown to produce the highest traction forces in the cell (Soiné et al, 2015). As merging produces longer and aligned fibers, we predict that this would result in increased force magnitude and promote the directionality of traction forces. This in turn would facilitate cell migration and remodeling of the extracellular matrix (Lemmon et al, 2009; Lekka et al, 2021).

Studies involving laser nano-surgery of the fibers involved in merging are recommended to further dissect the tensions involved at the intervening adhesion and evaluate the contribution of each merging component to the force balance at the merge point (Lee et al, 2018). In addition to the mechanobiological studies, mechanistic studies on the specific actin crosslinking factors at the merge point (such as alpha-actinin) will provide clarity into the proteins involved in the primary and secondary fiber linkage. Investigations in other cell types such as arterial and cancer cells will provide insight into how merging can facilitate VSF network formation in varied environments.

Through my research described in Chapter 3, we have created a novel standalone computational tool with integrated focal adhesion and stress fiber analysis to comprehensively quantify the actin-adhesion architecture in cells. The Focal Adhesion Filament Cross-correlation Kit introduces a new tool for focal adhesion detection and analysis through the Focal Adhesion Sensor and improves on the previously published Filament Sensor tool as well. The novel pairing of the detected structures from each module for cross-correlation produces a thorough map of the association of focal adhesions and stress fibers in the cell, allowing users to analyze stress fiber subtypes in their datasets through a reliable computational tool for the first time. FAFCK provides a high degree of user customizability and an evaluation module to optimize their input routine and derive specific detection and output of their images. By accepting input images as binary masks from other softwares, FAFCK provides easy integration of the tool into established quantitative methodologies in the cytoskeletal analysis field. In further

updates to the computational software, we expect to integrate machine learning and dynamic tracking capabilities into the modules, allowing for smart detection and temporal analysis of the focal adhesion-stress fiber network in future studies.

REFERENCES

Abercrombie, M. T. E. M., Heaysman, J. E., & Pegrum, S. M. (1971). The locomotion of fibroblasts in culture: IV. Electron microscopy of the leading lamella. Experimental cell research, 67(2), 359-367.

Akin, O., & Mullins, R. D. (2008). Capping protein increases the rate of actin-based motility by promoting filament nucleation by the Arp2/3 complex. *Cell*, *133*(5), 841-851.

Asakura, S. (1961). The interaction between G-actin and ATP. *Archives of biochemistry and biophysics*, *92*(1), 140-149.

Atherton, P., Stutchbury, B., Jethwa, D., & Ballestrem, C. (2016). Mechanosensitive components of integrin adhesions: Role of vinculin. *Experimental cell research*, *343*(1), 21-27.

Bach, C. T., Creed, S., Zhong, J., Mahmassani, M., Schevzov, G., Stehn, J., ... & O'Neill, G. M. (2009). Tropomyosin isoform expression regulates the transition of adhesions to determine cell speed and direction. *Molecular and cellular biology*, *29*(6), 1506-1514.

Barczyk, M., Carracedo, S., & Gullberg, D. (2010). Integrins. Cell and tissue research, 339(1), 269-280.

Barua, B., Nagy, A., Sellers, J. R., & Hitchcock-DeGregori, S. E. (2014). Regulation of nonmuscle myosin II by tropomyosin. Biochemistry, 53(24), 4015-4024.

Berginski, M. E., & Gomez, S. M. (2013). The Focal Adhesion Analysis Server: a web tool for analyzing focal adhesion dynamics. *F1000Research*, *2*.

Blanchoin, L., & Pollard, T. D. (2002). Hydrolysis of ATP by polymerized actin depends on the bound divalent cation but not profilin. *Biochemistry*, *41*(2), 597-602.

Blanchoin, L., Boujemaa-Paterski, R., Sykes, C., & Plastino, J. (2014). Actin dynamics, architecture, and mechanics in cell motility. *Physiological reviews*, *94*(1), 235-263.

Brennan, J. R., & Hocking, D. C. (2016). Cooperative effects of fibronectin matrix assembly and initial cell–substrate adhesion strength in cellular self-assembly. *Acta biomaterialia*, *32*, 198-209.

Bretscher, A. (1981). Fimbrin is a cytoskeletal protein that crosslinks F-actin in vitro. Proceedings of the National Academy of Sciences, 78(11), 6849-6853.

Brouhard, G. J., & Rice, L. M. (2018). Microtubule dynamics: an interplay of biochemistry and mechanics. *Nature reviews Molecular cell biology*, *19*(7), 451-463.

Broussard, J. A., Diggins, N. L., Hummel, S., Georgescu, W., Quaranta, V., & Webb, D. J. (2015). Automated analysis of cell-matrix adhesions in 2D and 3D environments. *Scientific reports*, *5*(1), 1-10.

Burke, B., & Stewart, C. L. (2013). The nuclear lamins: flexibility in function. *Nature reviews Molecular cell biology*, *14*(1), 13-24.

Burnette, D. T., Manley, S., Sengupta, P., Sougrat, R., Davidson, M. W., Kachar, B., & Lippincott-Schwartz, J. (2011). A role for actin arcs in the leading-edge advance of migrating cells. *Nature cell biology*, *13*(4), 371-382.

Burnette, D. T., Shao, L., Ott, C., Pasapera, A. M., Fischer, R. S., Baird, M. A., ... & Lippincott-Schwartz, J. (2014). A contractile and counterbalancing adhesion system controls the 3D shape of crawling cells. *Journal of Cell Biology*, *205*(1), 83-96.

Burridge, K. (2017). Focal adhesions: a personal perspective on a half century of progress. The FEBS journal, 284(20), 3355-3361.

Burridge, K., & Connell, L. (1983). A new protein of adhesion plaques and ruffling membranes. The Journal of cell biology, 97(2), 359-367.

Burridge, K., & Guilluy, C. (2016). Focal adhesions, stress fibers and mechanical tension. Experimental cell research, 343(1), 14-20.

Burridge, K., & Wittchen, E. S. (2013). The tension mounts: stress fibers as force-generating mechanotransducers. *Journal of Cell Biology*, *200*(1), 9-19.

Buskermolen, A. B., Kurniawan, N. A., & Bouten, C. V. (2018). An automated quantitative analysis of cell, nucleus and focal adhesion morphology. *PLoS One*, *13*(3), e0195201.

Calderwood, D. A., Zent, R., Grant, R., Rees, D. J. G., Hynes, R. O., & Ginsberg, M. H. (1999). The talin head domain binds to integrin β subunit cytoplasmic tails and regulates integrin activation. *Journal of Biological Chemistry*, *274*(40), 28071-28074.

Carlier, M. F., & Shekhar, S. (2017). Global treadmilling coordinates actin turnover and controls the size of actin networks. *Nature Reviews Molecular Cell Biology*, *18*(6), 389-401.

Case, L. B., & Waterman, C. M. (2015). Integration of actin dynamics and cell adhesion by a three-dimensional, mechanosensitive molecular clutch. *Nature cell biology*, *17*(8), 955-963.

Choi, C. K., Vicente-Manzanares, M., Zareno, J., Whitmore, L. A., Mogilner, A., & Horwitz, A. R. (2008). Actin and α-actinin orchestrate the assembly and maturation of nascent adhesions in a myosin II motor-independent manner. *Nature cell biology*, *10*(9), 1039-1050.

Chrzanowska-Wodnicka, M., & Burridge, K. (1996). Rho-stimulated contractility drives the formation of stress fibers and focal adhesions. *The Journal of cell biology*, *133*(6), 1403-1415.

Ciobanasu, C., Faivre, B., & Le Clainche, C. (2012). Actin dynamics associated with focal adhesions. *International journal of cell biology*, *2012*.

Clayton, J. E., Pollard, L. W., Sckolnick, M., Bookwalter, C. S., Hodges, A. R., Trybus, K. M., & Lord, M. (2014). Fission yeast tropomyosin specifies directed transport of myosin-V along actin cables. Molecular biology of the cell, 25(1), 66-75.

Cooper, G. M. (2000). Structure and organization of actin filaments. *The cell: a molecular approach*, *2*.

Cooper, J. A. (2002). Actin dynamics: tropomyosin provides stability. Current Biology, 12(15), R523-R525.

Cooper, J. A., & Sept, D. (2008). New insights into mechanism and regulation of actin capping protein. *International review of cell and molecular biology*, *267*, 183-206.

Cramer, L. P., Siebert, M., & Mitchison, T. J. (1997). Identification of novel graded polarity actin filament bundles in locomoting heart fibroblasts: implications for the generation of motile force. The Journal of cell biology, 136(6), 1287-1305.

Critchley, D. R. (2009). Biochemical and structural properties of the integrin-associated cytoskeletal protein talin. *Annual review of biophysics*, *38*, 235-254.

Critchley, D. R., & Gingras, A. R. (2008). Talin at a glance. *Journal of cell science*, *121*(9), 1345-1347.

Deakin, N. O., & Turner, C. E. (2008). Paxillin comes of age. Journal of cell science, 121(15), 2435-2444.

Deguchi, S., & Sato, M. (2009). Biomechanical properties of actin stress fibers of non-motile cells. *Biorheology*, *46*(2), 93-105.

Dixon, R. D., Arneman, D. K., Rachlin, A. S., Sundaresan, N. R., Costello, M. J., Campbell, S. L., & Otey, C. A. (2008). Palladin is an actin cross-linking protein that uses immunoglobulin-like domains to bind filamentous actin. Journal of Biological Chemistry, 283(10), 6222-6231.

Dos Remedios, C. G., Chhabra, D., Kekic, M., Dedova, I. V., Tsubakihara, M., Berry, D. A., & Nosworthy, N. J. (2003). Actin binding proteins: regulation of cytoskeletal microfilaments. *Physiological reviews*, *83*(2), 433-473.

Drees, B., Friederich, E., Fradelizi, J., Louvard, D., Beckerle, M. C., & Golsteyn, R. M. (2000). Characterization of the interaction between zyxin and members of the Ena/vasodilator-stimulated phosphoprotein family of proteins. *Journal of Biological Chemistry*, *275*(29), 22503-22511.

Du, J., & Frieden, C. (1998). Kinetic studies on the effect of yeast cofilin on yeast actin polymerization. *Biochemistry*, *37*(38), 13276-13284.

Dumbauld, D. W., Lee, T. T., Singh, A., Scrimgeour, J., Gersbach, C. A., Zamir, E. A., ... & García, A. J. (2013). How vinculin regulates force transmission. *Proceedings of the National Academy of Sciences*, *110*(24), 9788-9793.

Dumbauld, D. W., Shin, H., Gallant, N. D., Michael, K. E., Radhakrishna, H., & García, A. J. (2010). Contractility modulates cell adhesion strengthening through focal adhesion kinase and assembly of vinculin-containing focal adhesions. Journal of cellular physiology, 223(3), 746-756.

Eltzner, B., Wollnik, C., Gottschlich, C., Huckemann, S., & Rehfeldt, F. (2015). The filament sensor for near real-time detection of cytoskeletal fiber structures. *PloS one*, *10*(5), e0126346.

Feng, Y., Ngu, H., Alford, S. K., Ward, M., Yin, F., & Longmore, G. D. (2013). α-Actinin1 and 4 tyrosine phosphorylation is critical for stress fiber establishment, maintenance and focal adhesion maturation. *Experimental cell research*, *319*(8), 1124-1135.

Fletcher, D. A., & Mullins, R. D. (2010). Cell mechanics and the cytoskeleton. Nature, 463(7280), 485-492.

Funk, J., Merino, F., Schaks, M., Rottner, K., Raunser, S., & Bieling, P. (2021). A barbed end interference mechanism reveals how capping protein promotes nucleation in branched actin networks. *Nature communications*, *12*(1), 1-17.

Gardel, M. L., Schneider, I. C., Aratyn-Schaus, Y., & Waterman, C. M. (2010). Mechanical integration of actin and adhesion dynamics in cell migration. Annual review of cell and developmental biology, 26, 315-333.

Geiger, B. (1979). A 130K protein from chicken gizzard: its localization at the termini of microfilament bundles in cultured chicken cells. Cell, 18(1), 193-205.

Ghilardi, S. J., Aronson, M. S., & Sgro, A. E. (2021). Ventral stress fibers induce plasma membrane deformation in human fibroblasts. Molecular biology of the cell, 32(18), 1707-1723.

Goldschmidt-Clermont, P. J., Machesky, L. M., Baldassare, J. J., & Pollard, T. D. (1990). The actin-binding protein profilin binds to PIP2 and inhibits its hydrolysis by phospholipase C. Science, 247(4950), 1575-1578.

Goode, B. L., Drubin, D. G., & Lappalainen, P. (1998). Regulation of the cortical actin cytoskeleton in budding yeast by twinfilin, a ubiquitous actin monomer-sequestering protein. *The Journal of cell biology*, *142*(3), 723-733.

Gruenbaum, Y., Margalit, A., Goldman, R. D., Shumaker, D. K., & Wilson, K. L. (2005). The nuclear lamina comes of age. *Nature reviews Molecular cell biology*, *6*(1), 21-31.

Gudimchuk, N. B., & McIntosh, J. R. (2021). Regulation of microtubule dynamics, mechanics and function through the growing tip. *Nature Reviews Molecular Cell Biology*, *22*(12), 777-795.

Gunning, P., O'neill, G., & Hardeman, E. (2008). Tropomyosin-based regulation of the actin cytoskeleton in time and space. Physiological reviews, 88(1), 1-35.

Guo, F., Debidda, M., Yang, L., Williams, D. A., & Zheng, Y. (2006). Genetic deletion of Rac1 GTPase reveals its critical role in actin stress fiber formation and focal adhesion complex assembly. *Journal of Biological Chemistry*, *281*(27), 18652-18659.

Gupton, S. L., & Waterman-Storer, C. M. (2006). Spatiotemporal feedback between actomyosin and focal-adhesion systems optimizes rapid cell migration. *Cell*, *125*(7), 1361-1374.

Heath, J. P. (1983). Behaviour and structure of the leading lamella in moving fibroblasts. I. Occurrence and centripetal movement of arc-shaped microfilament bundles beneath the dorsal cell surface. *Journal of cell science*, *60*(1), 331-354.

Heath, J. P., & Dunn, G. A. (1978). Cell to substratum contacts of chick fibroblasts and their relation to the microfilament system. A correlated interference-reflexion and high-voltage electron-microscope study. Journal of cell science, 29(1), 197-212.

Hirata, H., Tatsumi, H., & Sokabe, M. (2008). Mechanical forces facilitate actin polymerization at focal adhesions in a zyxin-dependent manner. *Journal of cell science*, *121*(17), 2795-2804.

Hirata, H., Tatsumi, H., & Sokabe, M. (2008). Zyxin emerges as a key player in the mechanotransduction at cell adhesive structures. *Communicative & integrative biology*, *1*(2), 192-195.

Hliscs, M., Sattler, J. M., Tempel, W., Artz, J. D., Dong, A., Hui, R., ... & Schüler, H. (2010). Structure and function of a G-actin sequestering protein with a vital role in malaria oocyst development inside the mosquito vector. *Journal of Biological Chemistry*, *285*(15), 11572-11583.

Hoffman, L. M., Jensen, C. C., Chaturvedi, A., Yoshigi, M., & Beckerle, M. C. (2012). Stretch-induced actin remodeling requires targeting of zyxin to stress fibers and recruitment of actin regulators. *Molecular biology of the cell*, *23*(10), 1846-1859.

Hoffman, L. M., Jensen, C. C., Kloeker, S., Wang, C. L. A., Yoshigi, M., & Beckerle, M. C. (2006). Genetic ablation of zyxin causes Mena/VASP mislocalization, increased motility, and deficits in actin remodeling. *The Journal of cell biology*, *172*(5), 771-782.

Hohmann, T., & Dehghani, F. (2019). The cytoskeleton—a complex interacting meshwork. Cells, 8(4), 362.

Holmes, K. C., Popp, D., Gebhard, W., & Kabsch, W. (1990). Atomic model of the actin filament. *Nature*, *347*(6288), 44-49.

Hotulainen, P., & Lappalainen, P. (2006). Stress fibers are generated by two distinct actin assembly mechanisms in motile cells. *The Journal of cell biology*, *173*(3), 383-394.

Humphries, J. D., Wang, P., Streuli, C., Geiger, B., Humphries, M. J., & Ballestrem, C. (2007). Vinculin controls focal adhesion formation by direct interactions with talin and actin. *The Journal of cell biology*, *179*(5), 1043-1057.

Kanchanawong, P., Shtengel, G., Pasapera, A. M., Ramko, E. B., Davidson, M. W., Hess, H. F., & Waterman, C. M. (2010). Nanoscale architecture of integrin-based cell adhesions. *Nature*, *468*(7323), 580-584.

Kanellos, G., Zhou, J., Patel, H., Ridgway, R. A., Huels, D., Gurniak, C. B., ... & Frame, M. C. (2015). ADF and Cofilin1 control actin stress fibers, nuclear integrity, and cell survival. *Cell reports*, *13*(9), 1949-1964.

Kassianidou, E., & Kumar, S. (2015). A biomechanical perspective on stress fiber structure and function. *Biochimica et Biophysica Acta (BBA)-Molecular Cell Research*, *1853*(11), 3065-3074.

Khaitlina, S., Fitz, H., & Hinssen, H. (2013). The interaction of gelsolin with tropomyosin modulates actin dynamics. The FEBS journal, 280(18), 4600-4611.

Kong, F., García, A. J., Mould, A. P., Humphries, M. J., & Zhu, C. (2009). Demonstration of catch bonds between an integrin and its ligand. Journal of Cell Biology, 185(7), 1275-1284.

Kovac, B., Teo, J. L., Mäkelä, T. P., & Vallenius, T. (2013). Assembly of non-contractile dorsal stress fibers requires α-actinin-1 and Rac1 in migrating and spreading cells. *Journal of cell science*, *126*(1), 263-273.

Krishnan, K., & Moens, P. D. (2009). Structure and functions of profilins. Biophysical reviews, 1(2), 71-81.

Laine, R. O., Phaneuf, K. L., Cunningham, C. C., Kwiatkowski, D., Azuma, T., & Southwick, F. S. (1998). Gelsolin, a protein that caps the barbed ends and severs actin filaments, enhances the actin-based motility of Listeria monocytogenes in host cells. Infection and immunity, 66(8), 3775-3782.

Lazarides, E., & Burridge, K. (1975). α-Actinin: immunofluorescent localization of a muscle structural protein in nonmuscle cells. *Cell*, *6*(3), 289-298.

Lee, S., Kassianidou, E., & Kumar, S. (2018). Actomyosin stress fiber subtypes have unique viscoelastic properties and roles in tension generation. *Molecular biology of the cell*, *29*(16), 1992-2004.

Legerstee, K., & Houtsmuller, A. B. (2021). A Layered View on Focal Adhesions. Biology, 10(11), 1189.

Lehtimäki, J. I., Rajakylä, E. K., Tojkander, S., & Lappalainen, P. (2021). Generation of stress fibers through myosin-driven reorganization of the actin cortex. *Elife*, *10*, e60710.

Lekka, M., Gnanachandran, K., Kubiak, A., Zieliński, T., & Zemła, J. (2021). Traction force microscopy–Measuring the forces exerted by cells. *Micron*, *150*, 103138.

Lele, T. P., Pendse, J. A. Y., Kumar, S., Salanga, M., Karavitis, J., & Ingber, D. E. (2006). Mechanical forces alter zyxin unbinding kinetics within focal adhesions of living cells. *Journal of cellular physiology*, *207*(1), 187-194.

Lemmon, C. A., Chen, C. S., & Romer, L. H. (2009). Cell traction forces direct fibronectin matrix assembly. *Biophysical journal*, *96*(2), 729-738.

Letort, G., Ennomani, H., Gressin, L., Théry, M., & Blanchoin, L. (2015). Dynamic reorganization of the actin cytoskeleton. *F1000Research*, *4*.

Lewis, W. H., & Lewis, M. R. (1924). Behavior of cells in tissue cultures. *General cytology*, 385-447.

Li, B., & Trueb, B. (2001). Analysis of the α-actinin/zyxin interaction. Journal of Biological Chemistry, 276(36), 33328-33335.

Liu, J., Wang, Y., Goh, W. I., Goh, H., Baird, M. A., Ruehland, S., ... & Kanchanawong, P. (2015). Talin determines the nanoscale architecture of focal adhesions. *Proceedings of the National Academy of Sciences*, *112*(35), E4864-E4873.

Livne, A., & Geiger, B. (2016). The inner workings of stress fibers− from contractile machinery to focal adhesions and back. *Journal of Cell Science*, *129*(7), 1293-1304.

Maciver, S. K., & Hussey, P. J. (2002). The ADF/cofilin family: actin-remodeling proteins. *Genome biology*, *3*(5), 1-12.

Martins, B., Sorrentino, S., Chung, W. L., Tatli, M., Medalia, O., & Eibauer, M. (2021). Unveiling the polarity of actin filaments by cryo-electron tomography. *Structure*, *29*(5), 488-498.

McCullagh, M., Saunders, M. G., & Voth, G. A. (2014). Unraveling the mystery of ATP hydrolysis in actin filaments. *Journal of the American Chemical Society*, *136*(37), 13053-13058.

McGough, A., Pope, B., Chiu, W., & Weeds, A. (1997). Cofilin changes the twist of F-actin: implications for actin filament dynamics and cellular function. *The Journal of cell biology*, *138*(4), 771-781.

Merino, F., Pospich, S., & Raunser, S. (2020, June). Towards a structural understanding of the remodeling of the actin cytoskeleton. In *Seminars in Cell & Developmental Biology* (Vol. 102, pp. 51-64). Academic Press.

Metzler, W. J., Bell, A. J., Ernst, E., Lavoie, T. B., & Mueller, L. (1994). Identification of the poly-L-proline-binding site on human profilin. Journal of Biological Chemistry, 269(6), 4620-4625.

Mitra, S. K., Hanson, D. A., & Schlaepfer, D. D. (2005). Focal adhesion kinase: in command and control of cell motility. Nature reviews Molecular cell biology, 6(1), 56-68.

Murphy, A. C., & Young, P. W. (2015). The actinin family of actin cross-linking proteins–a genetic perspective. Cell & bioscience, 5(1), 1-9.

Nag, S., Larsson, M., Robinson, R. C., & Burtnick, L. D. (2013). Gelsolin: the tail of a molecular gymnast. Cytoskeleton, 70(7), 360-384.

Nakamura, F., Stossel, T. P., & Hartwig, J. H. (2011). The filamins: organizers of cell structure and function. Cell adhesion & migration, 5(2), 160-169.

Niwa, R., Nagata-Ohashi, K., Takeichi, M., Mizuno, K., & Uemura, T. (2002). Control of actin reorganization by Slingshot, a family of phosphatases that dephosphorylate ADF/cofilin. *Cell*, *108*(2), 233-246.

Nobes, C. D., & Hall, A. (1995). Rho, rac, and cdc42 GTPases regulate the assembly of multimolecular focal complexes associated with actin stress fibers, lamellipodia, and filopodia. Cell, 81(1), 53-62.

Nogales, E. (2000). Structural insights into microtubule function. *Annual review of biochemistry*, *69*(1), 277-302.

Nowak, J., Gennermann, K., Persson, S., & Nikoloski, Z. (2020). CytoSeg 2.0: automated extraction of actin filaments. *Bioinformatics*, *36*(9), 2950-2951.

Oakes, P. W., Beckham, Y., Stricker, J., & Gardel, M. L. (2012). Tension is required but not sufficient for focal adhesion maturation without a stress fiber template. *Journal of Cell Biology*, *196*(3), 363-374.

Oda, T., Iwasa, M., Aihara, T., Maéda, Y., & Narita, A. (2009). The nature of the globular- to fibrous-actin transition. *Nature*, *457*(7228), 441-445.

Parsons, J. T. (2003). Focal adhesion kinase: the first ten years. *Journal of cell science*, *116*(8), 1409-1416.

Parsons, J. T., Horwitz, A. R., & Schwartz, M. A. (2010). Cell adhesion: integrating cytoskeletal dynamics and cellular tension. *Nature reviews Molecular cell biology*, *11*(9), 633-643.

Pellegrin, S., & Mellor, H. (2007). Actin stress fibres. Journal of cell science, 120(20), 3491-3499.

Perrin, B. J., & Ervasti, J. M. (2010). The actin gene family: function follows isoform. *Cytoskeleton*, *67*(10), 630-634.

Plotnikov, S. V., Sabass, B., Schwarz, U. S., & Waterman, C. M. (2014). High-resolution traction force microscopy. In *Methods in cell biology* (Vol. 123, pp. 367-394). Academic Press.

Pollard, T. D. (1986). Rate constants for the reactions of ATP-and ADP-actin with the ends of actin filaments. *The Journal of cell biology*, *103*(6), 2747-2754.

Pollard, T. D. (2007). Regulation of actin filament assembly by Arp2/3 complex and formins. Annu. Rev. Biophys. Biomol. Struct., 36, 451-477.

Pollard, T. D. (2016). Actin and actin-binding proteins. *Cold Spring Harbor perspectives in biology*, *8*(8), a018226.

Pollard, T. D., & Cooper, J. A. (1986). Actin and actin-binding proteins. A critical evaluation of mechanisms and functions. *Annual review of biochemistry*, *55*(1), 987-1035.

Qin, S., Ricotta, V., Simon, M., Clark, R. A., & Rafailovich, M. H. (2015). Continual cell deformation induced via attachment to oriented fibers enhances fibroblast cell migration. PloS one, 10(3), e0119094.

Ressad, F., Didry, D., Egile, C., Pantaloni, D., & Carlier, M. F. (1999). Control of actin filament length and turnover by actin depolymerizing factor (ADF/cofilin) in the presence of capping proteins and ARP2/3 complex. *Journal of Biological Chemistry*, *274*(30), 20970-20976.

Rid, R., Schiefermeier, N., Grigoriev, I., Small, J. V., & Kaverina, I. (2005). The last but not the least: the origin and significance of trailing adhesions in fibroblastic cells. *Cell motility and the cytoskeleton*, *61*(3), 161-171.

Riveline, D., Zamir, E., Balaban, N. Q., Schwarz, U. S., Ishizaki, T., Narumiya, S., ... & Bershadsky, A. D. (2001). Focal contacts as mechanosensors: externally applied local mechanical force induces growth of focal contacts by an mDia1-dependent and ROCK-independent mechanism. The Journal of cell biology, 153(6), 1175-1186.

Roca-Cusachs, P., Del Rio, A., Puklin-Faucher, E., Gauthier, N. C., Biais, N., & Sheetz, M. P. (2013). Integrin-dependent force transmission to the extracellular matrix by α-actinin triggers adhesion maturation. *Proceedings of the National Academy of Sciences*, *110*(15), E1361-E1370.

Rogge, H., Artelt, N., Endlich, N., & Endlich, K. (2017). Automated segmentation and quantification of actin stress fibres undergoing experimentally induced changes. *Journal of microscopy*, *268*(2), 129-140.

Rottner, K., Krause, M., Gimona, M., Small, J. V., & Wehland, J. (2001). Zyxin is not colocalized with vasodilator-stimulated phosphoprotein (VASP) at lamellipodial tips and exhibits different dynamics to vinculin, paxillin, and VASP in focal adhesions. *Molecular biology of the cell*, *12*(10), 3103-3113.

Safer, D., Sosnick, T. R., & Elzinga, M. (1997). Thymosin β4 binds actin in an extended conformation and contacts both the barbed and pointed ends. *Biochemistry*, *36*(19), 5806-5816.

Schafer, D. A., Hug, C., & Cooper, J. A. (1995). Inhibition of CapZ during myofibrillogenesis alters assembly of actin filaments. *The Journal of cell biology*, *128*(1), 61-70.

Schaller, M. D. (2001). Paxillin: a focal adhesion-associated adaptor protein. Oncogene, 20(44), 6459-6472.

Schindelin, J., Arganda-Carreras, I., Frise, E., Kaynig, V., Longair, M., Pietzsch, T., ... & Cardona, A. (2012). Fiji: an open-source platform for biological-image analysis. *Nature methods*, *9*(7), 676-682.

Schneider, C. A., Rasband, W. S., & Eliceiri, K. W. (2012). NIH Image to ImageJ: 25 years of image analysis. *Nature methods*, *9*(7), 671-675.

Sjöblom, B., Salmazo, A., & Djinović-Carugo, K. (2008). α-Actinin structure and regulation. *Cellular and molecular life sciences*, *65*(17), 2688-2701.

Small, J. V., Rottner, K., Kaverina, I., & Anderson, K. I. (1998). Assembling an actin cytoskeleton for cell attachment and movement. Biochimica Et Biophysica Acta (BBA)-Molecular Cell Research, 1404(3), 271-281.

Smith, M. A., Blankman, E., Gardel, M. L., Luettjohann, L., Waterman, C. M., & Beckerle, M. C. (2010). A zyxin-mediated mechanism for actin stress fiber maintenance and repair. *Developmental cell*, *19*(3), 365-376.

Soiné, J. R., Brand, C. A., Stricker, J., Oakes, P. W., Gardel, M. L., & Schwarz, U. S. (2015). Model-based traction force microscopy reveals differential tension in cellular actin bundles. *PLoS computational biology*, *11*(3), e1004076.

Squire, J. (2019). The actin-myosin interaction in muscle: Background and overview. *International Journal of Molecular Sciences*, *20*(22), 5715.

Sumi, T., Matsumoto, K., Takai, Y., & Nakamura, T. (1999). Cofilin phosphorylation and actin cytoskeletal dynamics regulated by rho-and Cdc42-activated LIM-kinase 2. *The Journal of cell biology*, *147*(7), 1519-1532.

Takada, Y., Ye, X., & Simon, S. (2007). The integrins. Genome biology, 8(5), 1-9.

Takagi, J., Petre, B. M., Walz, T., & Springer, T. A. (2002). Global conformational rearrangements in integrin extracellular domains in outside-in and inside-out signaling. Cell, 110(5), 599-611.

Thevenaz, P., Ruttimann, U. E., & Unser, M. (1998). A pyramid approach to subpixel registration based on intensity. IEEE transactions on image processing, 7(1), 27-41.

Tojkander, S., Gateva, G., & Lappalainen, P. (2012). Actin stress fibers–assembly, dynamics and biological roles. Journal of cell science, 125(8), 1855-1864.

Tojkander, S., Gateva, G., Husain, A., Krishnan, R., & Lappalainen, P. (2015). Generation of contractile actomyosin bundles depends on mechanosensitive actin filament assembly and disassembly. *Elife*, *4*, e06126.

Tojkander, S., Gateva, G., Schevzov, G., Hotulainen, P., Naumanen, P., Martin, C., ... & Lappalainen, P. (2011). A molecular pathway for myosin II recruitment to stress fibers. *Current Biology*, *21*(7), 539-550.

Uemura, A., Nguyen, T. N., Steele, A. N., & Yamada, S. (2011). The LIM domain of zyxin is sufficient for force-induced accumulation of zyxin during cell migration. Biophysical journal, 101(5), 1069-1075.

Valencia, F. R., Sandoval, E., Du, J., Iu, E., Liu, J., & Plotnikov, S. V. (2021). Force-dependent activation of actin elongation factor mDia1 protects the cytoskeleton from mechanical damage and promotes stress fiber repair. *Developmental Cell*, *56*(23), 3288-3302.

Vallenius, T. (2013). Actin stress fibre subtypes in mesenchymal-migrating cells. *Open biology*, *3*(6), 130001.

Vicente-Manzanares, M., Newell-Litwa, K., Bachir, A. I., Whitmore, L. A., & Horwitz, A. R. (2011). Myosin IIA/IIB restrict adhesive and protrusive signaling to generate front–back polarity in migrating cells. *Journal of Cell Biology*, *193*(2), 381-396.

Vignaud, T., Copos, C., Leterrier, C., Toro-Nahuelpan, M., Tseng, Q., Mahamid, J., ... & Kurzawa, L. (2021). Stress fibres are embedded in a contractile cortical network. *Nature materials*, *20*(3), 410-420.

Wang, Y. L. (1984). Reorganization of actin filament bundles in living fibroblasts. *The Journal of cell biology*, *99*(4), 1478-1485.

Webb, D. J., Donais, K., Whitmore, L. A., Thomas, S. M., Turner, C. E., Parsons, J. T., & Horwitz, A. F. (2004). FAK–Src signalling through paxillin, ERK and MLCK regulates adhesion disassembly. Nature cell biology, 6(2), 154-161.

Weber, A., Pennise, C. R., & Pring, M. (1994). DNase I increases the rate constant of depolymerization at the pointed (-) end of actin filaments. *Biochemistry*, *33*(16), 4780-4786.

Weber, A., Pennise, C. R., Babcock, G. G., & Fowler, V. M. (1994). Tropomodulin caps the pointed ends of actin filaments. *The Journal of cell biology*, *127*(6), 1627-1635.

Wolfenson, H., Bershadsky, A., Henis, Y. I., & Geiger, B. (2011). Actomyosin-generated tension controls the molecular kinetics of focal adhesions. Journal of cell science, 124(9), 1425-1432.

Ye, N., Verma, D., Meng, F., Davidson, M. W., Suffoletto, K., & Hua, S. Z. (2014). Direct observation of α-actinin tension and recruitment at focal adhesions during contact growth. *Experimental cell research*, *327*(1), 57-67.

Yoshigi, M., Clark, E. B., & Yost, H. J. (2003). Quantification of stretch-induced cytoskeletal remodeling in vascular endothelial cells by image processing. *Cytometry Part A: The Journal of the International Society for Analytical Cytology*, *55*(2), 109-118.

Young, L. E., & Higgs, H. N. (2018). Focal adhesions undergo longitudinal splitting into fixed-width units. *Current Biology*, *28*(13), 2033-2045.

Zemel, A., Rehfeldt, F., Brown, A. E. X., Discher, D. E., & Safran, S. A. (2010). Optimal matrix rigidity for stress-fibre polarization in stem cells. *Nature physics*, *6*(6), 468-473.

Zemel, A., Rehfeldt, F., Brown, A. E. X., Discher, D. E., & Safran, S. A. (2010). Cell shape, spreading symmetry, and the polarization of stress-fibers in cells. *Journal of Physics: Condensed Matter*, *22*(19), 194110.

Zhang, Z., Xia, S., & Kanchanawong, P. (2017). An integrated enhancement and reconstruction strategy for the quantitative extraction of actin stress fibers from fluorescence micrographs. *BMC bioinformatics*, *18*(1), 1-14.

Ziegler, W. H., Liddington, R. C., & Critchley, D. R. (2006). The structure and regulation of vinculin. *Trends in cell biology*, *16*(9), 453-460.

Zimerman, B., Volberg, T., & Geiger, B. (2004). Early molecular events in the assembly of the focal adhesion-stress fiber complex during fibroblast spreading. *Cell motility and the cytoskeleton*, *58*(3), 143-159.

Zweifel, M. E., & Courtemanche, N. (2020). Competition for delivery of profilin–actin to barbed ends limits the rate of formin-mediated actin filament elongation. Journal of Biological Chemistry, 295(14), 4513-4525.